Universidad de Valladolid

Multidisciplinary System Design Optimisation of Oscillating Water Column Power Plants: a Nonlinear Stochastic Approach

Juan Gabriel González Gutiérrez

Submitted to the Department of
Energy Engineering and Fluid Dynamics
in partial fulfillment of the requirements for the degree of
Doctor of Engineering
at the
University of Valladolid

Supervisor: Prof Francisco Castro
Ind Supervisor: Dr Shahrokh Shahpar
October 2015

Empty

Acknowledgements

And I would like to acknowledge ...

Abstract

This is where you write your abstract ...

Contents

List of Figures

List of Tables

Nomenclature

BP Biplane Wells Turbine

CR Contra-rotating Wells Turbine

DFIG Doubly-Fed Induction Generator

MP Monoplane Wells Turbine

MSDO Multidisciplinary System Design Optimisation

MWL Mean Water Level

OWC Oscillating Water Column

PMSG Permanent Magnet Synchronous Generator

VLCRT Vaneless Contra-Rotating Turbine

VP Variable Pitch Wells Turbine

VoF Volume-of-Fluid multi-phase model

WEC Wave Energy Converter

WRSG Wound Rotor Synchronous Generator

DoE Design of Experiments

HOQ House Of Quality

OLHS Optimised Latin Hypercube Sampling

QFD Quality Function Deployment

NFPR Non-Functional Performance Requirement

uRANS Unsteady Reynolds-Averaged Navier-Stokes

VoC Voice of the Customer

Roman Symbols

A_{annulus} Turbine annulus area

A_w Wave amplitude

B_r Potential damping parameter

B_w Chamber breath

C_r Radiation restoration coefficient

$C_{w,i}$ Wave participation coefficient

C_1 Power Turbine bearing damping

C_{12} Turbine shaft damping

C_{23} Electrical Generator shaft damping

C_{2A} Gearbox bearing damping (turbine shaft)

C_{2B} Gearbox bearing damping (electrical generator shaft)

C_3 Electrical Generator bearing damping

CS Control surface

CV Control volume

d	Water depth
dS	Surface differential
dV	Volume differential
e	Reduced-order model error
$E(f)$	Power spectral density
$\vec{F}$	Force
f	Frequency
f_m	Frequency at the peak of the spectrum
GR	Gear Ratio
$\vec{g}$	Gravity acceleration vector
H_0	Total enthalpy
i	Electrical current
J_1	Power Turbine rotor inertia
J_{2A}	Gearbox inertia (turbine shaft)
J_{2B}	Gearbox inertia (electrical generator shaft)
J_3	Electrical Generator rotor inertia
K	Loss coefficient
k	Wave number k=$\frac{2\pi}{\lambda}$
K_1	Power Turbine bearing stiffness
K_{12}	Turbine shaft stiffness

K_{23}	Electrical Generator shaft stiffness
K_{2A}	Gearbox bearing stiffness (turbine shaft)
K_{2B}	Gearbox bearing stiffness (electrical generator shaft)
K_3	Electrical Generator bearing stiffness
K_C	Keulegan-Carpenter number
K_v	Eddy loss coefficient
L_a	Air reservoir height
L_w	Submergence depth
$\dot{m}$	Mass flow rate
M_r	Added-mass coefficient
$\vec{n}$	Unity vector normal to the control surface
N_w	Number of wave frequencies in the spectrum
p	Number of pole pairs
p	Static pressure
q	Mode participation factor
$\mathscr{R}$	Electric resistance
Re	Reynolds Number
R_L	Lip radius
S	Surface
s	Static entropy

T	Static temperature
t	Time
T_g	Electrical Generator torque load
th_{wall}	Concrete wall thickness
T_m	Power Turbine drive torque
$\mathscr{U}$	Uniform probability density function
v	Voltage
$\vec{v}$	Absolute velocity vector
V	Volume
v_r	Radial velocity component
v_t	Tangential velocity component
v_x	Radial velocity component
$\vec{w}$	Relative velocity
W_w	Chamber width
$\mathscr{X}$	Reactance
$\widetilde{X}$	Drive train variable reduced to turbine shaft
x	x coordinate
$y+$	Non-dimensional wall distance
z	z coordinate

Greek Symbols

α	Phillips constant (Jonswap sprectrum)
β_i	Sea wave component phase
η	Heave amplitude
γ	Ratio of the maximal spectral energy (Jonswap sprectrum)
$\mathscr{X}_\mu$	Magnetising reactance
λ	Wavelength
μ	Dynamic viscosity
ω_e	Electrical speed
Ω_r	Generator rotor speed of rotation
ω_S	Synchronous speed
ϕ	Mode shape
ϑ	Slosh angle
$\widetilde{\phi}$	Admissible function
ψ	Free-surface slope
ρ	Static density
ρ_{m}	Material density
σ_a	Left shape factor (Jonswap sprectrum)
σ_b	Right shape factor (Jonswap sprectrum)
σ_{c}	Centrifugal steady stress
$\overline{\overline{\tau}}$	Shear stress tensor

θ_1 Power Turbine rotor angle

θ_2 Gearbox angle

θ_3 Electrical Generator angle

ω Angular frequency

Subscripts

atm Atmospheric

B Caisson Bottom opening

c Air plenum, reservoir

d Direct axis

e Excitation

fr Friction

FS Free Surface

H Hydrostatic

h Heave mode

j Mode index

p Pitch mode

q Quadrature axis

r Radiation

r Rotor

s Stator

SW	Caisson Side Wall
v	Vortex dissipation
w	Water

Other Symbols

$\langle\ \rangle$	Area-averaged variable $\langle y \rangle = \frac{1}{S}\int_S y\,\mathrm{d}S$
$\cdot$	Dot product
$\frac{\mathrm{D}}{\mathrm{D}t}$	Material or Lagrangian derivative

Chapter 1

Introduction

1.1 Introduction

The contribution to installed capacity from renewable energy sources is forecasted to increase significantly. Investments in this type of technologies have increased over the last decades which are estimated to decrease their cost. Among all the renewable energies, large hydro has dominated the renewable market, but it might be overtaken by on- and off-shore wind power by 2030 according to the World Energy Council. Higher-cost technologies such as marine, solar thermal, or geothermal will have an significant contribution as they are more controllable.

Sea wave energy is one of the most promising renewable energy resources due to its market potential and energy density. The World Energy Council estimated the market potential for wave energy to be in excess of 2,000 TWh/year for fully mature devices. Sea wave energy density is one of the highest for renewable power sources, e.g. around 30-70 kW/m in the UK (see Gadonneix, 2010). Despite this promising outlook, sea wave energy still confronts significant challenges before it can be commercially exploited. The main obstacles have been power plant performance, reliability, survivability – the sea wave power can achieve in excess of 2000 kW/m during storms–, and

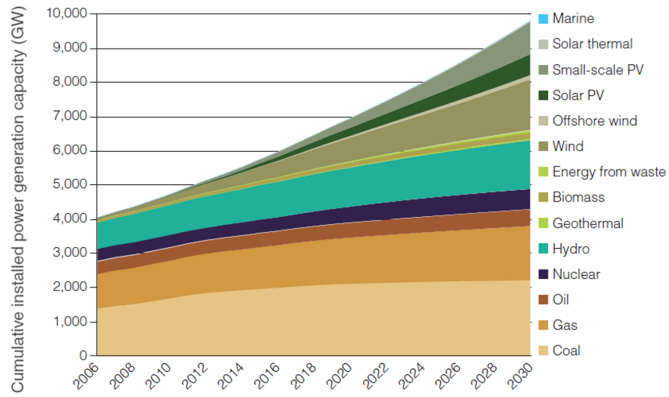

Source: Bloomberg New Energy Finance.
Note: forecast is from BNEF New Normal forecast scenario from the BNEF Global Renewable Energy Market Outlook: http://about.bnef.com/presentations/global-renewable-energy-market-outlook-2013-fact-pack-2

Fig. 1.1 Installed power generation capacity (2006-2030). Used by permission of the World Energy Council, London, www.worldenergy.org

environmental impact. The unsteady nature of sea waves, i.e. the wide range of sea wave periods, heights, and directions are challenging from a power plant efficiency perspective.

Amongst all the Wave Energy Converters (WECs), Oscillating Water Columns (OWCs) have become popular because their simplicity and structural robustness. These attributes have been proven by several demonstrators for instance Limpet in Scotland (UK), or Pico in the Azores (Portugal). Even so, poor cost-efficiency of energy production has been a major barrier to large-scale commercial exploitation.

1.2 Problem Formulation

The objective of this thesis is to perform a Multidisciplinary System Design Optimisation (MSDO) of an OWC power plant for a benchmark case for which wave state is representative of a suitable location.

The following steps have been taken to archive this objective:

(1) Develop a nonlinear parametric model for water column forced response.

(2) Develop a new turbine architecture which suits the OWC power plant functional requirements.

(3) Develop a nonlinear parametric reduced-order system model, which allows to investigate and optimise power plant operation under stochastic wave conditions.

(4) Develop a multi-fidelity turbine design system.

(5) Design and optimise a novel turbine.

(6) Define a suitable system optimisation problem: representative wave input, system design parameters, objective function, and penalty functions.

(7) Perform Multidisciplinary System Design Optimisation (MSDO) of an OWC power plant under representative wave conditions.

1.3 Original Contributions of the Thesis

The original contributions of this thesis are:

(1) A nonlinear stochastic reduced-order model for water column oscillation forced response prediction under irregular wave conditions has been developed (cf. **Chapter 3**). This method has been derived from the integral form of Conservation Laws and using a collocation method.

(2) A parametric model for water column added mass, dissimilar radiation coefficients for both exhaust and intake strokes, and hydrodynamic restoration coefficient (see **Chapter 3**)

(3) A multi-fidelity design framework based on the Non-Isentropic Radial Equilibrium Equation (NISRE) and Craix-Cox loss model. This design system comprises an efficient implement of the exploration-implementation strategy based on radial equilibrium and Unsteady Reynolds Navier-Stokes Computational Fluid Dynamics (uRANS CFD). This work has been presented in **Chapter 4**

(4) A novel Vane-Less Contra-Rotating Turbine (VLCRT) has been designed and optimised which has been described in **Chapter 4**. A patent was filed on the novel VLCRT turbine design.

(5) A nonlinear parametric system model for stochastic wave energy input conversion into electrical power. This model is presented in **Chapter 5**

(6) Multidisciplinary System Design Optimisation utilising the nonlinear parametric model under realistic sea-wave energy conditions. **Chapter 6** presents the optimisation method, constraints, and results

The nonlinear parametric system model has been validated and calibrated against higher-fidelity models to increase the accuracy of modelling without increasing the computational burden.

1.4 Structure of the Thesis

This thesis is organised as follows:

Chapter 2 presents the literature review relevant for the subjects in the following chapters.

Chapter 3 is devoted to the development a nonlinear reduced-order model utilising the integral form of the Conservation Laws and a collocation method. The validation and calibration of the empirical parameters of the nonlinear model are performed using a multi-phase two-

dimensional finite volume method simulation in ANSYS Fluent. Sixteen different models are generated based on the selected parameterisation by an Optimised Latin Hypercube Sampling (OLHS) to validate and to calibrate the reduced-order model.

Chapter 4 proposes the multi-fidelity design system utilised for the turbine design and optimisation. A novel non-free vortex design Vane-Less Contra-Rotating Turbine (VLCRT) is generated using the multi-fidelity design system and optimised via a genetic algorithm. The resulting optimised VLCRT shows several benefits for the OWC power plant environment operation which are analysed in this chapter.

Chapter 5 deals with the rest of the sub-systems (air system, drive train, electrical generator, and control system) which integrate the OWC power plant: air sub-system, drive train, and electrical generator. The proposed system-level model is described and verified.

Chapter 6 addresses the system-level optimisation of the OWC power plant using the reduced-order model developed and validated in the previous chapters. Two different approaches have been presented: (1) MSDO for a given turbine blading, and (2) MSDO including blading. The optimisation algorithms, optimisation problem, and constraints have also been described.

Chapter 7 presents the discussion of the results from the system-level optimisation and the inferred conclusions from this work. The limitations and assumptions in the system reduce-order model have been described in this chapter.

Chapter 8 shows the conclusions and future work strands derived from this thesis.

Chapter 2

Literature Review

2.1 OWC Power Plants

The Oscillating Water Column (OWC) power plants harvest energy from sea waves. Figure 2.1 presents a block diagram of five functional sub-systems which integrate the power plant:

(1) Water column;

(2) air system;

(3) power turbine;

(4) drive train or power train; and

(5) electric generator.

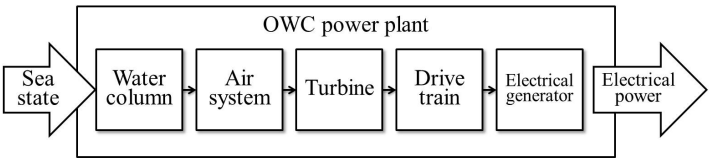

Fig. 2.1 OWC power plant system and sub-systems

Another support sub-system is usually required, although not essential, to control the power plant operation. Its elements greatly depend on the particular architecture of the power plant (such as relief valves, brakes, turbine blade pitch control, power electronics, etc.). Besides minimising the needs for a control system through a good design increases its operational robustness and reliability. Some control systems have been found to lower the overall plant efficiency as some actuators demand a significant amount of power to operate according to Thiebaut et al. (2011).

The water column and the air system are studied as a single entity in the literature, however have been split in the work presented in this thesis. The combination of both elements is known as *capture chamber*.

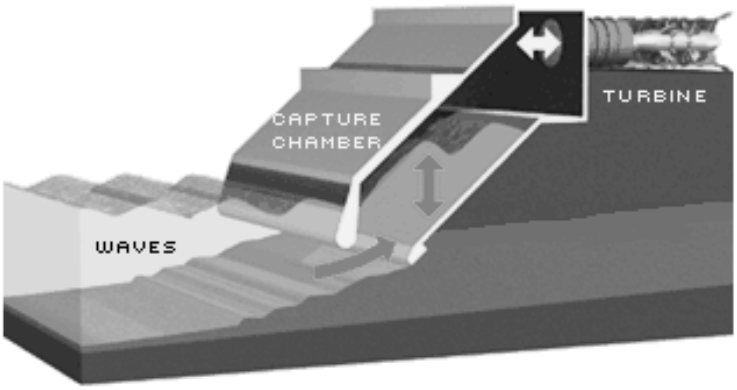

Fig. 2.2 Schematic view of an OWC (source: www.green-trust.com)

The *working principle* of OWC power plants is based on the conversion of the energy carried by the sea waves into electrical energy. There are three successive energy conversions: (1) hydraulic to pneumatic in the capture chamber, (2) pneumatic to mechanical shaft energy which is finally transformed into (3) electrical power through a rotating magnetic field in the electric generator driven by the power turbine.

The *working cycle* consists of two phases or processes:

(1) When the incident wave increases the water level inside a capture chamber, which is connected to the sea through a submerged opening. Therefrom, the free surface pushes some air out from the partly flooded chamber to the atmosphere. This process is the so-called *exhalation* or exhaust stroke.

(2) When the wave ebbs away, the water level falls inside the capture chamber forcing in air from the atmosphere. This phase is referred as *inhalation* or intake stroke.

Thus, OWC working cycle has two successive stages: exhalation and inhalation, with a period imposed by the sea wave characteristics. This can be seen as the capture chamber *breathing* air in and out.

The bi-directional alternating air flow, inhalation-exhalation, powers a turbine (typically rated power ranging from 50kW to 2MW) which rotates in a definite direction and extracts mechanical shaft power required to drive an electric generator to produce electricity. Such a turbine is known as *self-rectifying* turbine. Different types of OWC turbines have been proposed over the years (cf. Setoguchi and Takao, 2006). However, self-rectifying turbines have insufficient operating range (*Wells turbine*) or poor peak efficiency (*impulse turbine*). The Wells turbine was the first choice for all the OWC based wave energy plants which were built in Norway, Japan, Scotland, India, and China. This turbine and its variants (bi-plane, contra-rotating, etc.) have higher peak efficiency, but the range of operation is very narrow as the aerofoils suffer from severe stall at moderately high mass-flow rates. These turbines are described in detail in the following sections.

Table 2.1 lists the most important OWC devices and power plants which have been or still are in operation.

The power plant efficiency depends primarily on the capture efficiency which is a function of the chamber capture efficiency influenced by the turbine operation (Webb et al., 2005). The rest of sub-systems needs to be included in the analyses to allow for coupling effects between them, especially

Table 2.1 Main OWC devices and power plants

Location	Rated Power [kW]	Type	Turbine	Capture width [m]	Efficiency (real / estimated)
Limpet (Scotland)	500	On-shore	2 contra-rotative Wells turbines	21	40%/8%
OSPREY (Scotland)	2000	Near shore	4 Wells turbines	20	65%/-%
Pico (Azores)	400	On-shore	1 Wells turbines	12	35%/4%
Port Kembla (Australia)	300	Near shore	1 Denniss-Auld turbine	36	32.4%/-%
Sakata (Japan)	60	Breakwater	1 tandem Wells turbine	20	-%/-%
Toftestallen (Norway)	500	On-shore	-	10	-%/-%
Vizhinjam (India)	100	Breakwater	2 Wells turbines	14	-%/6.3%
Motrico (Spain)	250	Breakwater	16 Wells turbines	72	-%/6.3%

between capture chamber and power turbine, to achieve the desired performance. The measured efficiency of the OWC power plant that can be found in the public domain ranges from 6% to 8% (Webb et al., 2005). Average values for each sub-system have been reported in the literature for a type OWC power plant:

(1) The wave energy-to-pneumatic energy conversion process efficiency circa 40%;

(2) power turbine efficiencies between 30% and 40%; and

(3) the electric generator efficiency typically exceeds 90%.

The main advantages of the OWC power plant described in the literature are the following:

(1) Greatly-available renewable energy resource;

(2) flexible power plant location, limited by the inherit constraints of this technology;

(3) reduced underwater work compared to other WECs;

(4) off-site modular manufacturing;

(5) adaptable design to maximise energy harvesting for a given location;

(6) off-the-water moving elements, such as the power turbine; and

(7) reasonable protection against sea storms, hurricanes, and other extreme weather phenomena.

Despite the promising perspective of this technology, there are still several design challenges which need to be overcome before the OWC power plant could be industrialised. These aspects are listed below:

(1) OWC behaviour, design parameters, and loss modelling;

(2) chamber-power turbine coupling and matching;

(3) design rules, methods, and tools; and

(4) cost of civil engineering which could be in excess of 70%–85% of the total cost of the power plant (Webb et al., 2005).

2.1.1 Prior Art: Hydro-Pneumatic Power Plants and Navigation Buoys

The first patent found which of device that embodies all the elements of modern Oscillating Water Column Power Plants was filed on 18 Oct 1897 (Beckers, 1898). Fig. 2.3 depicts a cut-away and top view of the aforesaid invention. Compartment-chambers open at the outer end which allow waves to force air in the upper compartment into the air tank. The air is allowed to exit the chamber through a float-controlled valve to the air reservoir. Additionally, a double-action piston, which is pneumatically actuated, is connected to a motor-wheel through a crank mechanism.

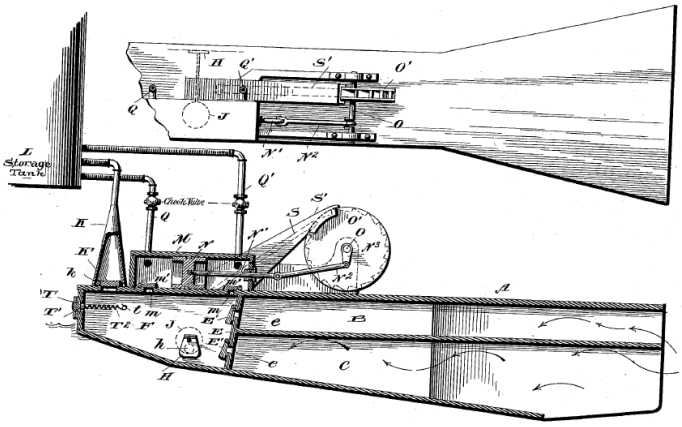

Fig. 2.3 Tide-water air compressor (Beckers, 1898)

Bissell (1907) proposed a wave motor comprising a tank open at the bottom which allows wave to push water in and out. The top of the chamber is closed and connected to a motor through a pipe system. A check valve system rectifies the flow such that the motor can operate. The exhaust is connected back to the partly-flooded tank. An emergency check valve allows to increase the air mass in the system (see Fig. 2.4).

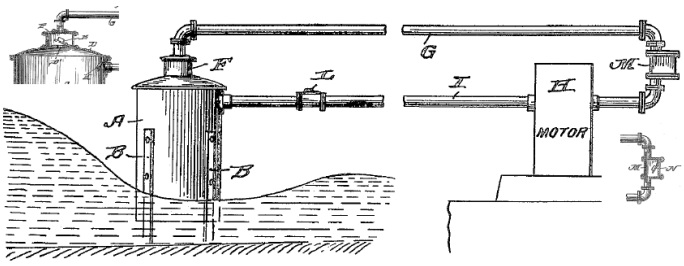

Fig. 2.4 Diagrammatic view of the wave motor (Bissell, 1907)

In 1910, M. Bochaux-Praceique vertically-tunneled a cliff which was communicated thought a bottom conduit to the sea (see fig. 2.5). The water inside the vertical cylinder created an Oscillating Water Column. This was the first-ever built device of this kind which was used to power an air turbine supplying enough energy to power a dwelling house.

Fig. 2.6 shows another hydro-pneumatic motor consists of a curved flared cylinder which has its lower end submerged in the water enclosing a buoyant piston. This floaty element rises and falls owing to the wave motion. Two turbines are then connected to the dry end of the cylinder, one of which is powered by the intake stroke and the other by the exhaust stroke. The flow is conditioned utilising a system of check valves.

Larry and Stein (1923) devised a wave-propelled vessel. The wave motor embodies two tanks having an opening through the bottom of the hull, both of which are connected to a common pipe in which a power wheel is located such that the pneumatic energy is converted into rotary motion. This motion is then transferred to a power train which drives a propeller (see Fig. 2.7).

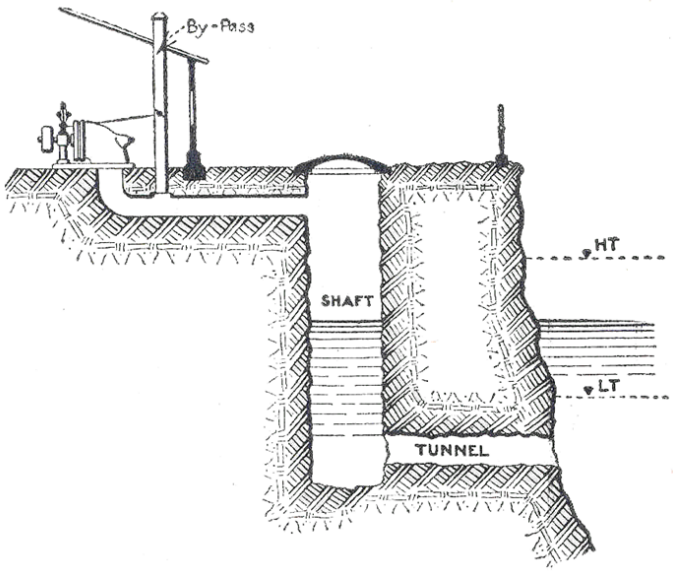

Fig. 2.5 First-ever built Oscillating Water Column power plant with an air turbine power off-take (Palme, 1920)

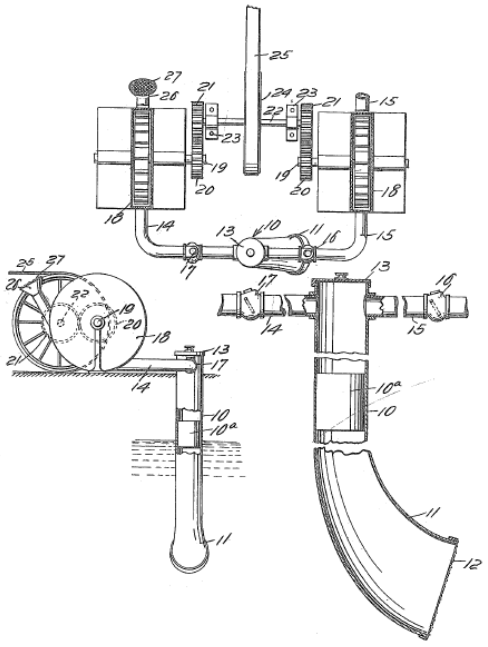

Fig. 2.6 Hydraulic air compressor and motor (Tuch, 1918)

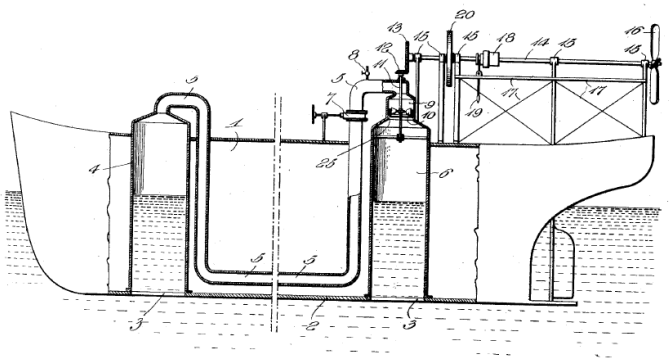

Fig. 2.7 Cut-away view of the water movement power vessel (Larry and Stein, 1923)

A hydro-pneumatic power plant was proposed by Paulson (1949). However, this device is not a wave energy converter but a tide-actuated apparatus, but the elements are similar enough to OWCs that it is worth having in consideration. Fig. 2.8 presents an schematic view of this unit which comprises a main tank and an auxiliary reservoir. The former is open at the bottom which allows the water to flow in and out during the tide cycle, uprising and dropping the free-surface level. The latter stores compressed air which is pumped from the main tank through a check valve. Once the tide has reached its maximum, an admission valve is opened in such a way that the compressed air is expanded through a turbine powering an electric generator. The process is driven by vacuum in the main tank when the tide recedes and the water level goes down. Again, the admission valve to the turbine is only actuated once the tide has reached its lowest level.

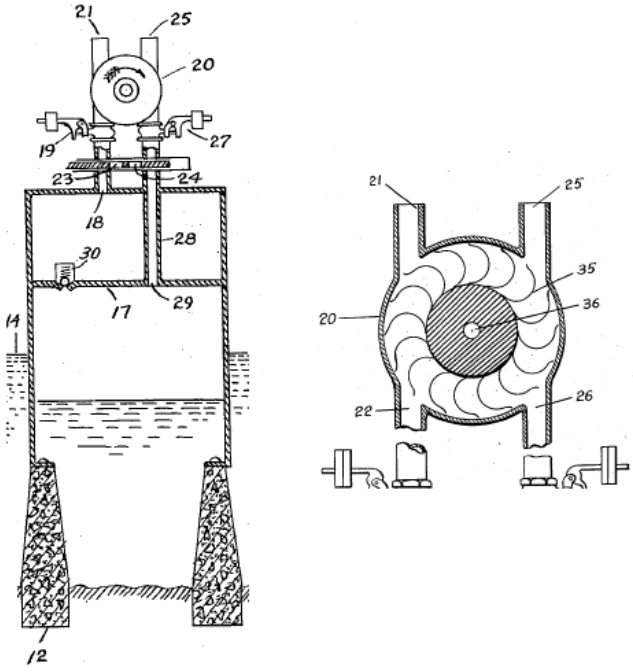

Fig. 2.8 Hydro-pneumatic power plant (Paulson, 1949)

Navigation buoys require a source of electrical energy to power lights. Storage batteries were initially used but found that they had to be regularly replaced. It was then pursued alternative means of in-situ power generation. The bobbing motion of the buoy was seen as a suitable source of energy as it is a desirable design feature for stability and visibility reasons. Corbett et al. (1962) filed the first patent on a hydro-pneumatic powered navigation buoy, however it was recognised that could be applied to any floating body or structure. Fig. 2.9 depicts a 2-watt direct current unit which embodies an open-ended standpipe in which the water enters and exits which alternatively raises and drops the free-surface level. The air inside the plenum then flows through a turbine due to the water motion. This invention presents four variants: (1) single-rotor turbine without check-valves, (2) single-rotor turbine with check valves, (3) dual-rotor turbine, one of which is operated only during the intake stroke and the other only on the exhaust stroke, and (4) dual-rotor turbine in which both rows rotate in the same direction.

Despite several inventions were conceived at the end of the 19^{th} century and first half of the 20^{th} century, there is no formal evidence of application of the any of the concepts described above. However, an important breakthrough happened in the 1960s decade, a wave-powered navigation buoy concept engineering by Masuda (1965) was the first-ever commercially available device based on the oscillating water column technology. Fig. 2.10 depicts an schematic view of the navigation buoy and the work cycle. The concept was similar to that proposed by Corbett et al. (1962), yet a check valve system was needed as a conventional unidirectional-flow turbine was implemented.

Early OWC devices were comprised of the three converting elements (chamber, turbine, and electric generator), however valve system were required to supply the turbine with a single-direction airflow. Such arrangements were abandoned due to reliability issues of the valves and poor efficiency in generating electrical power. Wells (1980) proposed the first turbine adapted to be driven by a reversible air flow whilst the rotor of such a de-

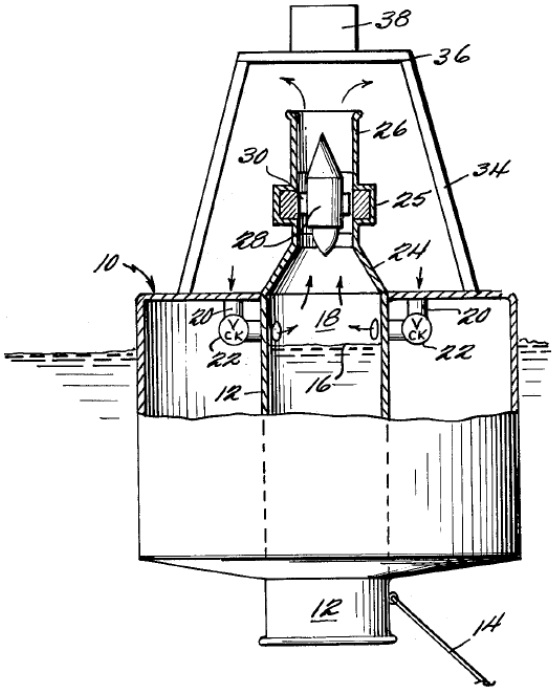

Fig. 2.9 Power generator actuated by wave motion (Corbett et al., 1962)

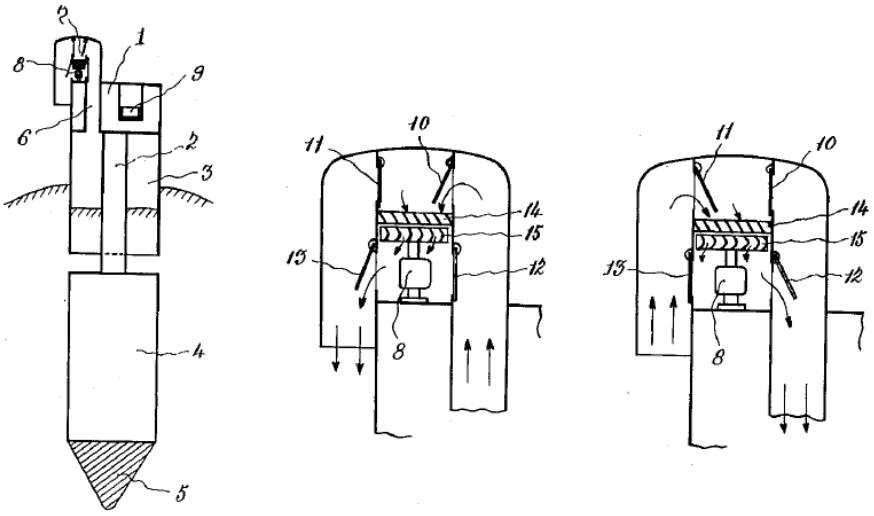

Fig. 2.10 Navigation buoy (Masuda, 1965)

vice is driven in a single sense of rotation during operation (see Fig. 2.11). Therefore, this machine enabled the removal of the valve systems to rectify the flow. This turbine type has been widely used since its invention and it will be analysed in more detail in the following sections. Wells (1983) also proposed a navigation buoy powered by such a turbine.

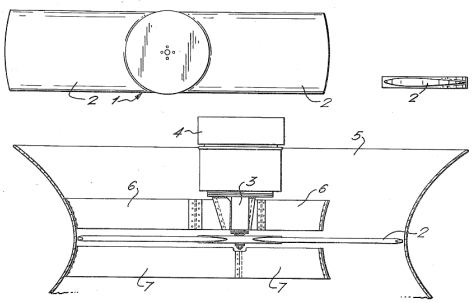

Fig. 2.11 Original Wells turbine rotor (Wells, 1980)

Moody et al. (1980) filed a patent on an asymmetric OWC. This patent also included some novel features such as the rounded lip at the front wall (see Fig. 2.12). The inlet air was sucked into the chamber without producing any useful work, and then, the exhaust air was discharged through a turbine to supply power to an electric generator.

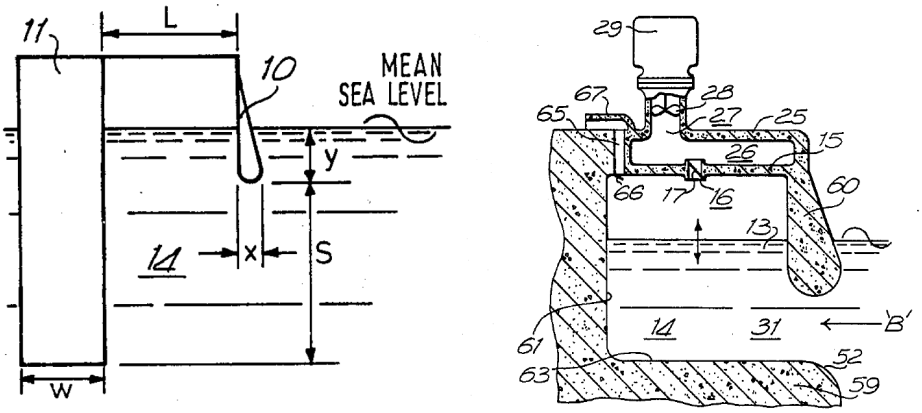

Fig. 2.12 Device for wave power extracting (Moody et al., 1980)

Chamber dimensions for maximum *power absorbtion efficiency* are also given by Moody et al. (1980):

1. Water column resonant frequency f_0 tuned to the incoming waves (see Fig. 2.12 for nomenclature):

$$f_0 = \frac{1}{2\pi}\sqrt{\frac{g}{y+\frac{\pi L}{4}}} \tag{2.1}$$

2. Proposed dimension ranges:

   (a) $L \leq s \leq 2.0L$

   (b) $0.25L \leq y \leq 0.5L$

(c) $0.50y \leq x \leq y$

(d) $L \leq W \leq 3.0L$

Chamber dimensions for maximum *power efficiency* are also given:

1. Wavelength of incoming waves λ_0 (see Fig. 2.12 for nomenclature):

$$\lambda_0 = \frac{g}{2\pi f_0} \tag{2.2}$$

2. Proposed dimensions:

(a) $L = 0.1\lambda_0$

(b) $s = 0.67L$

(c) $y = 0.40L$

(d) $x = 0.25L$

Ambli (1982) proposed a wave energy power station comprising to water-filled chambers communicating at the bottom being one of each open at the upper end to the sea leading to an U-shape water column. An intermediate moving wall or equivalent system could has been added to have the facility to adapt the resonant frequency of the water column to the existent sea state. Several configurations of the second chamber have been defined, one of which was suitable for an air turbine power off-take as shown in Fig. 2.13. In such an arrangement, the second chamber is communicated to the atmosphere through a turbine.

Boccotti (2007) studied the U-OWC device which allows to decrease the resonant frequency of the water column without increasing the draft of the device (which would reduce the capture efficiency). This modification enabled the harvesting of swell rather than large wind waves which allowed to install OWC in the Mediterranean Sea (cf. Boccotti, 2012).

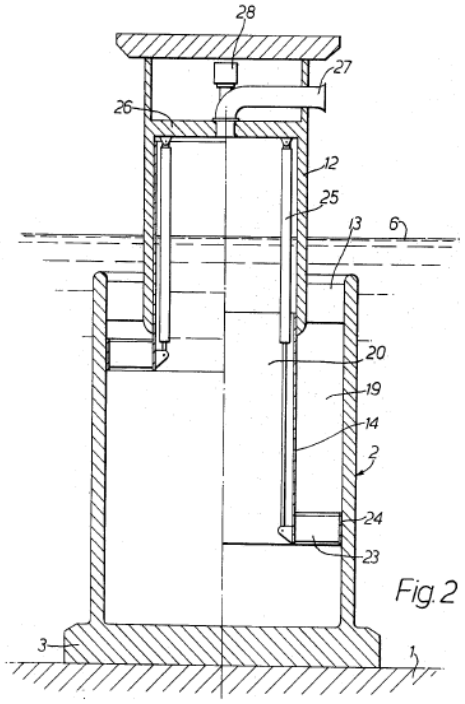

Fig. 2.13 Wave power energy power station (Ambli, 1982)

2.2 Capture chamber

The chamber or caisson is the element in which the hydrodynamic wave energy is transformed into pneumatic energy. The energy conversion process is extremely complex (see Fig. 2.14) in which incident waves are diffracted and absorbed, whilst the pressure fluctuations radiated waves back into the free field. The external wave field in the vicinity of the OWC is composed by the interference of the three wave fields: incident, diffracted, and radiated.

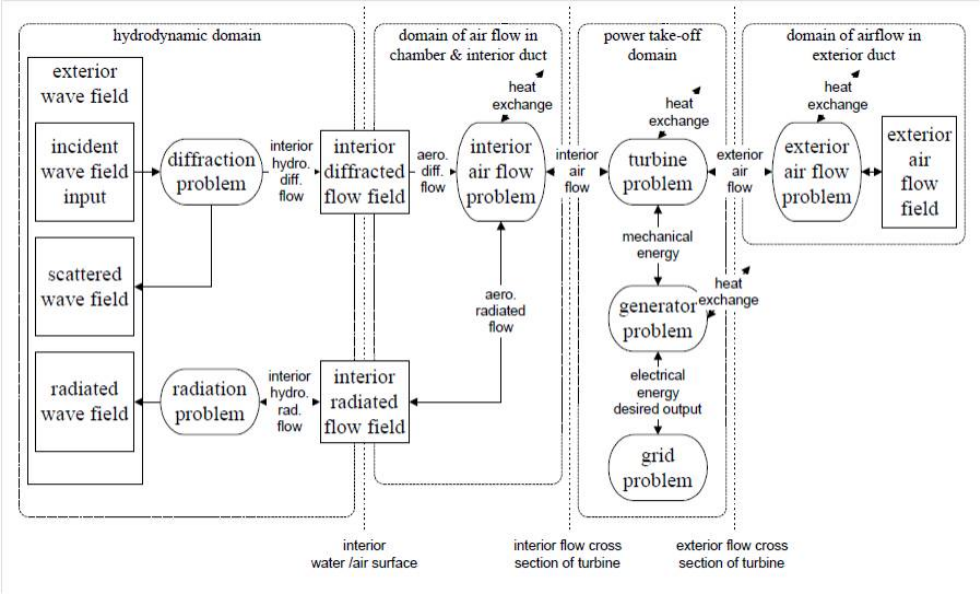

Fig. 2.14 OWC domains and their problems (Weber et al., 2001)

The energy communicated from the external flow field may force the water column oscillations which pressurises and decompresses the air trapped in the chamber volume. The pressure difference between the chamber and the atmosphere is set by the power turbine characteristics. Air compressibility in the chamber has a penalising impact on overall OWC power plant performance as described by Thakker et al. (2003). Therefore, turbine characteristics have a direct impact on overall efficiency as the may enhance energy loss due to air compressibility. Furthermore, greater pressures in the chamber will

increase energy loss due to wave radiation.

Chamber dimensions and geometry have to be tuned to match the the sea wave spectrum at the location where the OWC power plant will be installed. the transmissibility of the water column is maximum at resonance conditions, therefore the column has to be tuned to the dominant wave frequencies in the sea state in order to maximise the column, and hence, the overall plant efficiency.

Coupling effects have been also investigated in the literature (see Weber et al., 2001). The chamber-turbine interaction have been found stronger at maximum efficiency conditions.

2.2.1 Performance Analysis

An early linear theoretical model was proposed by McCormick (1974). This model was apply to a navigation buoy system and it predicted peak efficiency of power conversion at the resonant frequency of the combined buoy and water column system. A secondary peak was observed at the water column resonant frequency. Maximum conversion efficiency was found to be a function of the water column length.

This initial theoretical model was further developed by McCormick (1976). It was based upon the following assumptions:

(1) Regular monochromatic sea waves excite both the heaving motion and the water column oscillations. Adequate frequency separation between both is enforced.

(2) Internal water column motion is independent of buoy heave motion.

(3) Deep-water linear wave theory is applied.

(4) Air pressure on the internal free surface is negligible, therefore turbine and chamber are decoupled.

(5) Buoy heaving motion velocity is much smaller than the water velocity.

(6) Lossless incompressible-flow turbine is assumed.

(7) Electric generator efficiency is not account for.

(8) Added mass correction is applied to the water column as a function of the water column length.

(9) Water column damping term is a function of the water flow speed, which is experimentally calibrated.

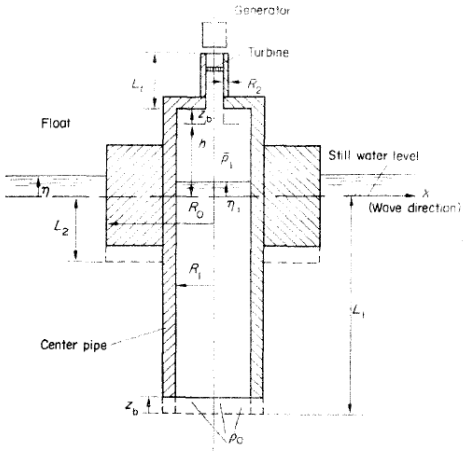

Fig. 2.15 Schematic diagram of the navigation buoy studied by McCormick (1974)

Eq.2.3 presents the model described above for which parameters and variables are shown in Fig. 2.15.

$$\rho_w A_1 L_1 \ddot{\bar{\eta}}_1 + b_1 \dot{\bar{\eta}}_1 + \rho_w g A_1 \bar{\eta}_1 = \rho_w \frac{Hg}{kR_1} \mathrm{e}^{kL_1} \mathrm{J}_1(kR_1)\cos(\omega t) \qquad (2.3)$$

where J_1 is the first-order Bessel function of the first kind.

This modified linear model showed satisfactory agreement with the experimental data. This simplified model explains the basic physics of the water column oscillation: a reactive energy transfer between inertial motion and hydrodynamic restoration forces.

However, the assumptions on the air system and turbine behaviour are insufficient as the pressure ratio or pressure difference between the chamber and the atmosphere determine the flow though the turbine, and not the displacement of the water column.

Oscillating rigid body theory was adapted to water column oscillations by Evans (1982). This model solves the boundary value problem to calculate the water velocity potential using Laplace's equation (see Eq. 2.4):

$$\begin{aligned} \nabla^2\Phi &= 0 && \text{in the fluid} \\ \frac{\partial\Phi}{\partial n} &= 0 && \text{at the walls} \\ \frac{\partial\Phi}{\partial z} - k\Phi &= -\frac{1}{\rho_w g}\frac{dP_i}{dt} && \text{on the free surface} \end{aligned} \tag{2.4}$$

where Φ is the velocity potential which can be expressed as a linear superposition of the incident velocity potential (Φ_0), the scattered field due to submerged solid walls (Φ_s), and the radiated field due to the pressure exert on the internal free surface (Φ_r). Eq. 2.5 presents the incident wave potential was expressed as a three-dimensional function.

$$\Phi_0(x,y,z,t) = \frac{gA}{\omega}\mathrm{e}^{kz}\cos(kx\cos\beta + ky\sin\beta - \omega t) \tag{2.5}$$

where β is the incidence angle of the wave train.

Evans (1982) also proposed equations to determine the maximum absorbed power and the resonant conditions based on a radiation volume flux

assumed a linear combination of the internal pressure and its first derivative. However, these equations need to be solved by numerical methods for each particular geometry. It was also demonstrated that only small differences occur between this model and models based on a rigid-body assumption for large wavelengths.

The main assumptions in this model are:

1. Incident wave potential based on the deep-water linear wave theory.
2. Linear turbine characteristics are assumed.
3. Air compressibility effect was neglected.

Again, the fact the the air compressibility was neglected, water column behaviour is decoupled from the turbine characteristics. This model was solved using Galerkin's method by Evans and Porter (1995). Further details on the radiation and the scattering problems. This model has demonstrated the ability to capture slosh mode resonances which could lead to very high amplitudes, however this oscillations do not produce useful work.

This model was extended by Brendmo et al. (1996) to include viscous and vortex shedding losses which were determined by experimental means. These were determined in a open chamber configuration (no power off-take) by two experiments: (1) measuring the power difference between the incident and the returned wave from the OWC, or (2) measuring the internal free-surface elevation subject to free-oscillations.

Sarmento and Falcão (1985) extended the surface pressure-induced wave model proposed by Stoker (1957) the effect of the following factors: (1) finite water depth, (2) air compressibility, and (3) turbine characteristics. Wave diffraction due to immersed structures is neglected. This extended model was applied to compute power absorption by a two-dimensional OWC device subject to a regular incident wave train.

It was demonstrated the air compressibility can have a significant impact. A linearised isentropic model has been found to produce satisfactory

results for small wave amplitudes. Capture efficiency has been calculated against breath-to-wavelength ratio for which unity values could be achieved as shown in Fig. 2.16. It has been also shown that chamber and turbine size can be greatly reduced. When nonlinear characteristics are considered, dependence on frequency and incidence amplitude are found, and, therefore, both variables need to be accounted for. The phase relationship between the flow through the turbine and the air pressure inside the chamber has been ascertained to have a powerful effect on capture efficiency. Detailed mathematical of this model can be found in Sarmento and Falcão (1985).

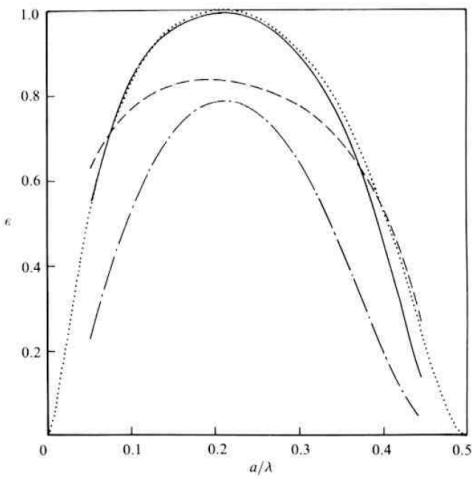

Fig. 2.16 Chamber efficiency against breath-to-wavelength ratio for various turbine characteristics (Sarmento and Falcão, 1985)

2.3 Power Turbine

Turbines for power off-take have to operate in very challenging conditions which are usually not ideal for turbomachinery for which a well-defined operation condition is required.

The flow supplied by the motion of water column are the following:

1. Irregular bi-directional flow (which might have certain periodicity). This implies off-design operation for majority of the work-cycle.

2. Wide mass flow range resulting from wave amplitude and on- or off-resonance operation of the the water column.

3. Speed of rotation set by the electric generator and drive train gear ratio. The sense of rotation has to be the same regardless of the direction of the flow through the turbine.

There are two system architectures which allow to extract energy from the airflow in the aforementioned conditions:

1. Conventional turbine with check valves: The check valves and the turbine are arranged in such a way that one-directional flow is supplied to the turbine (see Fig. 2.17). The main advantage of this architecture is high efficiency of the turbine. However, for large power systems, valve energy loss, reliability, and large maintenance burden make this configuration a bad candidate for OWC power plants. It has been successfully implemented for small-scale devices, such as navigation buoys.

2. Self-rectifying turbines: These kind of machines have lower peak efficiency than the conventional turbines, but the overall efficiency is improved because the auxiliary check valves can be removed. Power plants implement this architecture as higher reliability and plant efficiency are required for electricity production.

Several self-rectifying turbines have been developed for OWC power plants which aimed at efficient and reliable power conversion. They can be classified in three main groups:

(1) Wells-type turbines.

(2) Impulse-type turbines.

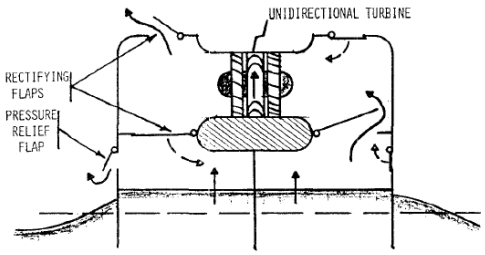

Fig. 2.17 Pneumatic system a unidirectional turbine rectifying flaps (McCormick et al., 1992)

(3) Radial turbines.

These turbine types will be studied in the following sections.

2.3.1 Wells-Type Turbines

The original Wells turbine was designed by Alan Wells in 1976. The Wells turbine is composed of a single rotor (see Fig. 2.18) in the simplest variant. The rotor is integrated by straight NACA00XX aerofoils for which the plane of symmetry is perpendicular to the axis of the machine. There are other variants of this basic concept which include several co- or contra-rotating rotors, or guide vanes upstream or downstream. More complex concepts have been developed in which the guide vanes a pitched-controlled.

The working principle of the Wells turbine is very simple. The blades experience a lift force which is proportional to the dynamic head of the flow and the lift coefficient, which is function of the flow incidence. The lift force on each blade generate a torque on the machine shaft (see Fig. 2.19).

Among all the self-rectifying turbines for OWC power off-take, the Wells turbine is the simplest concept and most widely spread which can be easily manufactured at low cost. However, many limitations have to be solved:

1. Although the peak efficiency is the highest among the self-rectifying turbines, such an efficiency steeply drops above relatively moderate

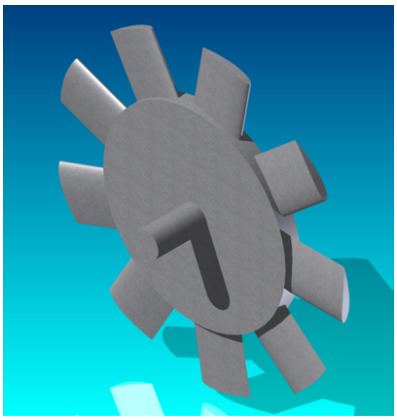

Fig. 2.18 Wells turbine rotor

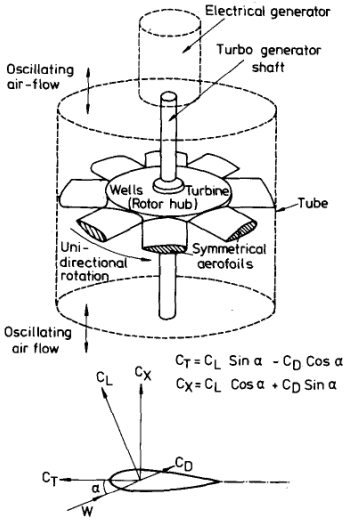

Fig. 2.19 Wells turbine working principle (Raghunathan, 1995)

flow coefficients, and therefore, the operating range is very narrow. As a result, the time-averaged efficiency under alternating flow conditions is severely penalised as highest mass flow rates do not produce any work (torque).This performance shortfall is produced by aerofoil stall. This phenomenon has been studied in CITE. Several authors have tried to improved the operating range of the Wells turbine by: (1), (2), (3) ... Another consequence of blade stall is big torque variations may lead to high-cycle fatigue. At low mass flow rates, the profile drag is too large, and the turbine does not produce any torque.

2. The unsteady working line differs from the steady characteristics, as the flow suffers from hysteresis effects. This phenomenon has been studied by Raghunathan (1995); Setoguchi et al. (2003). This effect can be explained by the asymmetric behaviour of separated boundary layers on blade surfaces and the oscillations of the blade wake, which becomes more dominant at low Reynolds numbers.

3. Depending on the rotor design, the Wells turbine might not be able to self-start (Raghunathan, 1995). Depending on the solidity and hub-to-tip rations, the turbine might experience *crawling*, in which the turbine torque curve has three regimes as speed increases: turbine, compressor, and turbine. The fact that the compressor mode exists, prevents the rotor to speed up to the design speed. This phenomenon is due to the torque-incidence characteristics.

4. High speed of rotation which increases turbine start-up. Therefore, power plant operation may be severely penalised if the starting process is repeated frequently. High tip speeds have a detrimental effect on noise emissions (Takao et al., 2002b).

5. High alternating axial thrust which requires an auxiliary system to avoid cyclic bearing load crossover. This system increases cost and maintenance burden.

In order to try to mitigate or fully solve the limitations of the Monoplane Wells Turbine without guide vanes(MP), several variants of have been proposed (see Fig. 2.20):

1. Monoplane Wells Turbine with Guide Vanes (GV): This turbine embodies downstream and upstream stator vanes to the MP turbine rotor. The upstream vanes add co-swirl (see Fig. 2.20(b)) to the incoming flow to the rotor. The co-swirl increases the incidence onto the rotor which reduces flow coefficient at which stall occurs as shown in Fig. 2.21. Other authors have reported a delay of the stall onset (Gato and Falcao, 1990; Setoguchi et al., 2001). However, the main advantage of the GV Wells turbine derives from the recovery of outlet rotor swirl by the downstream vanes resulting in increased efficiency over the working range (see Fig. 2.21). Three-dimensional vane designs have been proposed in the literature (Setoguchi et al., 2001) which take into account the distribution of peripheral speed of the rotor. This feature increases the range of operation of the turbine which overshadows a modest increase in peak efficiency as shown in Fig. 2.24. This turbine has been installed in the OWC power plant located in Pico (Azores).

2. Single-shaft Biplane Wells Turbine (BP): Pressure drop for this turbine could exceed twice the value of the MP. It can also produce twice as much power when compared to the MP. For a given turbine damping ($\Delta P/Q$), low solidity BP efficiency outperforms the equivalent high solidity MP. The normalised torque drops, however the pressure drop reduction overbalances it (see Figs. 2.21 and 2.22). The BP turbine has superior starting characteristics (Raghunathan and Tan, 1983). The main difference between MP and BP is the gradual efficiency drop of the latter when stall conditions are encountered

3. Contra-rotating Wells Turbine (CR): Rig testing showed superior aerodynamic efficiency that the BP Wells turbine (Raghunathan and Beattie,

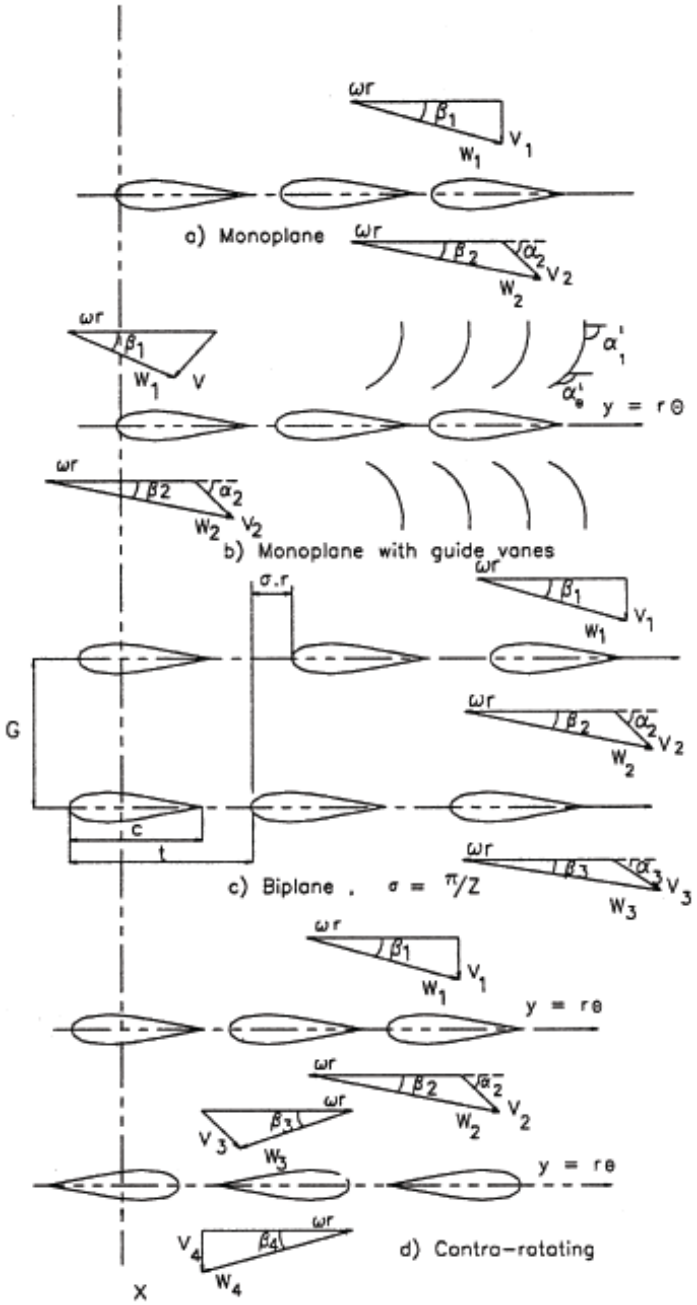

Fig. 2.20 Wells turbine variants and velocity triangles. From top to bottom: (a) monoplane turbine (MP), (b) monoplane turbine with Guide vanes (GV), (c) single-shaft biplane turbine (BP) ,and (d) contra-rotating turbine (CR) (Curran and Gato, 1997)

1996). Both GV and CR Wells Turbines partly recover flow swirl for which kinetic energy loss is proportional. It has been proven to operate stall free over a wide range of flow rates. This variant also offers a much lighter turbine damping (see Fig. 2.21). A 500kW CR Wells turbine was commissioned and tested in the LIMPET Power Plant. Turbine predicted damping satisfactorily agreed with the measured damping characteristics (see Folley et al., 2006). However, large errors were found between the efficiency predictions and measurements. The lower measured efficiency has been reported to be caused by a flow distortion and flow settling time. It has also been noted that this turbine suffers from higher hysteresis effects due to: (1) transient working line due to accelerating and decelerating flow, (2) both rotors switching from upstream to downstream during flow reversal, and (3) higher settling time for the flow (around 20-30 s measured during constant flow testing).

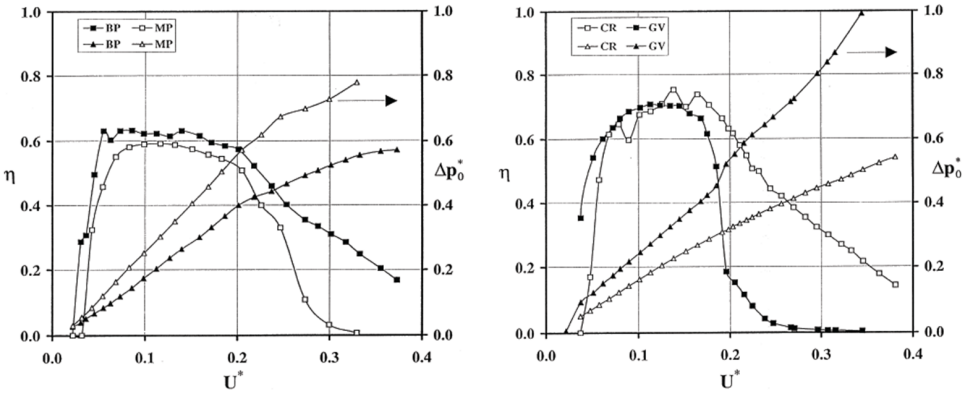

Fig. 2.21 Efficiency and pressure drop for a monoplane turbine (MP) and biplane turbine (BP) (left), and for a contra-rotating turbine (CR) and monoplane turbine with guide vanes (GV) (right) (Curran and Gato, 1997)

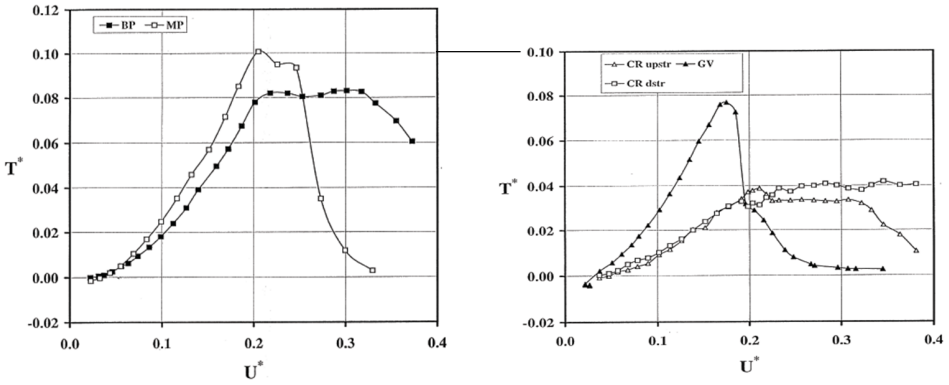

Fig. 2.22 Torque coefficient for a monoplane turbine (MP) and biplane turbine (BP) (left), and for a contra-rotating turbine (CR) and monoplane turbine with guide vanes (GV) (right) (Curran and Gato, 1997)

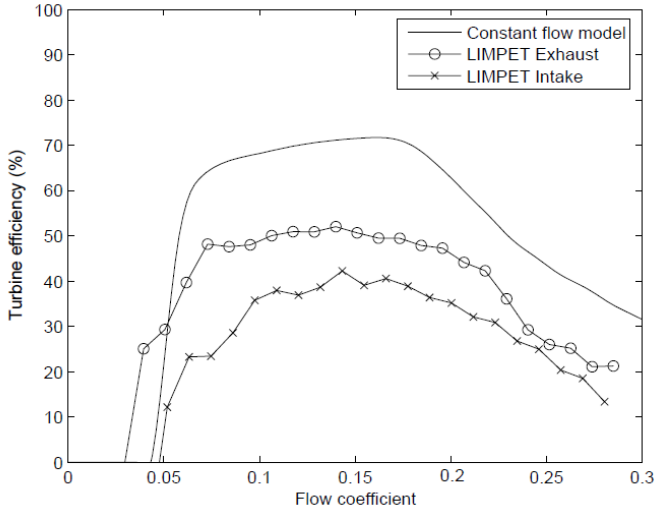

Fig. 2.23 Comparison of LIMPET measured efficiency and predictions (Folley et al., 2006)

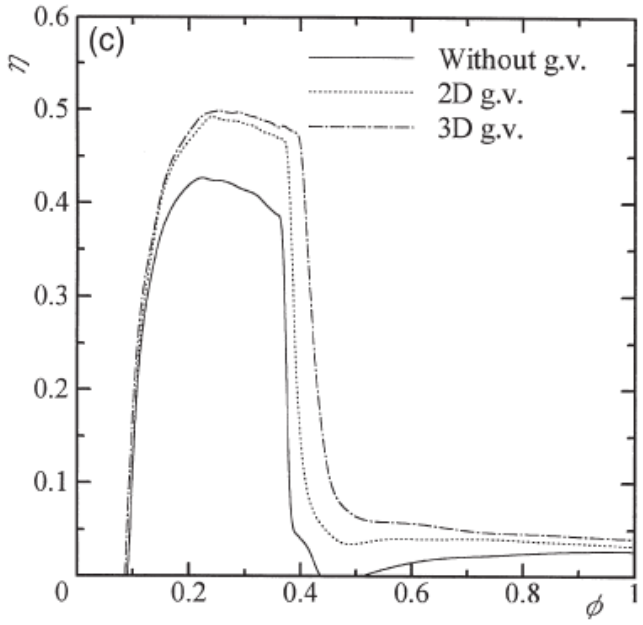

Fig. 2.24 Effect of 2D and 3D guide vanes on Wells turbine efficiency (Setoguchi et al., 2001)

2.3.2 Impulse-Type Turbines

Several patents were filed on a new type of turbines power off-take in Oscillating Water Columns, the so-called *impulse-type turbines*, at the end of the 70s:

1. Babintsev (1975) filed a patent in Apr 1974 on an impulse-type turbine composed on a rotor, and upstream and downstream guide vanes. This turbine was aimed at producing electricity for a navigation buoy replacing the check-valve system.

2. Modisette (1981) presents an impulse type turbine composed by a rotor, and upstream and downstream guide vanes. The application of this turbine was to produce electric power for buoys and remote off-shore structures. This patent was filed shortly after the previous patent in Jul 1974.

3. McCormick (1981) proposed a more complex impulse type turbine embodies two contra-rotating rotors, and guide vanes located both upstream and downstream. Both runners are connected by a bevel-gear system which enables same-speed rotation of both shafts but in opposite directions.

Between 1984 and 1985, demonstrator testing was carried out on the *Kaimei*, floating wave power plant (cf. Richards and Weiskopf, 1986). A 450 rpm rated-speed McCormick turbine was tested. The turbine characteristics were mapped by measuring turbine power, efficiency, and mass flow rates as a function of pressure difference and speed of rotation (see Fig. 2.28). Nozzle stagger angle was optimised as the turbine had the facility to modify this parameter. However, guide vane design resulted in high exit flow deviation which was inferred from the fact of increased flow at a given speed. Improved efficiency could be achieved if guide vanes are redesigned taking into account viscous effects. It was noted that the McCormick turbine removes the axial

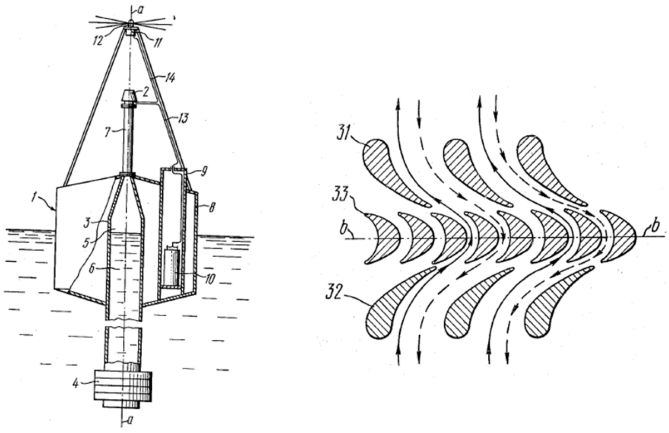

Fig. 2.25 Impulse-type turbine concept for navigation buoys (Babintsev, 1975)

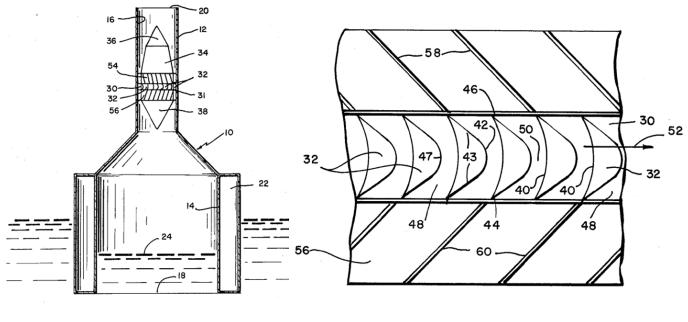

Fig. 2.26 Impulse-type turbine concept for OWC power off-take (Modisette, 1981)

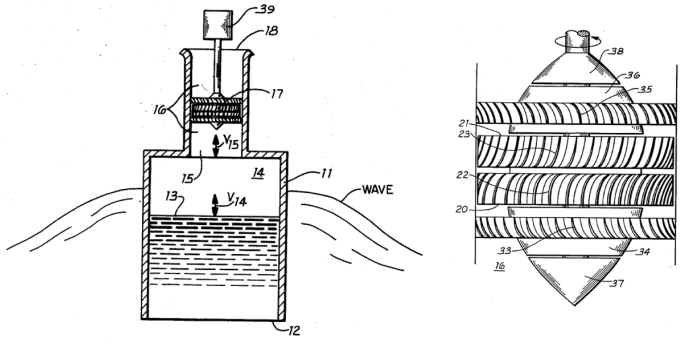

Fig. 2.27 Contra-rotating impulse-type turbine concept (McCormick, 1981)

thrust problem with the dual rotor-split flow design and noise generation is lower to that of an equivalent Wells turbine.

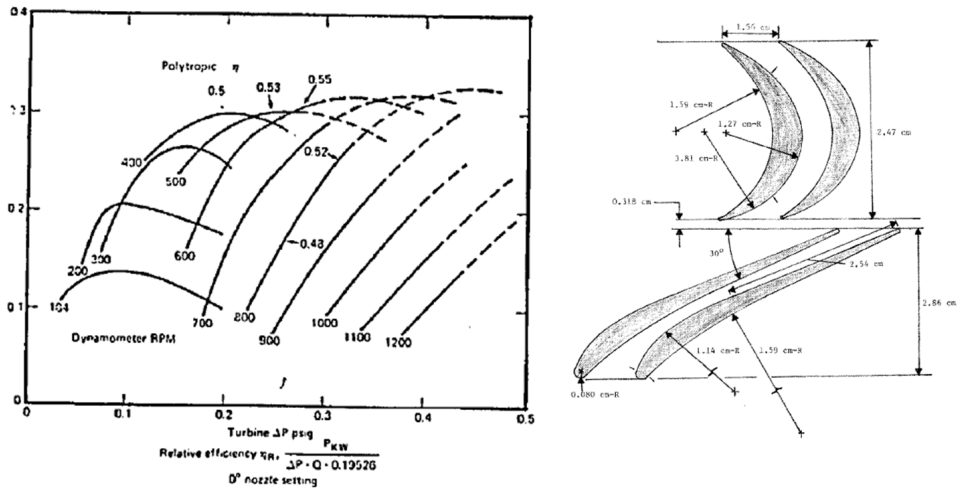

Fig. 2.28 McCormick turbine measured efficiency curves (left Richards and Weiskopf, 1986), and and sketch of rotor-stator pair (right McCormick and Surko, 1989)

The first published study on a single-rotor impulse-type turbine performance was carried out by Setoguchi et al. (1988). The objective of this design was to overcome the limitations of the Wells-type turbines: (1) poor efficiency characteristics –the turbine suffers from stall at high flows–, and (2) poor starting characteristics –it may exhibit *crawling* being unable to self-start–.

Fig. 2.29 depicts the first proposed design was a self-controlled pitch axial impulse turbine. In such a turbine, the rotor was designed based on high-pressure steam turbine buckets. Upstream and downstream stationary rows were added in order to guide the flow into the rotor. Downstream stator rows are usually referred as de-swirl vanes as their purpose is to straighten the flow to the axial direction. This vanes had the ability to rotate about the edge which is closer to rotor as shown in Fig. 2.29. The motion of these vanes is induced by the bi-directional air flow.

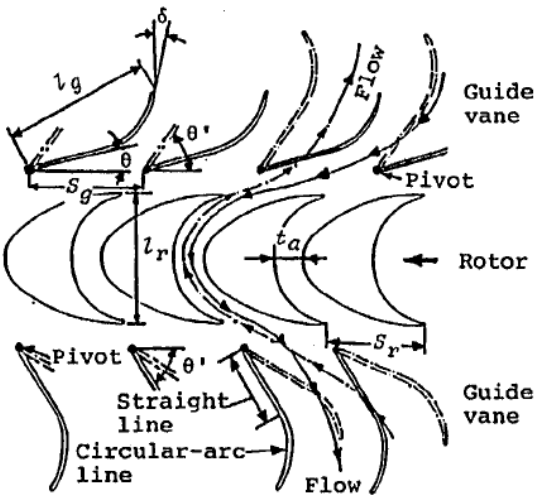

Fig. 2.29 Impulse turbine with self-controlled pitch vanes, blade-to-blade view (Kaneko et al., 1991)

Fig. 2.30 presents the cycle efficiency comparison for the self-controlled pitch impulse turbine, and the MP and BP wells turbines. The impulse turbine has higher cycle efficiency over a much wider flow range as it does not suffer from stall unlike the Wells turbine. Additional benefits have been reported such as: (1) lower speed of rotation, and (2) better starting characteristics. However, the moving parts greatly increases the maintenance burden.

Test rig results shown by Kaneko et al. (1991) have been confirmed in an breakwater power plant demonstrator. Fig. 2.30 presents the power output of a 1m-MP Wells turbine and the equivalent Impulse turbine under identical wave conditions. The Wells turbine losses efficiency at high power inputs as the power output is flat irrespectively of the wave input power. The Impulse turbine produces more power and its efficiency is more or less constant with the power input.

In order to eliminate maintenance problems due to moving parts in the self-controlled pitch impulse turbine, a fixed-vane impulse turbine has been proposed by Maeda et al. (1999). Rig testing was carried out in order to

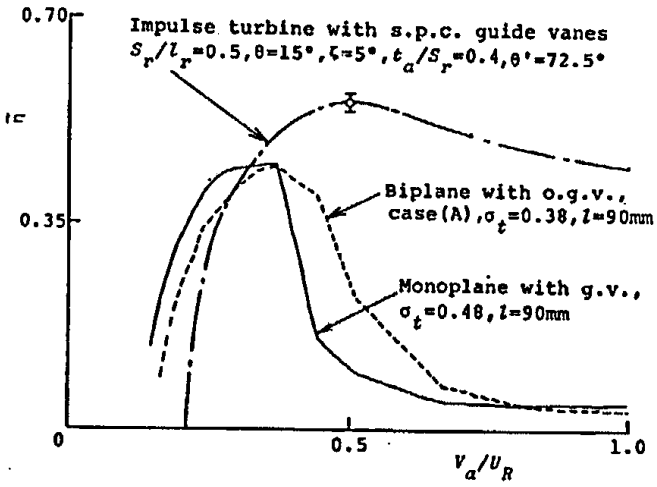

Fig. 2.30 Comparison of cycle efficiency for self-controlled pitch impulse turbine, and MP and BP Wells turbines (Kaneko et al., 1991)

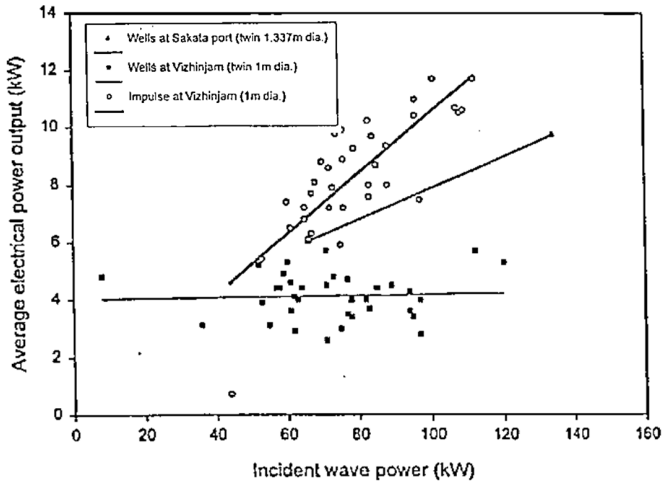

Fig. 2.31 Performance of Vizhinjam OWC power plant with Wells and Impulse turbines (Santhakumar et al., 1998)

determine the optimum stagger angle of the vanes (see Fig. 2.32). The turbine was tested under sinusoidal flow conditions. Numerical simulations were then utilised to compute starting characteristics and performance under irregular flow conditions. Fig. 2.33 presents the comparison of the impulse turbine and a Wells turbine efficiency and starting characteristics both of which were superior for the former.

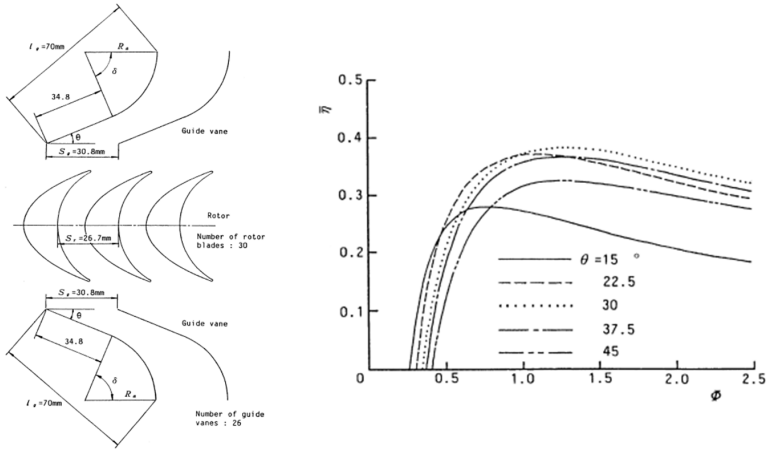

Fig. 2.32 Geometry definition of an impulse turbine with fixed guide vanes (left), and efficiency characteristics for various stagger angles (right) (Maeda et al., 1999)

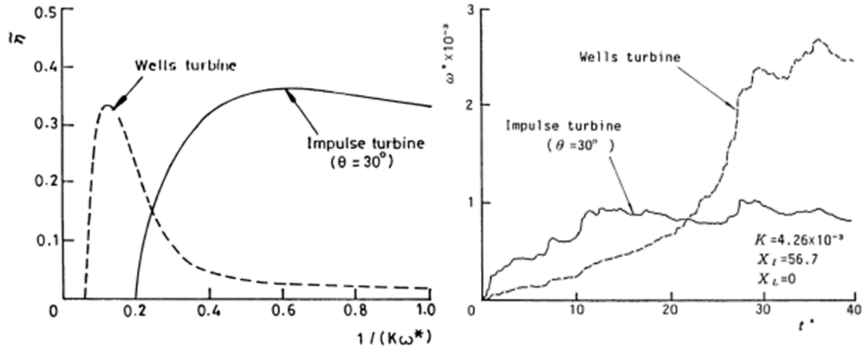

Fig. 2.33 Fixed-vane impulse and Wells turbines efficiency (left) and starting characteristics (right) under irregular wave conditions (Maeda et al., 1999)

Setoguchi et al. (1999) investigated the effect of guide vane geometry. Two different designs were rig tested and compared: (1) plate guide vanes, and (2) aerofoil guide vanes. Fig. 2.34 presents cycle efficiency for both guide vane designs in which the aerofoil guide vanes show no benefit in terms of cycle efficiency, however plate guide vanes cannot withstand buffet resulting from flow separation (see Vieira et al., 2015).

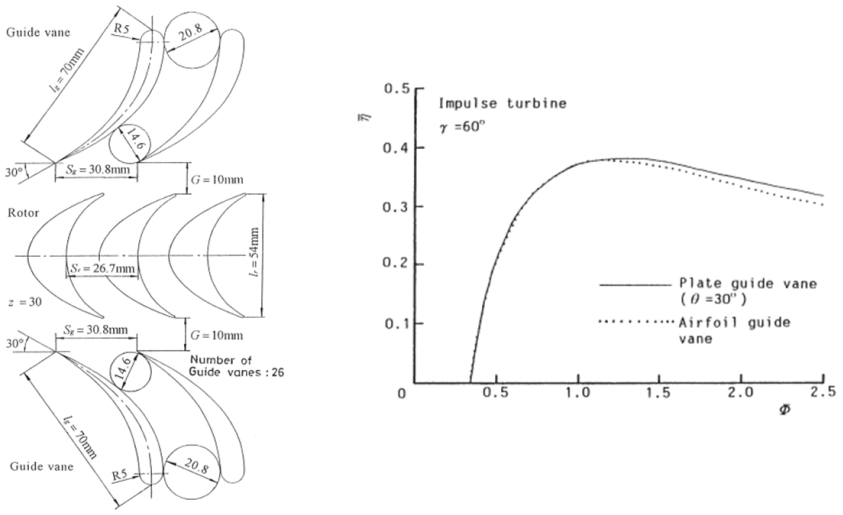

Fig. 2.34 Aerofoil vane impulse turbine geometry (left), and cycle efficiency comparison (right) for plate and aerofoil guide vanes (Setoguchi et al., 1999)

Thakker et al. (2005) performed rig testing measurements on two types of guide vanes: (1) straight or 2D vanes, and (2) twisted or 3D vanes. The 3D vanes were designed following the free-vortex theory. The aim of the twist is to reduce the leading edge separation during off-design operation. Fig. 2.35 (left) presents the overall characteristics for the impulse turbine embodying 2D and 3D vanes. It shows an average improvement of 4.5% in efficiency. Spanwise traverse measurements were carried out using a 5-hole probe to determine velocity profiles downstream of the guide vanes which showed reduced flow deviation. Thakker et al. (2005) also reported larger hysteretic loops (see Fig. 2.35 (right)) to those of Wells turbines found by Setoguchi

et al. (2003).

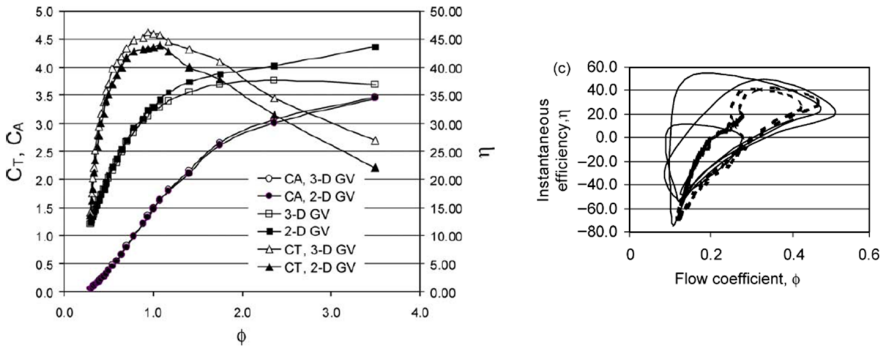

Fig. 2.35 Aerofoil vane impulse turbine geometry (left), and cycle efficiency comparison (right) for plate and aerofoil guide vanes (Setoguchi et al., 1999)

Aerodynamic rotor design has been studied by Takao et al. (2002a). Four different rotor geometries were designed, manufactured, and rig tested in order to optimise turbine performance based on rotor design factors (see Fig. 2.36). Type I and IV have con-di passage shape, Type II has a constant passage area, and Type III convergent passage area. Fig. 2.37 depicts turbine efficiency for each of the aforesaid rotor geometries. Type I and IV show higher peak and off-design efficiency which indicate that con-di passage area shape maximises impulse turbine efficiency, whilst convergent passage area shape (Type III) penalises turbine efficiency. Takao et al. (2002a) claim that the best rotor design is Type I based on peak efficiency. However, better off-design efficiency would suggest that a more robust solution would be Type IV which also has the smallest maximum thickness-to-chord ratio among the investigated designs.

Rotor geometries proposed by Takao et al. (2002a) were designed using Hamajima's rules. However, this method is intended for supersonic turbines. Fig. 2.38 shows the flow patterns for a supersonic impulse turbine with 0% contraction ratio. The compression waves separate the suction side boundary layer, therefore, higher efficiency designs incorporate certain contraction ratio (8% on the design on the right) ir order to suppress the flow separation.

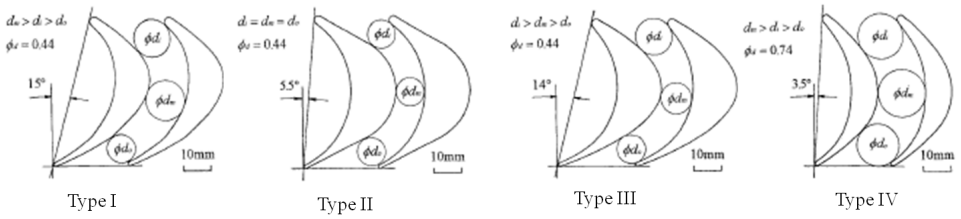

Fig. 2.36 Impulse turbine rotor geometries (Takao et al., 2002a)

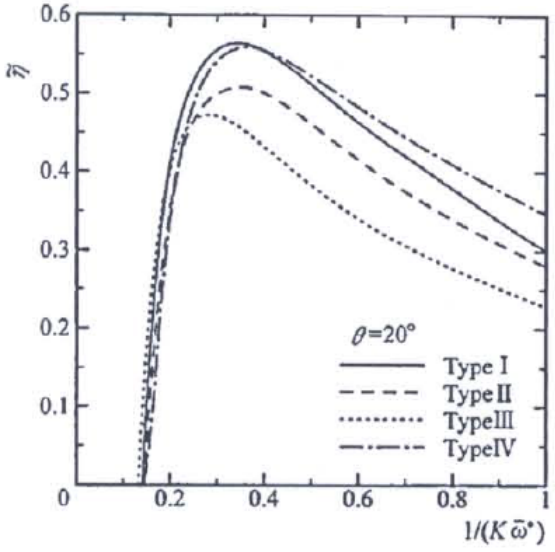

Fig. 2.37 Efficiency characteristics of four rotor designs (Takao et al., 2002a)

Impulse turbines for OWC power off-take efficiency is penalised if passage contraction is used. This fact highlights the need for specific rotor design rules which are not derived from supersonic impulse turbine but specifically for bi-direction subsonic flow.

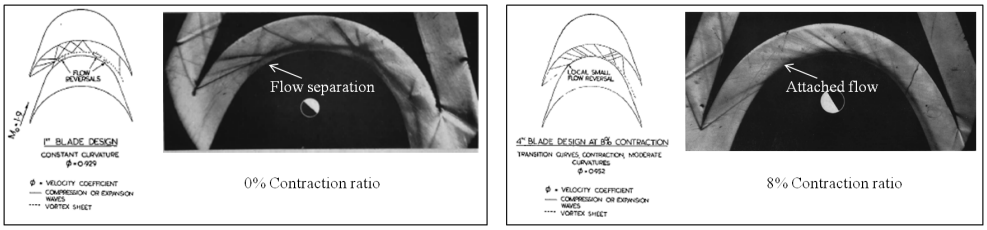

Fig. 2.38 Schlieren photograph on supersonic impulse turbine buckets with 0% contraction ratio (left) and 8% contraction ratio (right) (Stratford and Sansome, 1962)

Most of the research in the literature is based on experimental rig or demonstrator testing. However, there is a scarcity in 3D viscous CFD simulations. A brief study was carried out by Thakker et al. (2001) which objective was to compare and to validate CFD analysis of an impulse turbine. The incompressible flow CFD analyses were carried out on a single-passage 2D section using a fully triangular grid. Several turbulence models were investigated and wall models were utilised. CFD results showed similar trends to experimental data, however further work would be needed to accurately predict impulse turbine characteristics.

Further work has been carried out in order to improve the accuracy of CFD simulations. Thakker and Dhanasekaran (2004) generated a 3D hexahedral mesh with tip clearance which would be able to solve secondary (endwall) and tip leakage flows. Three meshes were investigated and several tip clearances were simulated which showed that efficiency is not affected by tip clearances smaller than 1%, steeply falling for greater tip gaps. Greater accuracy has been achieved (Fig. 2.39) by 3D simulations. However, greater prediction errors are still found away from peak efficiency, and CFD simulations overpredict both turbine torque and pressure drop which allow better

match of the turbine efficiency as both errors cancel each other out.

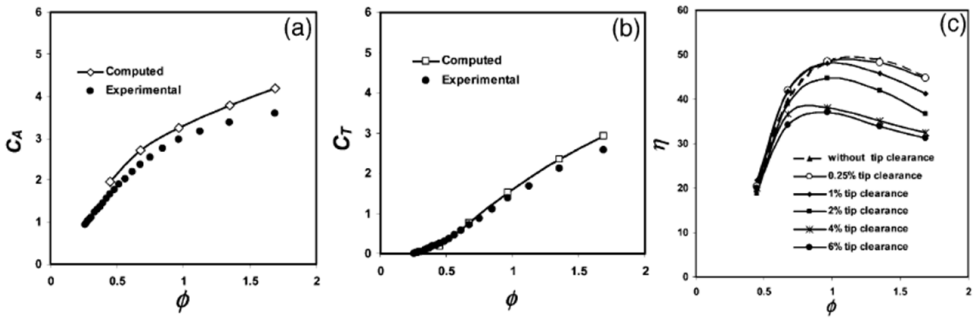

Fig. 2.39 (a) Input power coefficient (b) torque coefficient, and (c) efficiency for various tip gaps (Thakker and Dhanasekaran, 2004)

Thakker et al. (2005) investigated the loss generation mechanism both using rig testing and 3D CFD simulations. Measurements revealed that downstream guide vanes where responsible for the majority of the aerodynamic loss at low flow coefficients. Fig. 2.40 depicts CFD-calculated velocity contours which identify the following loss sources:

1. Upstream guide vane: Suction side separation (i) grows above $\phi = 1.0$ which slightly increase upstream guide vane total pressure loss.

2. Rotor: Two major loss sources are identified: (ii) leading edge separation on the pressure side, and (iii) mid-chord suction side separation. Total pressure loss increases with flow coefficient as suction side separation grows. A modest decrease in loss is observed at $\phi = 1.68$ as flow incidence approximates design incidence leading to a reduced leading edge separation on the pressure side. Accurately determining separation (iii) will play a major role in calculating turbine torque as outlet flow angles are greatly affected by this flow feature.

3. Downstream guide vane: Massive leading separation (iv) is present at the lowest flow coefficients contribute circa 40% of the overall total pressure loss. The leading edge flow separation is reduced as the flow

coefficient increases which can be seen in diminished loss coefficient down to approximately 10%.

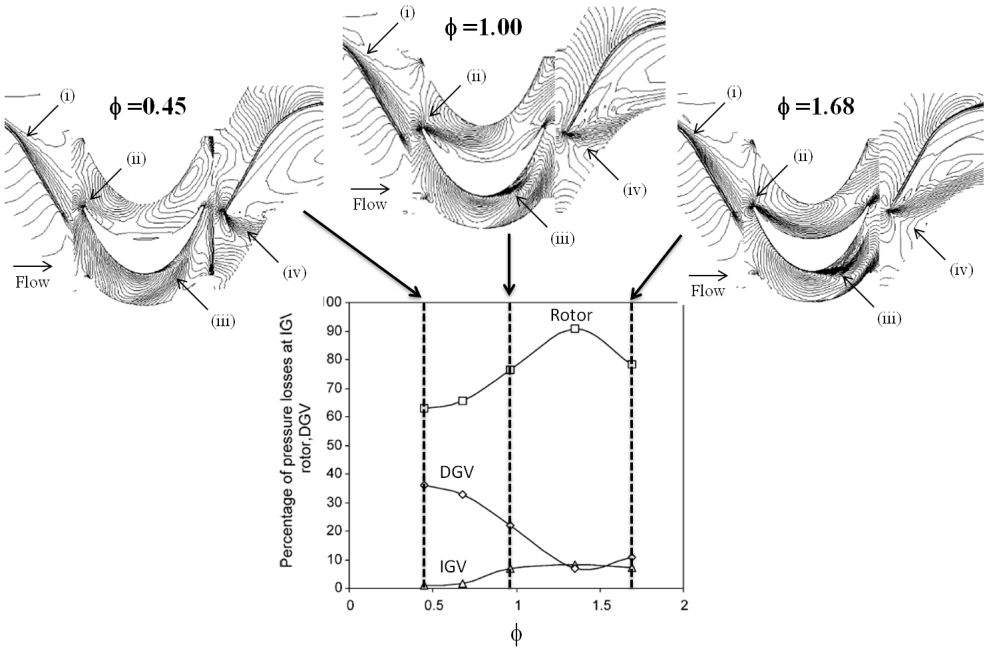

Fig. 2.40 Velocity contours near the tip section (top), and percentage total pressure drop at each blade row (bottom) (Thakker et al., 2005)

The effect of hub-to-tip ratio was studied by Thakker and Elhemry (2007) which demonstrated a performance benefit of 0.5 hub-to-tip ratio compared to 0.55 and 0.6.

2.3.3 Radial turbines

Radial turbines for OWC power off-take were introduced by McCormick et al. (1992). The proposed design embodies a single rotor with arcuate blades, upstream and downstream guide vanes. Because of the design, the shaft rotates in the same sense regardless of the flow direction throughout the

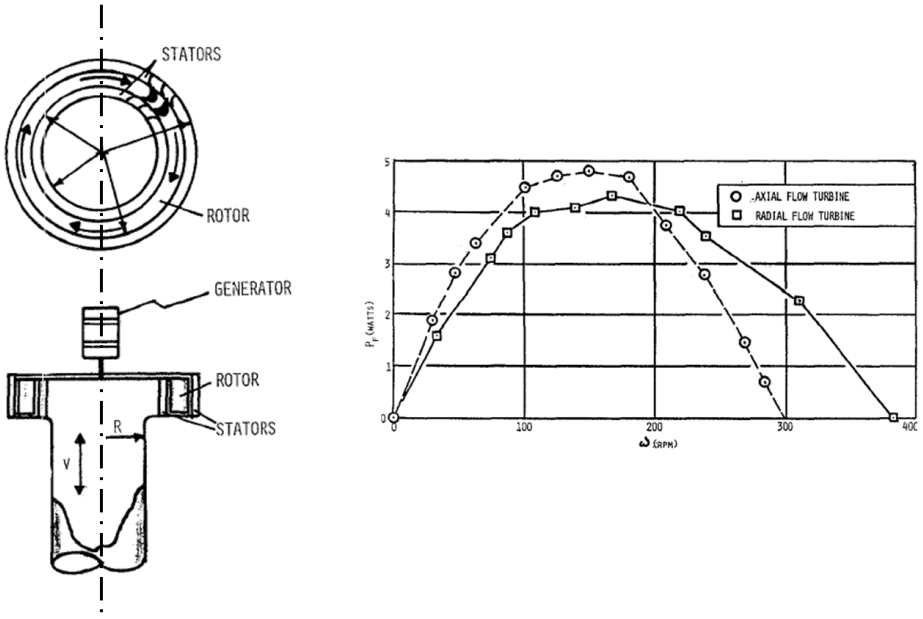

Fig. 2.41 Sketch of the bidirectional radial turbine and turbine maximum power compared with a contra-rotating impulse-type turbine (McCormick et al., 1992)

turbine. The radial turbine rotates at lower speeds and the runaway speed is higher than that of the impulse-type turbines (see Fig. 2.41).

Rig testing was performed by Setoguchi et al. (2002) on a single-rotor radial turbine at constant speed of rotation under sinusoidal flow conditions. Two different rotor stagger angles were tested and various stagger angles for the guide vanes. The two rotor configurations showed very little difference in terms of cycle efficiency and starting characteristics.

However, guide vane stagger angle have a powerful effect on cycle efficiency under sinusoidal flow conditions at constant rotational speed as shown in Fig. 2.43. Outer guide vane configuration have a more powerful effect that inner guide vanes. Steady performance is superior when operating as centripetal turbine which worsens if the flow is reversed working in centrifugal mode. Optimum stagger angles were defined based on turbine performance although as all vane configurations have similar starting characteristics. Peak

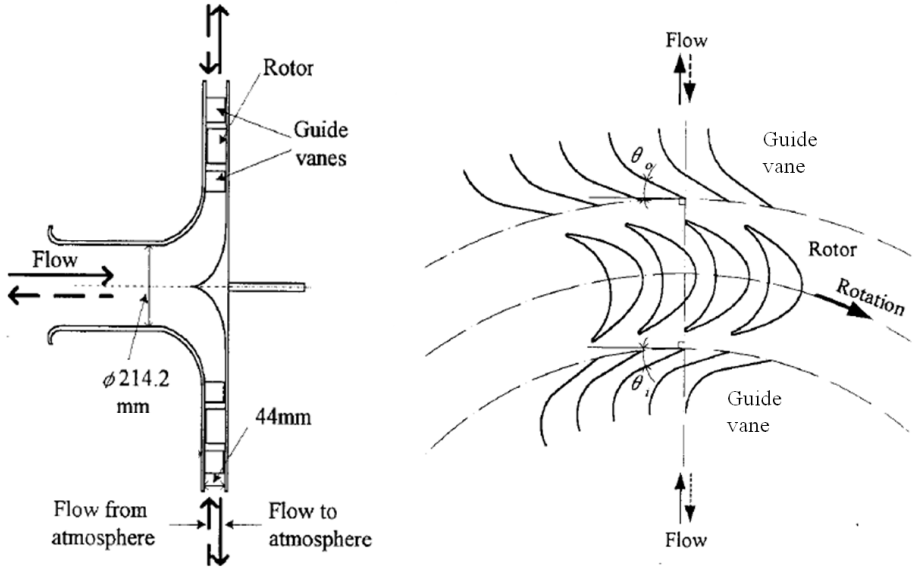

Fig. 2.42 (Setoguchi et al., 2002)

cycle efficiency is significantly lower to that of the impulse-type turbines (see Fig. 2.37 and Fig. 2.43).

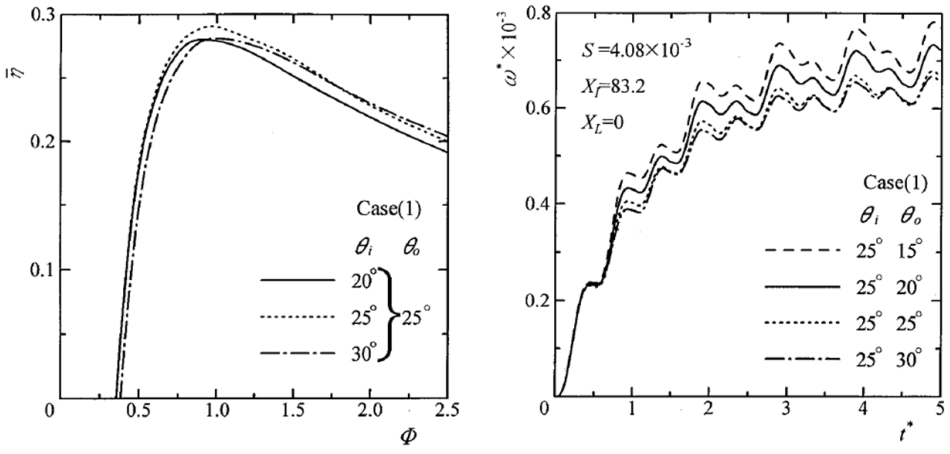

Fig. 2.43 Radial turbine cycle efficiency (left) and starting characteristics (right) (Setoguchi et al., 2002)

A radial turbine with variable-pitch guide vanes has been proposed by Takao et al. (2005) in order to improve the aerodynamic efficiency of the fixed-pitch vane radial turbine. Both inner and outer guide vanes had a bi-stable schedule, i.e. the vane stagger angle was set to a constant value during each phase of the work cycle. Rig testing was carried out in order to determine the optimum vane schedule which was found to improved peak cycle efficiency in excess of 10% (see Fig 2.44). On the other hand, mechanical complexity and control requirements had greatly increased which will also had an negative impact on mechanical reliability.

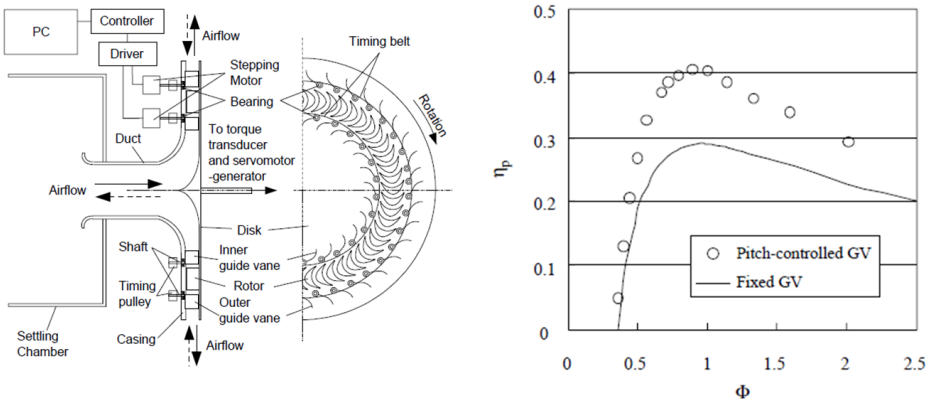

Fig. 2.44 Variable-pitch vane radial turbine scheme (left) and cycle efficiency comparison for both radial turbines with fixed- and variable-pitch guide vanes (right) (Takao et al., 2005)

The Fluid Dynamics Research Group at the University of Valladolid has extensively contributed to the understanding and improvement of the fixed-pitch vane radial turbine for OWC power off-take. El Marjani et al. (2008) developed a three-dimensional viscous computational model to analyse the radial turbine. Grid sensitivity studies were carried out to determine the adequate mesh density. Fig. 2.45 depicts the triangular prism mesh utilised and a good agreement between the predicted and measured torque and pressure coefficients.

Gonzalez et al. (2010) presents both an inviscid one-dimensional (low-

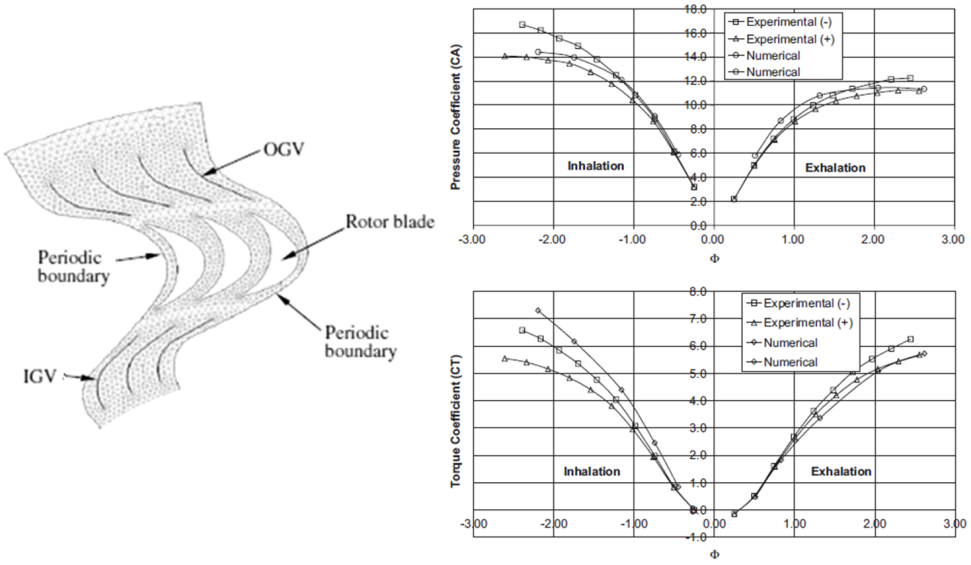

Fig. 2.45 Axial layer of computational grid (left), measured and predicted pressure coefficient (top right), and measured and predicted torque coefficient (bottom right) (El Marjani et al., 2008)

fidelity) and a viscous three-dimensional model (high-fidelity). The one-dimensional model does not include deviation effects and it is utilised to determine the turbine torque based on the Euler Equation, inviscid total pressure loss, and degree of reaction. The proposed 3D CFD model solves the incompressible flow equations using the Realizable $k-\varepsilon$ turbulence model. Fig. 2.46 depicts the unstructured hexahedral mesh with tip gap and O-grid around the aerofoils suitable for Enhanced Wall Functions ($y+ < 5$) which improve off-design flow prediction.

Fig. 2.46 presents the torque and pressure coefficients calculated utilising the 1D and 3D models compared with the experimental data. Both torque coefficient calculations have a good agreement, nonetheless the one-dimensional model slightly overpredicts inhalation ($\phi < 0$) torque while underpredicts exhalation ($\phi > 0$) torque. This difference is likely to be due to flow deviation which modifies the flow velocity triangles. Measured and high-fidelity calculate pressure coefficient show a very good agreement while

inviscid calculation exhibits a much lower pressure drop. Fig. 2.46 also depicts the degree of reaction for the radial turbine which becomes negative at high flow coefficients during exhalation ($\phi > 0$). This behaviour of the degree of reaction explains the poor turbine efficiency when operating as centrifugal. Negative degrees of reaction imply adverse pressure gradients for the boundary layers which will be prone to separation and high aerodynamic loss.

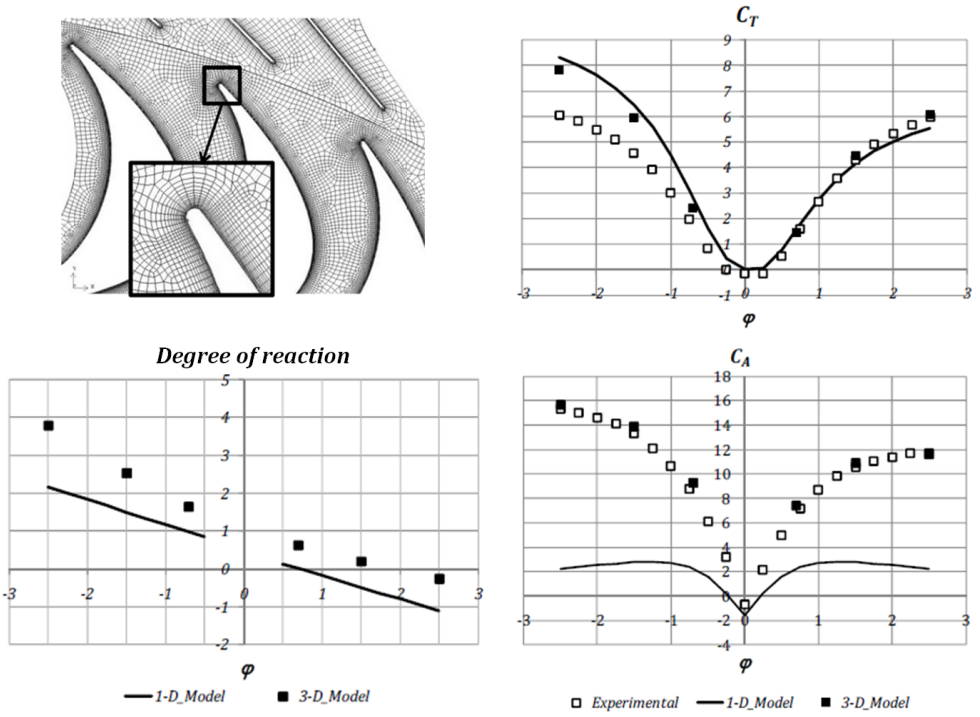

Fig. 2.46 Axial layer of computational grid and O-grid detail (top left), degree of reaction (bottom left), torque coefficient (top right), and pressure coefficient (bottom right) (Gonzalez et al., 2010)

Pereiras et al. (2011) carried out a thorough study on tip clearance effects on aerodynamic performance. It has been noted that tip leakage flows behaviour differs from inhalation to exhalation and increases flow deviation which has a knock on effect on downstream rows increasing incidence loss.

2.3.4 Note on Contra-Rotating Turbines

Contra-rotating turbines were firstly design for steam power generation applications. A radial contra-rotating centrifugal turbine was invented and designed by the Ljungström brothers in 1912 (see Fig. 2.48). Due to slow relative motion between parts and small thermal inertia, these turbines were employed in peak-load generators. Soon after axial contra-rotating turbines were built in the UK and the US for this type of application. Fig. 2.48 shows the Griffith contra-rotating axial flow high and low pressure turbine and compressor with bladed duct and turbine cooling proposed for jet engine applications (cf. Griffith, 1949).

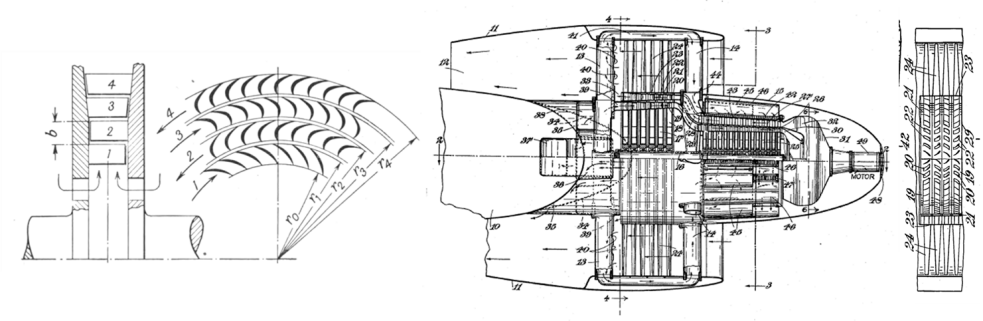

Fig. 2.47 Four row Ljungström turbine (left, Kearton, 1948), and Griffith contra-rotating engine (right, Griffith, 1949)

Early studies on contra-rotating studies were conducted by Wintucky and Stewart (1958). A two-stage contra-rotating turbine (stator-rotor-rotor) was compared to the equivalent conventional two-stage turbine (stator-rotor-stator-rotor). It was found that contra-rotating overall efficiencies were 2%-4% to that of equivalent conventional turbine depending on the blade loading due to the elimination of stator rows. Several shaft speed ratios were analysed showing no significant effect on the overall efficiency. Turbine efficiency steeply falls above certain exit swirl ($V_{u,exit}/\Delta V_{u,rotor2} > -0.3$). Therefore, controlling exit swirl angle plays a major role in turbine efficiency.

Two types of contra-rotating turbine stages were analysed by Louis (1985).

The first type is a two stage turbine composed of a stator-rotor and a rotor-only stage. Both types were found to be able to reach similar or higher loadings to those of conventional turbines. However, loading coefficient for the vaneless turbines are limited to four. The second kind is always vaneless which embodies two rotor-only stages. Several benefits of contra-rotating turbines were identified:

1. High specific power;
2. elimination of stator vanes which reduces efficiency penalties and weight;
3. moderate blade deflections;
4. removal of gyroscopic effects by torque balancing;
5. reduction of erosion rates due low speed of rotation; and
6. decrease of particulates deposition.

But then, various challenges arise:

1. Need for off-design speed control;
2. more acoustic modes are likely to propagate for two turbines with the same cut-off mode; and
3. complex rotor-to-rotor interaction phenomena.

Following the early application of contra-rotating steam turbines and the studies on gas turbines, this technology was shelved for some year until open rotor aeroengines reawakened the interest. A systematic basic analysis and taxonomy of contra-rotating turbines were performed by Cai et al. (1990). The key ideas exposed in this work are:

1. A turbine *stage* is defined as the *minimum number of blade rows which can roughly make the outlet kinetic condition similar to the inlet kinetic*

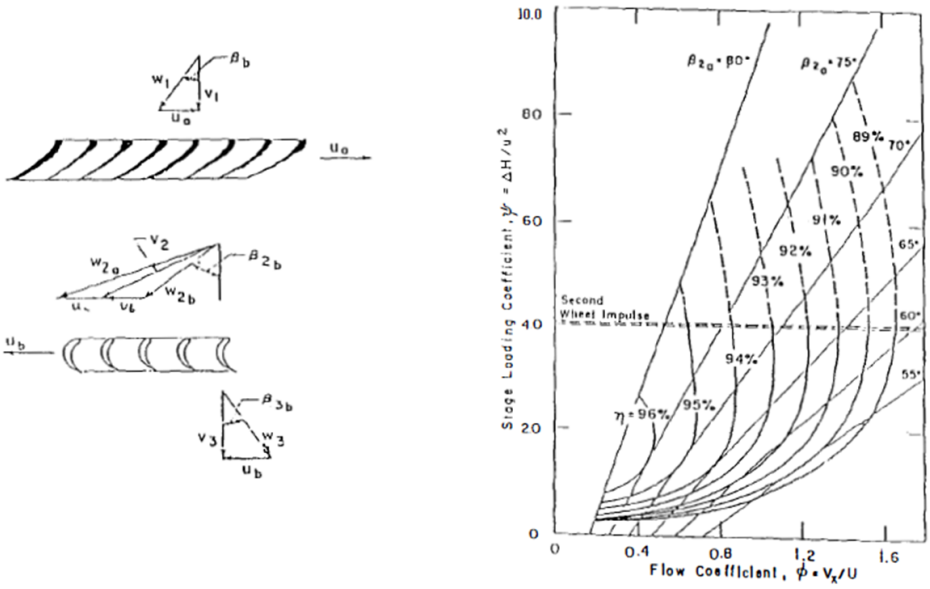

Fig. 2.48 Velocity triangles (left) and Smith chart (right) for a vaneless contra-rotating stage (Louis, 1985)

conditions. Hence, a conventional turbine stage is formed by a stator-rotor pair, a Curtis stage embodies four blade rows, and at least two rotors for contra-rotating turbine.

2. Each blade row is classified according to the velocity triangles:

   (a) Impulse (I): Inlet and outlet tangential components of the relative speed have the same magnitude and opposite directions ($w_{u,in} = w_{u,out}$). This type defines the practical lower limit for the degree of reaction.

   (b) Reaction (R): Inlet tangential component of the relative speed is null ($w_{u,in} = 0$).

   (c) Axial (A): Inlet or exit tangential component of the absolute speed is null ($v_u = 0$). This kind of cascade can be used without nozzle guide vanes at the expense of higher blade temperature. This kind

sets the practical upper limit for the degree of reaction.

(d) Duplicate (D): Exit condition is known as duplicate ($\alpha_{in} = \alpha_{out}$) which is typically utilised in multistage machines rather then the last stage.

3. Fig. 2.49 depicts the eleven contra-rotating turbine stages which are designated with three characters: (1) inlet condition of the first row, (2) inlet condition of the second row, and (3) exit condition. Stages AAA, AAD, IAA, RAA, and IID do not exist. AID and ARA are equivalent to AID and ARD.

4. Preliminary efficiency evaluation based on empirical correlations (including both profile and secondary loss) suggested that contra-rotating turbine stages have higher load capacity and efficiency when compared to conventional turbines (see Fig. 2.50).

Based on the study performed by Cai et al. (1990), there are two types of contra-rotating turbines which could be used in bi-directional flow: AIA ($\eta_{TS} \approx 0.83$) and ARA ($\eta_{TS} \approx 0.85$). However, it should be noted that although the velocity triangles could be reversed, leading and trailing edge should be carefully design as their functionality changes when the flow is reversed between the intake and the exhaust strokes of the water column. ARA turbines have the potential cost benefit of having identical blades.

Contra-rotating turbines have been also utilised in Renewable Energy Harvesting, other than the examples described in the previous sections for OWC power off-take. A few illustrative applications of successful design or implementation of contra-rotating turbines will be showcased in the forthcoming sections.

Tidal Energy

Rolls-Royce plc in partnership with Atkins Ltd have progressed the development of a bidirectional turbine and very-low head dual generation tidal

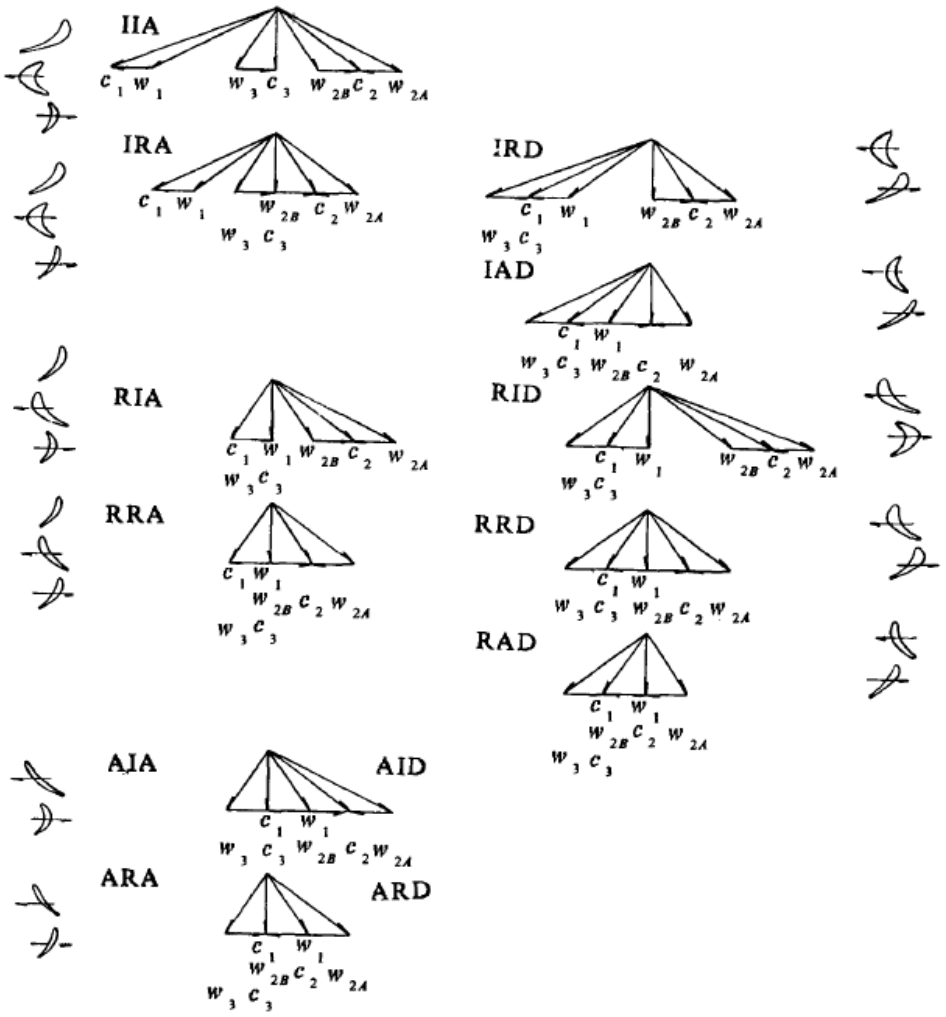

Fig. 2.49 Contra-rotating turbine stage cascade taxonomy (Cai et al., 1990)

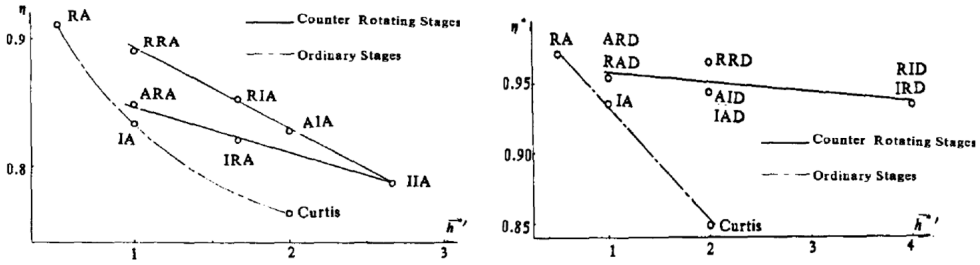

Fig. 2.50 Typical total-to-static peak-efficiency of contra-rotating turbines (left), and total-to-total peak efficiency of contra-rotating turbine stages (right) (Cai et al., 1990)

scheme proposed for construction and operation in the Severn estuary (Cardiff) to the outline design stage (see Rolls-Royce plc and Atkins ltd, 2010). Rolls-Royce has produced a very-low head variable-pitch contra-rotating turbine (see Fig. 2.51). Low tip speed and high blade spacing was achieved in order to reduced sea life mortality. Each rotor has been connected to an independent drive train. Blades can be rotated 180 degrees to align the leading edge to the flow direction. Three-dimensional unsteady viscous CFD simulations were used to validate and estimate turbine performance. CFD predictions showed that peak and off-design efficiencies exceeded 90%.

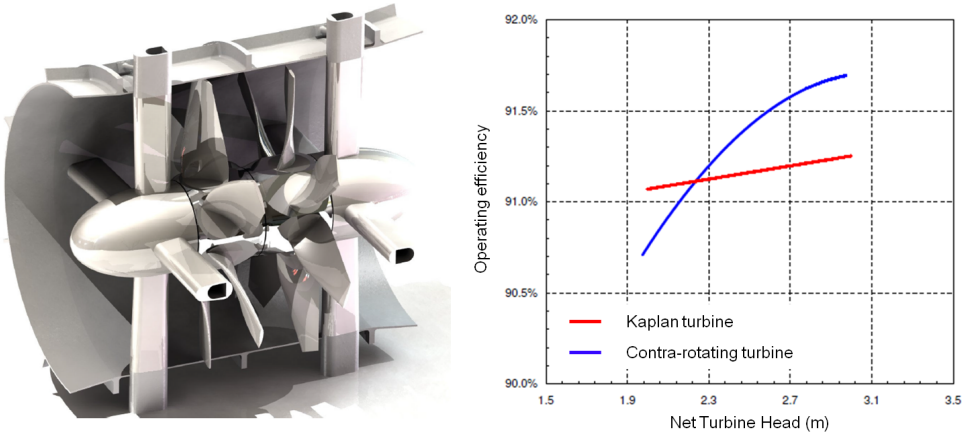

Fig. 2.51 Contra-rotating turbine configuration (left) and hydraulic efficiency predictions (right) (Rolls-Royce plc and Atkins ltd, 2010)

Hydroelectric Energy

A contra-rotating hydroelectric unit which comprises two runners which rotate in opposite directions has been proposed by Kasai et al. (2010). Fig. 2.53 depicts the such an arrangement. A contra-rotating electric generator has been introduced so that the gearbox can be eliminated. This unit could be used in small, mini, or micro hydropower, tidal or even pump storage units (Murakami et al., 2012). Two different runners were designed, validated by CFD, and then rig tested. Impeller A was designed based on NACA aerofoil profiles to operate in turbine mode. Impeller B was engineered to operate as pump by 3D inverse design techniques leading to higher solidities to reduce flow separation and outflow deviation. Fig. 2.53 presents the predicted and measured hydraulic efficiency in both turbine and pump modes. Efficiency values were achieved in excess of 80% in turbine mode and circa 80% when the unit operates as a pump.

Wind Energy

Trial testing of a contra-rotating wind turbine was performed by Ushiyama et al. (1996) demonstrating self-starting characteristics and increase relative rotational speed. In the past two decades, extensive investigation on contra-rotating wind turbines has been carried out. Jung et al. (2005) predicted the performance of a 30 kW contra-rotating wind turbine which comprised a primary rotor and an auxiliary rotor. The relative size of the rotors and the axial location was assessed utilising the strip theory plus experimentally-obtained wake data. Predicted results, which were validated by full-scale testing, showed an increase circa 10% in power generation (for the optimal axial distance between rotors) relative to the equivalent single rotor wind turbine. Both rotors were connected by a bevel gear mechanism and a planetary gear due to the dissimilar rotational speeds. Kanemoto and Galal (2006) proposed a contra-rotating wind turbine driving a double-armature generator. The large front rotor and the smaller rear rotor drive the inner and the outer armature

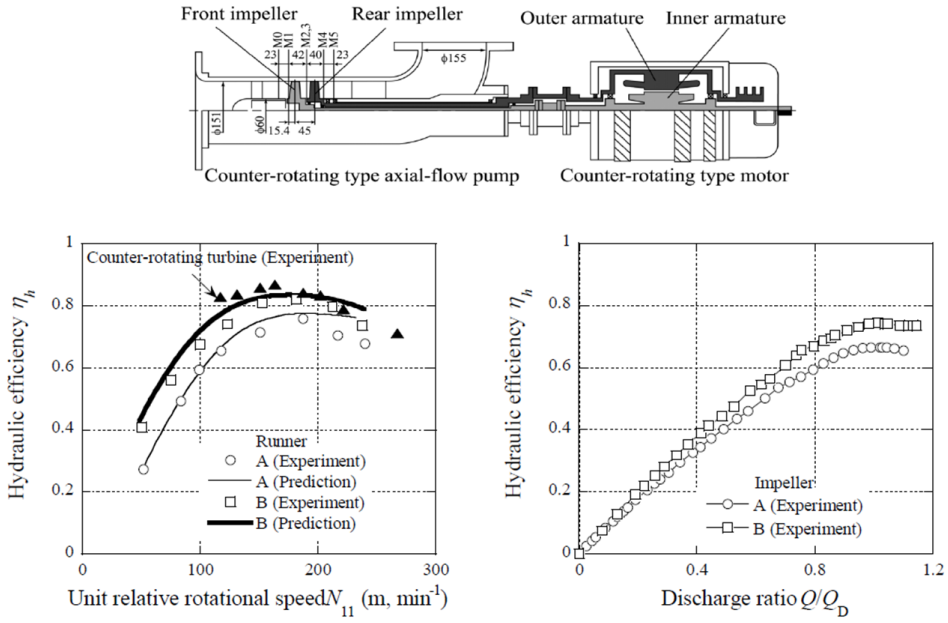

Fig. 2.52 Contra-rotating turbine-pump unit cross-section view (top), and hydraulic efficiency in turbine mode (bottom left) and pump mode (bottom right) (Murakami et al., 2013)

of the electric generator respectively. Such a configuration enables to generate more power than a conventional single-rotor wind turbine. Additionally, this novel architecture can output a constant power without the need for variable-pitch mechanism or a brake which greatly simplifies the mechanical construction.

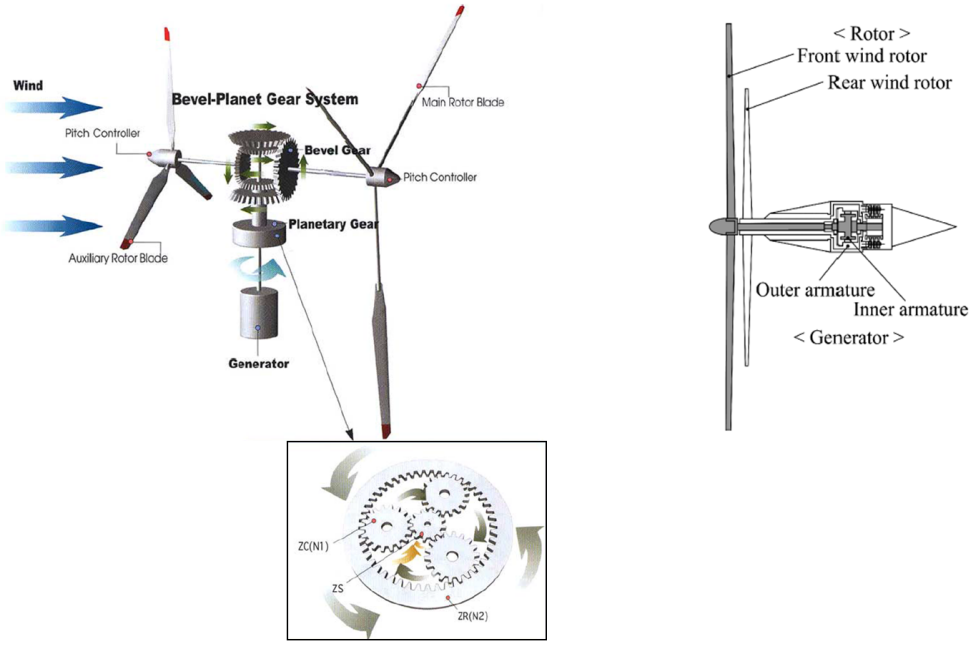

Fig. 2.53 Schematic of a contra-rotating wind turbine connected through a bevel gear (left) (Jung et al., 2005) and driving a double-armature electric generator (right) (Kanemoto and Galal, 2006)

Solar Energy

Solar updraft power plants or solar chimneys are thermal solar power plants which generate a convective flow due to surface heating which can be used to power a turbine (see .fig:CRTSolar). Theory, and results from designing, building, and operation of a demonstrator solar chimney in Spain are presented in Schlaich et al. (2005).

Denantes and Bilgen (2006) compared overall efficiencies, on- and off-design, for this type of power plants for a single rotor, a contra-rotating turbine with inlet guide vanes, and a vaneless contra-rotating turbine. Contra-rotating turbines showed much higher efficiency at part load conditions than the conventional turbine.

Preliminary design optimisastion studies were carried out by Fluri and Von Backström (2008) in which for turbines were analysed: (1) Single Rotor (SR) without Inlet Guide Vanes (IGVs), (2) Single Rotor (SR) with Inlet Guide Vanes (IGVs), (3) Contra-Rotating (CR) rotors without Inlet Guide Vanes (IGVs), and (4) Contra-Rotating (CR) rotors with Inlet Guide Vanes (IGVs). Rotor-only turbine was shown to waste a vast amount of energy as exhaust kinetic energy. Among the remaining architectures, contra-rotating turbines demonstrated higher efficiency, especially at low speeds of rotation (see Fig. **??**).

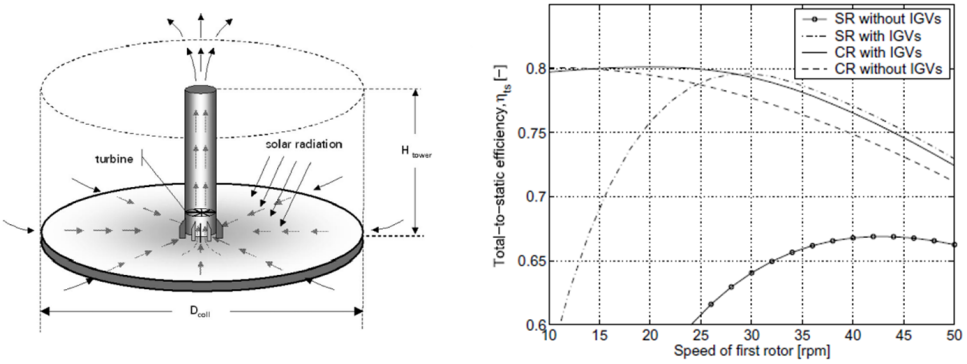

Fig. 2.54 Solar updraft power plant principle of operation (left, Schlaich et al., 2005), and total-to-static efficiency prediction for various turbine configurations (right, Fluri and Von Backström, 2008)

2.4 Electric Generators

The aim of this section is to provide a brief overview of the available technologies which could be implemented in a Electric generator sub-systems are largely a derivative from wind energy applications which have greater maturity than wave energy devices. The purpose of this section is to give a brief overview on the available electric generator technology and solutions in OWC power plants.

In the last years, variable speed systems have become more popular due to the greater flexibility and as they enable larger energy production. These variable speed electric generator are (cf. Bang et al., 2008; Muyeen et al., 2009):

1. *Doubly-Fed Induction Generator* (DFIG): This is the most widely spread solution in variable speed systems. The DFIG is essentially a wound rotor machine in which both rotor and stator are connected to the electric grid. It has the facility of controlling frequency and voltage output despite the rotor speed by means of power electronics. The main advantages are low cost, small size, and low weight.

2. *Permanent Magnet Synchronous Generator* (PMSG): This is the most effective electrical generator in terms of energy yield, reliability, and low maintenance because of the permanently magnetic rotor. The main drawbacks of this systems are higher cost, lower maturity, difficult start-up, need for a cooling system to keep the magnetic properties, and large size and weight (100 tonnes 6MW-PMSG compared to 10 tonnes of a 6MW-DFIG (power conversion, 2014))

3. *Wound Rotor Synchronous Generator* (WRSG): Similar to the PMSG but less efficient in terms of energy yield, more expensive, and heavier than the PMSG. The other drawback is the difficulty to find rate power <1MW which does not allow the OWC array configuration.

4. *Contra-Rotating Electric Generator*: Booker et al. (2010) proposed a permanent magnet contra-rotating topology which nearly doubles conventional generator power capability for a given rotor speed, low starting torque, and very high electrical and mechanical efficiencies. The manufacturing and assembly is simple and inexpensive. The full-size machines are will be in the 10kW to 20 kW rated power range. However, it requires a contra-rotating turbine to drive it and it is not yet a commercially available solution.

Early OWC power plants were based on conventional induction generators (wound rotor or squirrel cage rotor). Although these generators allow some variation in speed, typically 3%, these values have been deemed insufficient. Another important limitation of the conventional induction generators is that they consume reactive power, so these parameter needs to be compensated.

Recently constructed OWC power plants benefit from wind energy maturity, and therefore implement DFIGs. These generators enable variable speed operation at low cost and adequate power rating. PMSGs have too many challenges as described above, and WRSGs are only available for larger power ratings to those required by OWC power plants.

Therefore the focus in this work is on DFIG. This machine type has been widely studied, particulary linked to wind power generation systems (CITE). Amundarain et al. (2011) presented a OWC-specific application of a DFIG. Simulation of the electric machine and the control were the subjects of study. Two control methods were proposed and studied to control the rotor speed. The aim was to mitigate the stall problems of the Wells turbine which would increase power output.

Chapter 3

Nonlinear Stochastic Model for Water Column Forced Oscillations: Development and Validation

3.1 Introduction

The objectives of the work presented in this chapter are:

1. To develop a reduced-order model which contains the relevant physics of forced water column oscillations
2. To verify and validate the proposed model
3. To derive a parametric model for the dynamic model coefficients: added mass, radiation damping, and hydrodynamic restoration

The model characteristics are the following:

(1) Parametric (semi-physical)

(2) Non-linear

(3) Asymmetric (The equations or parameters describing the exhalation and inhalation process are different.)

The reduced-order model is validated, and then, the model coefficients are calibrated using a two-dimensional uRANS VoF solver (ANSYS Fluent®). The *validation* provides evidence that the dynamical system describing the water oscillation is formally correct. The *calibration* compares the response from a higher-order and the reduced-order methods so that the parameters can be tuned and correlated with the design parameters.

A system model can be built using three different approaches:

(1) *Physical* models which require a complete knowledge about the system physics translated into mathematical equations. This approach is normally unpractical for moderately complex systems.

(2) *Black-box* models are built weighing combinations of generic functions but cannot be interpreted. They are difficult to use for design, as there is no explicit link between the design parameters and the model output.

(3) *Semi-Physical* models combine the strengths of the two previous approaches. These models add physical understanding which provides the required information from the design perspective, while retaining certain flexibility by using empirical parameters in the derived equations. These parameters are unknown and need to be identified by optimisation techniques in the calibration process.

3.2 Development of a Nonlinear Stochastic Model for Water Column Forced Oscillations

3.2.1 Introduction

The reduced-order nonlinear model of water column oscillations is derived from the integral form of Mass and Momentum Conservation Laws. The integral approach provides numerical stability and simplicity, and also the facility to include parameters which can be easily adjusted using higher-fidelity simulations or experimental data.

These parameters to account for:

(1) friction loss (Chan and Baird, 1974);

(2) entry and exit loss (Knott and Flower, 1980; Knott and Mackley, 1980); and

(3) radiation damping and added-mass effects (Newman, 1977).

The resulting equations are a system of nonlinear Ordinary Differential Equations (ODEs) which are not linearised but solved using suitable numerical techniques. Non-linear effects, such as nonlinear radiation damping play a major role as shown in the following sections. The radiation damping is caused by kinetic energy loss at entry of water flow during exhalation and water outflow throughout inhalation. This phenomenon has been studied studied by Knott and Flower (1980).

The nonlinear reduced-order model presented in this chapter is based on the following assumptions:

(1) Deformable control volume (as shown in Fig. 3.1) for which the boundaries are the caisson walls (S_{SW}), the free surface at the top (S_{FS}), and the bottom opening (S_{B});

(2) two-dimensional formulation of the problem in the $x-z$ plane;

(3) uniform pressure on the free surface p_{FS} inside the chamber;

(4) no interaction with the sea bed; and

(5) diffraction effects due to submerged structures is neglected.

The analysis of any oscillatory motion requires identifying the system modal parameters: mass, damping, and stiffness. It also encompasses the study of the equilibrium points, stability, free response, and forced response.

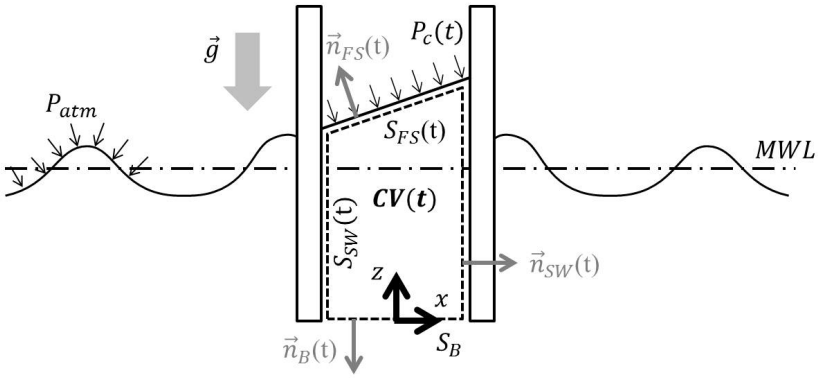

Fig. 3.1 Schematic of the control volume for OWC oscillation analysis

3.2.2 Conservation of Mass

Figure 3.1 presents the deformable control volume ($CV(t)$) and it boundary surfaces ($CS(t)$) used in the integral form of the Mass Conservation Equation (Eq. 3.1).

$$\frac{\mathrm{D}}{\mathrm{D}t}\int_{CV(t)}\rho_w\,\mathrm{d}V=\frac{\partial}{\partial t}\int_{CV(t)}\rho_w\,\mathrm{d}V+\int_{CS(t)}\rho_w(\vec{w}\cdot\vec{n})(t)\,\mathrm{d}S=0 \tag{3.1}$$

The only boundary of the control volume which allows material flux, i.e. $\vec{w}\cdot\vec{n}\neq 0$, is the bottom surface (S_B). Water is a liquid which for which compressibility can be neglected, therefore the water density is assumed uniform in the control volume $CV(t)$. Eq. 3.1 can be integrated as follows:

$$\rho_w\frac{\partial V_{CV}(t)}{\partial t}+\dot{m}_\mathrm{B}(t)=0 \tag{3.2}$$

being $\dot{m}_\mathrm{B}(t)$ the water mass-flow rate through the bottom openning

$$\dot{m}_\mathrm{B}(t)=\int_{S_\mathrm{B}}\rho_w(\vec{w}\cdot\vec{n})(t)\,\mathrm{d}S=\rho_w\langle w_\mathrm{B}\rangle S_\mathrm{B} \tag{3.3}$$

Eq. 3.2 can be rearranged as Eq. 3.4

$$\frac{\partial V_{CV}(t)}{\partial t}=-\frac{\dot{m}_\mathrm{B}(t)}{\rho_w} \tag{3.4}$$

Note that $\dot{m}_B$ is positive when water exits the control volume whereas negative when there is an incoming flow.

3.2.3 Conservation of Momentum

The Momentum Conservation Law is applied to the control volume $CV(t)$ shown in Fig. 3.1 to derive the Equation of Motion.

$$\begin{aligned}\frac{\mathrm{D}}{\mathrm{D}t}\int_{CV(t)}\rho_w\vec{v}(x,z,t)\,\mathrm{d}V &= \frac{\partial}{\partial t}\int_{CV(t)}\rho_w\vec{v}(x,z,t)\,\mathrm{d}V \\ &+ \int_{CS(t)}\rho_w\vec{v}(x,z,t)(\vec{w}\cdot\vec{n})(x,z,t)\,\mathrm{d}S \\ &= \int_{CV(t)}\rho_w\vec{g}\,\mathrm{d}V + \int_{CS(t)}(\overline{\overline{\tau}}\cdot\vec{n}_z)(x,z,t)\,\mathrm{d}S\end{aligned} \tag{3.5}$$

Gravitational oscillations are the subject of study, therefore (Eq. 3.5) has to be projected onto the direction of the gravitational acceleration vector (z in Fig. 3.1).

$$\begin{aligned}\frac{\mathrm{D}}{\mathrm{D}t}\int_{CV(t)}\rho_w v_z(x,z,t)\,\mathrm{d}V &= \frac{\partial}{\partial t}\int_{CV(t)}\rho_w v_z(x,z,t)\,\mathrm{d}V \\ &+ \int_{CS(t)}\rho_w v_z(x,z,t)(\vec{w}\cdot\vec{n})(x,z,t)\,\mathrm{d}S \\ &= \int_{CV(t)}\rho_w(-g)\,\mathrm{d}V + \int_{CS(t)}(\overline{\overline{\tau}}\cdot\vec{n})(x,z,t)\,\mathrm{d}S\end{aligned} \tag{3.6}$$

Solving Eq. 3.6 needs the knowledge of the velocity field $v_z(x,z,t)$. Most of the studies found in the literature (cf. Evans, 1982; Sarmento and Falcão, 1985) analytically derive a two-dimensional velocity field using Laplace's Equation and solving the boundary value problem.

An alternative approach is proposed in this work to solve Eq. 3.6. The velocity field $v_z(x,z,t)$ can be derived from the free-surface shape as described by Abramson (1966). The free-surface shape can be approximated by a sum of functions (Eq. 3.7) compatible with the boundary conditions. These functions are split into spatial and temporal terms (see Eq. 3.7).

$$z_{\mathrm{FS}}(x,z,t) = \sum_{j=0}^{\infty} \phi_j(x,z) q_j(t) \tag{3.7}$$

The spatial term $\phi_j(x,z)$ is the so-called *mode shape*, and the temporal function $q_j(t)$ is the *mode participation factor*. The exact approach requires computing the eigenfunctions, but the problem is simplified using a *collocation method* where the eigenfunctions (ϕ_j) are estimated by utilising *admissible functions* ($\widetilde{\phi}_j$).

This method has been successfully applied for mechanical vibrations (see Thomsen (2003)), but there is no known reference of the use of a collocation method for a similar application. For the purpose of this study, the infinite series can be truncated to only three terms as shown in Eq. 3.8: (1) mean water level, (2) rigid-body heave mode, and (3) rigid-body pitch mode.

$$\begin{aligned} z_{\mathrm{FS}}(x,z,t) \approx \sum_{j=0}^{\infty} \widetilde{\phi}_j(x,z) q_j(t) &= z_0 + \eta(t) + x \tan\vartheta(t) \\ &= z_0 + \eta(t) + x\psi(t) \end{aligned} \tag{3.8}$$

Therefore, free surface motion can be expressed as a combination of two oscillation modes:

(1) Heave mode (h): The free surface elevation of the water column is constant across the whole section. The useful compression work is produced by this mode.

$$z_{\mathrm{FS},h}(x,z,t) = \eta(t) \tag{3.9}$$

where $\widetilde{\phi}_h(x,z) = 1$, and $q_h(t) = \eta(t)$ $\Big(\eta(t) > z_0\Big)$

(2) Pitch mode (p): The free surface rotates about the centre axis of the column

$$z_{\mathrm{FS},p}(x,z,t) = x\tan\Big(\vartheta(t)\Big) = x\psi(t) \tag{3.10}$$

where $\widetilde{\phi}_p(x,z) = x$, and $q_p(t) = \psi(t)$ $\left(-\dfrac{\pi}{2} < \vartheta(t) < \dfrac{\pi}{2}\right)$

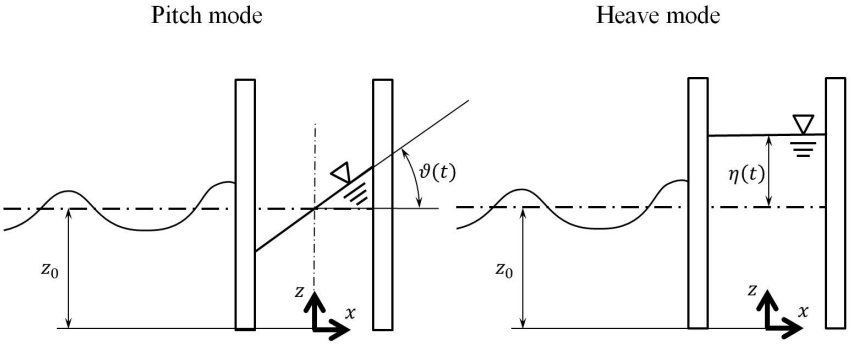

Fig. 3.2 OWC oscillation modes

The velocity field for each of the two modes can be derived from the free-surface shape as shown in Eq. 3.11 and Eq. 3.12.

$$v_{z,h}(x,z,t) = \frac{\partial}{\partial t}\Big\{z_{\mathrm{FS},h}(x,z,t)\Big\} = \dot{\eta}(t) \tag{3.11}$$

$$v_{z,p}(x,z,t) = \frac{\partial}{\partial t}\Big\{z_{\mathrm{FS},p}(x,z,t)\Big\} = x\dot{\psi}(t) \tag{3.12}$$

The velocity fields derived above can be substituted into in Eq. 3.6 which integration is described in the following sections. Then, both sides of the resulting equation are multiplied by the corresponding admissible shape ($\widetilde{\phi}_j$) to transform the system into modal coordinates . Observe that the two right-hand side terms in Eq. 3.13 are body and surface *generalised forces* respectively.

$$\begin{aligned}
&\frac{\partial}{\partial t}\int_{CV(t)} \rho_w \widetilde{\phi}_j^2(x,z)\dot{q}_j(t)\,\mathrm{d}V \\
&+\int_{CS(t)} \rho_w \widetilde{\phi}_j^2(x,z)\dot{q}_j(t)(\vec{w}\cdot\vec{n})(x,z,t)\,\mathrm{d}S \\
&=\int_{CV(t)} \rho_w \widetilde{\phi}_j(x,z)(-g)\,\mathrm{d}V \\
&+\int_{CS(t)} \widetilde{\phi}_j(x,z)(\overline{\overline{\tau}}\cdot\vec{n})(x,z,t)\,\mathrm{d}S
\end{aligned} \tag{3.13}$$

Eq. 3.13 is integrated under the following hypothesis are: (1) uniform water properties in the control volume, and (2) the free surface can only vary in a constant area cross-section (S_w). Note that local changes at the column bottom surface (S_B) are possible allowed. Hence, the velocity field can be locally altered at the bottom opening which can be determined using the Mass Conservation Law (Eq. 3.4).

If *heave* oscillations are considered, then

$$\begin{aligned}
\frac{\partial V_{CV}(t)}{\partial t} = S_w \frac{\partial z(t)}{\partial t} = S_w \dot{\eta}(t) = -S_\mathrm{B} w_{\mathrm{B},h}(t) \\
\implies w_{\mathrm{B},h}(t) = -\frac{S_w}{S_\mathrm{B}}\dot{\eta}(t)
\end{aligned} \tag{3.14}$$

and for the *pitch* mode

$$\frac{\partial V_{CV}(t)}{\partial t} = -\frac{\dot{m}_{\mathrm{B},p}(t)}{\rho_w} = 0 \quad \therefore \quad \dot{m}_{\mathrm{B},p}(t) = 0 \tag{3.15}$$

The following sections present the integration of each of the terms in

Eq. 3.13: (1) Material Derivative, (2) Generalised Body Forces, and (3) Generalised Surface Forces.

(1) Material Derivative

The material derivative describes the rate of change of momentum in the time-varying control volume. The first term is the so-called *local derivative* or *unsteady* term, and the second is the *convective derivative* or *advection* term.

First, the local derivative is calculated for the heave mode (Eq. 3.16).

$$\begin{aligned}\frac{\partial}{\partial t}\int_{CV(t)}\rho_w v_{z,h}(x,z,t)\,\mathrm{d}V &= \frac{\partial}{\partial t}\int_{CV(t)}\rho_w\widetilde{\phi}_h^2(x,z)\,\dot{q}_h(t)\,\mathrm{d}V\\ &\approx \rho_w S_w\frac{\partial}{\partial t}\int_0^{z_0+\eta(t)}\dot{\eta}(t)\,\mathrm{d}z\\ &= \rho_w S_w\frac{\partial}{\partial t}\Big\{[z_0+\eta(t)]\dot{\eta}(t)\Big\}\\ &= \rho_w S_w\Big\{[z_0+\eta(t)]\ddot{\eta}(t)+\dot{\eta}^2(t)\Big\}\end{aligned} \tag{3.16}$$

And then, the advection term (Eq. 3.17).

$$\begin{aligned}&\int_{CS(t)}\rho_w v_{z,h}(x,z,t)(\vec{w}\cdot\vec{n})(x,z,t)\,\mathrm{d}S\\ &=\int_{CS(t)}\rho_w\widetilde{\phi}_h^2(x,z)\dot{q}_h(t)(\vec{w}\cdot\vec{n})(x,z,t)\,\mathrm{d}S\\ &=\rho_w\int_{S_\mathrm{B}}\dot{\eta}(t)(\vec{w}\cdot\vec{n})(t)\,\mathrm{d}S\\ &=\rho_w S_\mathrm{B}\Big(\pm|\dot{\eta}(t)|\Big)\Big(\mp|w_B(t)|\Big)\\ &=\rho_w S_\mathrm{B}\left(\pm|\dot{\eta}(t)|\right)\left(\mp|\frac{S_w}{S_\mathrm{B}}\dot{\eta}(t)|\right)\\ &=-\rho_w S_w\dot{\eta}^2(t)\end{aligned} \tag{3.17}$$

The material derivative can calculated for *heave* oscillations adding both

terms calculated above (Eq. 3.18).

$$\begin{aligned}
&\frac{\mathrm{D}}{\mathrm{D}t}\int_{CV(t)}\rho_w v_{z,h}(x,z,t)\,\mathrm{d}V \\
&=\rho_w S_w\Big\{[z_0+\eta(t)]\ddot{\eta}(t)+\dot{\eta}^2(t)\Big\} \\
&-\rho_w S_w\dot{\eta}^2(t) \\
&=\Big\{\rho_w S_w[z_0+\eta(t)]\Big\}\ddot{\eta}(t)
\end{aligned} \tag{3.18}$$

The material derivative for *pitch* oscillations is presented in Eq. 3.21 together with the local derivative (Eq. 3.19) and the advection term (Eq. 3.20).

$$\begin{aligned}
\frac{\partial}{\partial t}\int_{CV(t)}\rho_w v_{z,p}(x,z,t)\,\mathrm{d}V &= \frac{\partial}{\partial t}\int_{CV(t)}\rho_w\widetilde{\phi}_s^2(x,p)\dot{q}_p(t)\,\mathrm{d}V \\
&=\rho_w\frac{\partial}{\partial t}\int_{-\frac{S_w}{2}}^{\frac{S_w}{2}}\int_0^{z_0+x\psi(t)}x^2\dot{\psi}(t)\,\mathrm{d}z\,\mathrm{d}x \\
&=\rho_w\frac{\partial}{\partial t}\left\{\frac{S_w^3 z_0}{12}\dot{\psi}(t)\right\}=\frac{1}{12}\rho_w S_w^3 z_0\ddot{\psi}(t)
\end{aligned} \tag{3.19}$$

$$\begin{aligned}
&\int_{CS(t)}\rho_w v_{z,p}(x,z,t)(\vec{w}\cdot\vec{n})(x,z,t)\,\mathrm{d}S \\
&=\int_{CS(t)}\rho_w\widetilde{\phi}_p^2(x,z)\dot{q}_p(t)(\vec{w}\cdot\vec{n})(x,z,t)\,\mathrm{d}S \\
&=0\quad\because\quad \dot{m}_{\mathrm{B},p}(t)=\int_{S_\mathrm{B}}\rho_w(\vec{w}\cdot\vec{n})(t)\,\mathrm{d}S\equiv 0
\end{aligned} \tag{3.20}$$

$$\frac{\mathrm{D}}{\mathrm{D}t}\int_{CV(t)}\rho_w v_{z,p}(x,z,t)\,\mathrm{d}V=\frac{1}{12}\rho_w S_w^3 z_0\ddot{\psi}(t) \tag{3.21}$$

(2) Generalised Body Forces

The only body force acting on the volume is the gravity for which the generalised force can be calculated using Eq. 3.22 for the *heave* mode and Eq. 3.23 for the *pitch* mode.

$$\begin{aligned}\int_{CV(t)} \rho_w \widetilde{\phi}_h(x,z)(-g)\,\mathrm{d}V &\approx -\int_{-\frac{S_w}{2}}^{\frac{S_w}{2}} \int_0^{z_0+\eta(t)} \rho_w g\,\mathrm{d}z\,\mathrm{d}x \\ &= -\rho_w g S_w \Big[z_0+\eta(t)\Big]\end{aligned} \tag{3.22}$$

$$\begin{aligned}\int_{CV(t)} \rho_w \widetilde{\phi}_p(x,z)(-g)\,\mathrm{d}V &\approx -\int_{-\frac{S_w}{2}}^{\frac{S_w}{2}} \int_0^{z_0+x\psi(t)} \rho_w x g\,\mathrm{d}z\,\mathrm{d}x \\ &= -\frac{1}{12}\rho_w g S_w^3 \psi(t)\end{aligned} \tag{3.23}$$

Note that the volume $V_{CV}(t)$ is an approximation if local variations of local cross sectional area in the vicinity of the bottom opening are allowed ($S_\mathrm{B} \approx S_w$).

(3) Generalised Surface Forces

The surface forces need to be integrated over the whole boundary of the control volume: free surface ($S_{\mathrm{FS}(t)}$), bottom (S_B), and caisson wall ($S_{\mathrm{W}(t)}$).

$$\begin{aligned}\int_{CS(t)} \widetilde{\phi}_j(x,z)\,(\overline{\overline{\tau}}\cdot\vec{n}_z)(t)\,\mathrm{d}S &= \int_{S_{\mathrm{FS}}(t)} \widetilde{\phi}_j(x,z)\,(\overline{\overline{\tau}}\cdot\vec{n}_z)(t)\,\mathrm{d}S \\ &+ \int_{S_{\mathrm{SW}}(t)} \widetilde{\phi}_j(x,z)\,(\overline{\overline{\tau}}\cdot\vec{n}_z)(t)\,\mathrm{d}S \\ &+ \int_{S_\mathrm{B}} \widetilde{\phi}_j(x,z)\,(\overline{\overline{\tau}}\cdot\vec{n}_z)(t)\,\mathrm{d}S\end{aligned} \tag{3.24}$$

The surface force acting on the free surface (S_FS) is the air pressure in the

chamber which is assumed to be uniform. The pressure in the air chamber is determined by the turbine characteristics. Shear stress and surface tension are neglected on this boundary. Eq. 3.25 and Eq. 3.26 present the integration of the free surface pressure for the *heave* and the *pitch* modes respectively.

$$\begin{aligned}\int_{S_{\mathrm{FS}}(t)} \widetilde{\phi}_h(x,z)\,(\overline{\overline{\tau}}\cdot\vec{n}_z)(t)\,\mathrm{d}S &= \int_{\frac{-S_{\mathrm{FS}}}{2}}^{\frac{S_{\mathrm{FS}}}{2}} \Big[-P_{\mathrm{FS}}(t)\Big]\,\mathrm{d}x \\ &= -P_{\mathrm{FS}}(t)S_{\mathrm{FS}}\end{aligned} \tag{3.25}$$

$$\begin{aligned}\int_{S_{\mathrm{FS}}(t)} \widetilde{\phi}_p(x,z)\,(\overline{\overline{\tau}}\cdot\vec{n}_z)(t)\,\mathrm{d}S &= \int_{\frac{-S_{\mathrm{FS}}}{2}}^{\frac{S_{\mathrm{FS}}}{2}} x\Big[-P_{\mathrm{FS}}(t)\Big]\cos(\vartheta(t))\,\mathrm{d}x \\ &= 0\end{aligned} \tag{3.26}$$

The surface force acting on the side caisson wall (S_{SW}) in the z-direction is the friction force, which is the shear stress (τ_w) effect due to the boundary layer on the wall. Note that the boundary layer profile is neglected in the velocity profile integrated in Eq. 3.6. Eq. 3.27 presents the shear stress on the caisson wall which is assumed to be proportional to the dynamic pressure. The proportionality constant is the so-called friction coefficient (K_{fr}) which is a function of the Reynolds number (Re).

$$\tau_w(t) = \mu_w \nabla\vec{v} = \frac{1}{2}K_{fr}\rho_w v_{z,\mathrm{SW}}^2(x,z,t) \tag{3.27}$$

$$\int_{S_{\mathrm{SW}}(t)} \widetilde{\phi}_j(x,z)\,(\overline{\overline{\tau}}\cdot\vec{n}_z)\,\mathrm{d}S = \int_{S_{SW}(t)} \widetilde{\phi}_j(x,z)\,\tau_w(t)\,\mathrm{d}S \tag{3.28}$$

Eq. 3.28 can be written as Eq. 3.29 for *heave* oscillations and as Eq. 3.30 for *pitch* oscillations.

$$\begin{aligned}\int_{S_{\mathrm{SW}}(t)} \widetilde{\phi}_j(x,z)\,\tau_w(t)\,\mathrm{d}S &= 2\int_0^{z_0+\eta(t)} -\frac{1}{2}K_{fr}\rho_w\dot{\eta}^2(t) \\ &= -K_{fr}\rho_w\Big[z_0+\eta(t)\Big]\,\dot{\eta}^2(t)\end{aligned} \tag{3.29}$$

$$\begin{aligned}&\int_{S_{SW}(t)} \widetilde{\phi}_j(x,z)\,\tau_w(t)\,\mathrm{d}S = \\ &\int_0^{z_0+\frac{S_w}{2}\psi(t)} \frac{S_w}{2}\Big[-\frac{1}{2}K_{fr}\rho_w\frac{S_w}{2}\dot{\psi}^2(t)\Big] \\ &+\int_0^{z_0-\frac{S_w}{2}\psi(t)} \Big(-\frac{S_w}{2}\Big)\Big[-\frac{1}{2}K_{fr}\rho_w\Big(-\frac{S_w}{2}\Big)\dot{\psi}(t)\Big] \\ &= -\frac{1}{8}K_{fr}S_w^2\rho_w\dot{\psi}^2(t)\end{aligned} \tag{3.30}$$

The surface forces acting on the bottom opening (S_{B}) of the water column are a combination of the hydrostatic $p_{H,B}$ pressure, the diffraction force caused by the dynamic pressure of the incident wave field $p_{e,B}$, the radiation force $p_{r,B}$ (cf. Newman, 1977), and a dynamic pressure contribution from vortex shedding $p_{v,B}$, (cf. Knott and Flower, 1980; Knott and Mackley, 1980). Some authors quote a small vortex effect based on theoretical results for small oscillations, but they can become significant at larger amplitudes as described by Faltinsen et al. (2007).

$$\begin{aligned}\int_{S_B} \widetilde{\phi}_j(x,z)(\overline{\overline{\tau}}\cdot\vec{n}_z)\,\mathrm{d}S = &\int_{S_B} \widetilde{\phi}_j(x,z)p_{H,B}\,\mathrm{d}S \\ &+ \int_{S_B} \widetilde{\phi}_j(x,z)p_{e,B}(x,z,t)\,\mathrm{d}S \\ &+ \int_{S_B} \widetilde{\phi}_j(x,z)p_{r,B}(x,z,t)\,\mathrm{d}S \\ &+ \int_{S_B} \widetilde{\phi}_j(x,z)p_{v,B}(t)\,\mathrm{d}S\end{aligned} \tag{3.31}$$

Eq. 3.32 and Eq. 3.33 present the generalised surface force due to hydrostatic pressure for *heave* oscillations and *pitch* oscillations respectively.

$$\begin{aligned}\int_{S_B} \widetilde{\phi}_h(x,z)p_{H,B}\,\mathrm{d}S &= \int_{-\frac{S_B}{2}}^{\frac{S_B}{2}} \left[\rho_w g z_0 + P_{\text{atm}}\right]\mathrm{d}S \\ &= \rho_w g z_0 S_B + P_{atm} S_B\end{aligned} \tag{3.32}$$

$$\int_{S_B} \widetilde{\phi}_p(x,z)p_{H,B}\,\mathrm{d}S = \int_{-\frac{S_B}{2}}^{\frac{S_B}{2}} x\left[\rho_w g z_0 + P_{\text{atm}}\right]\mathrm{d}S = 0 \tag{3.33}$$

Dynamic pressure variations are induced by incident waves. Sea waves are irregular which can be modelled as a stochastic excitation. Excitation pressure time series can be generated using the one-dimensional Jonswap spectrum proposed by Hasselmann et al. (1973). This spectral function describes the energy carried by each wave frequency. This irregular wave model is describe by the equations below:

$$E(f) = \alpha g^2 (2\pi)^{-4} f^{-5} \exp\left[-\frac{5}{4}\left(\frac{f}{f_m}\right)^{-4}\right] \gamma^{\exp\left\{\frac{-(f-f_m)^2}{2\sigma^2 f_m^2}\right\}}$$
$$\sigma = \begin{cases} \sigma_a \text{ if } f \leq f_m \\ \sigma_b \text{ if } f > f_m. \end{cases} \tag{3.34}$$

The participation coefficient for each wave frequency can computed inverse-Fourier transforming Eq. 3.34 as shown in Eq. 3.35.

$$C_{w,i} = \sqrt{2E(\omega_i)\Delta\omega_i} \tag{3.35}$$

The total excitation dynamic pressure can be calculated as superimposing individual contribution from each frequency from Eq. 3.35.

where wave phase is randomly selected according to $\beta_i \sim \mathscr{U}(-\pi, \pi]$, and the angular frequency and wave number are linked through the dispersion relationship: $\omega_i^2 = g\, k_i \tanh(k_i\, d)$.

Eq. 3.36 and Eq. 3.37 present the generalised surface force caused by the excitation pressure calculated above. The former describes *heave* oscillations, and the latter *pitch* oscillations.

$$\begin{aligned}
&\int_{S_\mathrm{B}} \widetilde{\phi}_h(x,z)\, p_{e,B}(x,z,t)\,\mathrm{d}S \\
&= \int_{-\frac{S_\mathrm{B}}{2}}^{\frac{S_\mathrm{B}}{2}} \sum_{i=1}^{N_w} \left\{ \rho_w\, g\, C_{w,i}\, \frac{\cosh[k_i(z+d)]}{\cosh(k_i d)} \cos(k_i x - \omega_i t + \beta_i) \right\} \mathrm{d}x \\
&= \sum_{i=1}^{N_w} 2\,\rho_w\, g\, C_{w,i}\, \frac{\cosh[k_i(z+d)]}{k_i \cosh(k_i d)} \sin\left(\frac{S_\mathrm{B}}{2} k_i\right) \cos(\omega_i t - \beta_i)
\end{aligned} \tag{3.36}$$

$$\begin{aligned}
&\int_{S_\mathrm{B}} \widetilde{\phi}_p(x,z)\, p_{e,B}(x,z,t)\,\mathrm{d}S = \\
&\int_{-\frac{S_\mathrm{B}}{2}}^{\frac{S_\mathrm{B}}{2}} (x) \sum_{i=1}^{N_w} \left\{ \rho_w g C_{w,i}\, \frac{\cosh[k_i(z+d)]}{\cosh(k_i d)} cos(k_i x - \omega_i t + \beta_i) \right\} \mathrm{d}x \\
&= \sum_{i=1}^{N_w} 2\,\rho_w\, g\, C_{w,i}\, \frac{\cosh[k_i(z+d)]}{k_i^2 \cosh(k_i d)} \left[2 \sin\left(\frac{S_\mathrm{B}}{2} k_i\right) \right. \\
&\left. - S_\mathrm{B}\, k_i \cos\left(\frac{S_\mathrm{B}}{2} k_i\right) \right] \sin(\omega_i t - \beta_i)
\end{aligned} \tag{3.37}$$

The generalised force due to radiation is formulated in following the definition given by Newman (1977), and then modified using the experimental work by Knott and Flower (1980). The radiation force is proportional to water column acceleration (added-mass effect), kinetic energy (radiation damping), and water elevation (hydrodynamic restoration or stiffness). Eq. 3.38 presents the radiation force for the *heave* mode, and Eq. 3.39 for *pitch* mode.

$$\int_{S_\mathrm{B}} \widetilde{\phi}_h(x,z)\, p_{r,\mathrm{B}}(x,z,t) = -M_{r,h}\ddot{\eta}(t) - B_{r,h}\dot{\eta}^2(t) - C_{r,h}\eta(t) \tag{3.38}$$

$$\int_{S_B} \widetilde{\phi}_p(x,z) p_{r,B}(x,z,t) = -M_{r,p}\ddot{\psi}(t) - B_{r,p}\dot{\psi}^2(t) - C_{r,s}\psi(t) \tag{3.39}$$

Depending on the opening geometry, vortices could appear. These flow structures induce loss which is proportional to the velocity squared for both *heave* (Eq. 3.40), and *pitch* mode (Eq. 3.41).

$$\int_{S_B} \widetilde{\phi}_h(x,z) p_{v,B}(x,z,t) = -K_{v,h}\dot{\eta}^2(t) \tag{3.40}$$

$$\int_{S_B} \widetilde{\phi}_p(x,z) p_{v,B}(x,z,t) = -K_{v,p}\dot{\psi}^2(t) \tag{3.41}$$

The integrated Equation of Motion for *heave* oscillations (see Eq. 3.42) in modal coordinates is obtained by combining Eqs. 3.18, 3.22, 3.25, 3.29, 3.36, 3.38, and 3.40.

$$\begin{aligned} &\left\{\rho_w S_w\Big[z_0+\eta(t)\Big] + M_{r,h}\right\}\ddot{\eta}(t) \\ &+\left\{K_{fr}\rho_w\Big[z_0+\eta(t)\Big] + B_{r,h} + K_{v,h}\right\}\dot{\eta}^2(t) \\ &+\left\{\rho_w S_w g + C_{r,h}\right\}\eta(t) \\ =&\sum_{i=1}^{N_w} 2\rho_w g C_{w,i}\frac{\cosh[k_i(z+d)]}{k_i\cosh(k_i d)}\sin\left(\frac{S_B}{2}k_i\right)\cos(\omega_i t-\beta_i) \\ &+\Big(P_{atm}-P_{FS}(t)\Big)S_w \end{aligned} \tag{3.42}$$

The integrated Equation of Motion for *pitch* oscillations (see Eq. 3.43) in modal coordinates is obtained from Eqs. 3.21, 3.23, 3.26, 3.30, 3.33, 3.37, 3.39, and 3.41.

$$\begin{aligned}
&\left\{\frac{1}{12}\rho_w S_w^3 z_0 + M_{r,p}\right\}\ddot{\psi}(t) \\
&+\left\{\frac{1}{8}K_{fr}S_w^2\rho_w + B_{r,p} + K_{v,p}\right\}\dot{\psi}^2(t) \\
&+\left\{\frac{1}{12}\rho_w g S_w^3 + C_{r,p}\right\}\psi(t) \\
=\sum_{i=1}^{N_w} 2\rho_w g C_{w,i}&\frac{\cosh[k_i(z+d)]}{k_i^2\cosh(k_i d)}\left[2\sin\left(\frac{S_\mathrm{B}}{2}k_i\right)\right. \\
&\left.-S_\mathrm{B}k_i\cos\left(\frac{S_\mathrm{B}}{2}k_i\right)\right]\sin(\omega_i t-\beta_i)
\end{aligned} \tag{3.43}$$

3.3 Validation of the Nonlinear Stochastic Model for Water Column Forced Oscillations

validation and calibration of the reduced-order nonlinear model against a higher fidelity method, two-dimensional multi-phase VoF RANS simulations, are presented in this section. An initial value problem is solved using both methods: (1) nonlinear reduced-order method described by Eq. 3.42, and (2) high-order VoF uRANS ANSYS Fluent®. the Volume-of-Fluid method (VoF) enables accurate definition of the free surface which is deemed as the most adequate multi-phase model for this problem.

The reduced-order model coefficients (M_r, B_r, C_r, K_v, and K_{fr}) can be adjusted by solving the optimisation problem described by Eq. 3.44. It is solved by an iterative prediction-error minimisation method based on the Newton-Raphson algorithm using Matlab®. These coefficients need to be related to

design parameters to allow for design optimisation.

$$\min\ E(t) = \sum_{i=1}^{N} \left[e(t_i)\right]^2 \tag{3.44}$$

where $e(t_i)$ is the error between the solutions calculated by ANSYS Fluent®and the reduced-order model for a given instant t_i, and N is the number of time samples.

An uniform initial elevation is applied to the water column inside the chamber (see 3.3), i.e. free-decay response of the the water column has been used to calibrate the coefficients in Eq. 3.42. No differential pressure between the air chamber and the atmosphere is applied. The free surface pressure or wave excitation pressure are not system properties, but an external forces as describe in the previous section. Therefore, there is no need to include them to identify the equation coefficients.

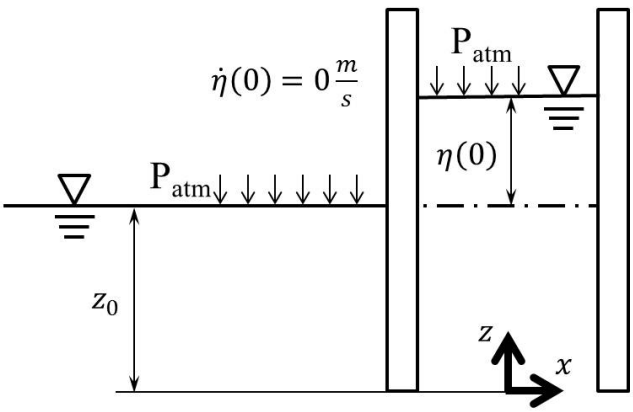

Fig. 3.3 Initial state for reduced-order model validation

An example CFD mesh employed in the ANSYS Fluent®simulations is

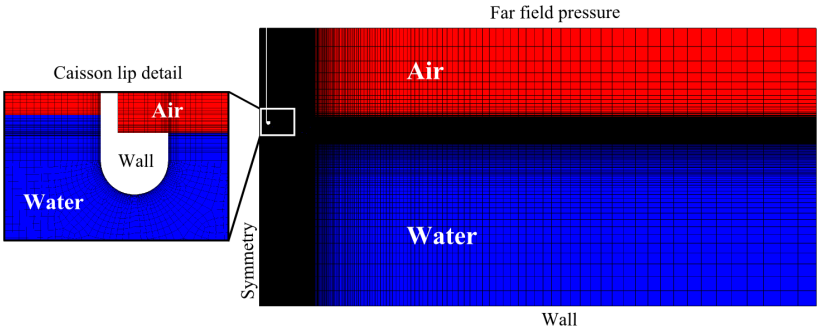

Fig. 3.4 Two-dimensional mesh for VoF validation and calibration of the low-order model (model #8 in Table 3.1)

shown in Fig. 3.4. The mesh is structured with boundary layer around the caisson wall and lip to resolve the boundary layer in viscous simulations. Both inviscid and viscous simulations have been performed. This mesh topology is maintained for all the cases in this study. There is also improved mesh resolution around means water level to improve free surface definition. Fig. 3.4 also shows the initial condition in terms of phase: air (red) and water (blue).

3.3.1 Geometry Definition and Design Parameters

Caisson geometry is parameterised as shown in Fig. 3.5. The nonlinear reduced-order coefficients must be related to the design parameters, so that the model output can be related to the physical geometry.

(1) Submergence depth (L_w): Distance between the mean water level and the bottom opening of the caisson.

(2) Lip radius (R_L): A rounded lip is added to the bottom opening to create a bell mouth. This radius greatly influences entry and exit kinetic energy loss, and vortex generation.

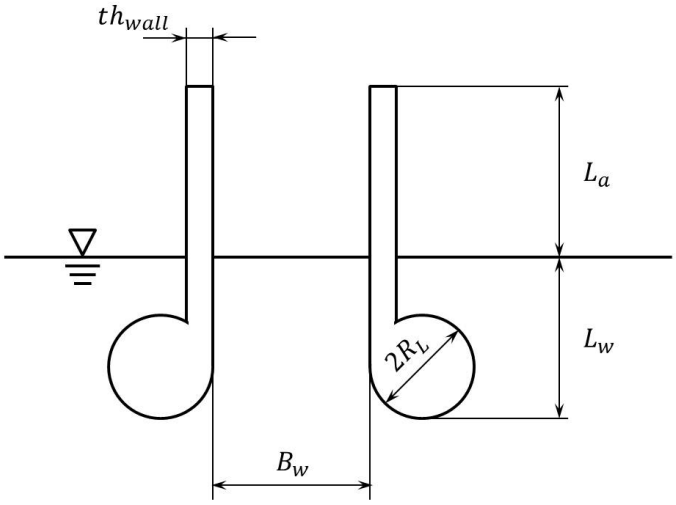

Fig. 3.5 Caisson design parameters

(3) Chamber breath (B_w): This magnitude is the free-surface area per unit width of collector.

(4) Air reservoir height (L_a): Distance between the mean water level and the top inside the caisson. The air plenum size needs to accommodate the maximum amplitude reached in the test case. This parameter plays a major role in the air compressibility effects.

(5) Concrete wall thickness (th_{wall}): The design of the wall thickness is likely to be determined by mechanical integrity requirements. This parameter is only included in this study to evaluate its possible influence on the water column oscillations.

The caisson design is defined by 4 parameters: L_w, R_L, B_w, and L_a. The wall thickness is included for exploration purposes only.

3.3.2 Design of Experiments

The coefficients of the nonlinear reduced-order model are calibrated using different caisson geometry designs (Fig. 3.5). Full factorial Design of Experiments (DoE) is used to sample the whole likely design space. The Optimised Latin Hypercube Sampling (OLHS) has been applied to generate 16 (2^4) different caisson designs which are presented in Table 3.1.

Table 3.1 Caisson models generated by *OLHS*

Model #	L_a [m]	L_w [m]	R_L [m]	th_{wall} [m]	B_w [m]
1	1.0	10.0	0.80	0.23	6.20
2	1.6	4.0	2.80	0.48	2.40
3	2.2	1.6	0.40	1.75	9.37
4	2.8	9.4	2.00	1.49	1.13
5	3.4	8.8	0.20	0.73	3.67
6	4.0	6.4	0.00	0.86	10.00
7	4.6	5.2	1.00	1.37	1.77
8	5.2	2.2	1.20	0.61	6.83
9	5.8	3.4	2.20	0.99	5.57
10	6.4	7.0	3.00	1.87	4.30
11	7.0	4.6	1.40	1.24	3.03
12	7.6	7.6	0.60	0.35	8.10
13	8.2	1.0	1.60	1.11	8.73
14	8.8	2.8	1.80	1.62	4.93
15	9.4	5.8	2.40	2.00	0.50
16	10.0	8.2	2.60	0.10	7.47

3.3.3 Reduced-Order Model Coefficients

A model for the reduced-order model coefficients (M_r, B_r, C_r, K_v, and K_{fr}) is presented in this section. It has been obtained solving the optimisation problem in Eq. 3.44.

The results from both high-order and reduced-order simulations are presented in Appendix A. Extensive research has been carried out by analysing 66 cases for a combination of:

(1) Initial conditions: Initial elevation of the water column of $0.33L_w$, $-0.33L_w$, and $0.66L_w$ to explore amplitude effects.

(2) Flow regimes: Three flow regimes are investigated inviscid, fully laminar, and fully turbulent (using the standard $k-\varepsilon$ turbulence model). Transitional flow is not included as the complexity of this flow regime is beyond the scope of this work.

The equation coefficients in Eq. 3.42 have been found to correlate with the design variables as follows:

(1) Added-mass coefficient ($\widetilde{M}_{r,h}$): Fig. 3.7 depicts the added-mass coefficient which represents a virtual increase of the mass of water of the water column. Eq. 3.45 presents the added-mass coefficient (added mass normalised by water density and cross-sectional area) has been found to correlate with the square root of the cross-sectional area, $\sqrt{S_w}$.

$$\widetilde{M}_{r,h} = \frac{M_{r,h}}{\rho_w S_w} = 2.6391\sqrt{S_w} - 1.4981 \quad [\text{m}] \tag{3.45}$$

(2) Nonlinear radiation damping coefficient ($\widetilde{B}_{r,h}$): Fig. 3.9 shows the nonlinear radiation coefficient correlation. This coefficient represents the kinetic energy loss by the water column. The loss coefficient has not been best-fitted, but an envelope is derived which represents the maximum loss of the water column. This coefficient has been found to

have different values during the exhaust stroke (see Eq. 3.47) and the intake stroke (Eq. 3.48). Vortex-shedding effects cannot be separated from the radiation effects, as both are a function of the water column velocity squared $\dot{\eta}^2(t)$.

$$\widetilde{B}_{r,h} = \frac{B_{r,h} + K_{v,h}}{\rho_w S_w} \tag{3.46}$$

$$\widetilde{B}^{+}_{r,h} = \widetilde{B}_{r,h}\Big|_{\dot{\eta}(t)\geq 0} = \left(\frac{R_L}{S_w}\sqrt{\frac{L_w}{g}} + 0.150\right)^{-2.5} + 0.7 \quad [1] \tag{3.47}$$

$$\widetilde{B}^{-}_{r,h} = \widetilde{B}_{r,h}\Big|_{\dot{\eta}(t)<0} = \left(\frac{R_L}{S_w}\sqrt{\frac{L_w}{g}} + 0.025\right)^{-2.0} - 0.3 \quad [1] \tag{3.48}$$

Boundary layer separation in oscillatory flow depends on the Keulegan-Carpenter number (Eq. 3.49) which is defined as the amplitude-to-lip radius ratio. No vortex detachment is observed if $K_C < 4$.

$$K_C = \frac{\eta_{\max}}{R_L} < 4 \quad \Longrightarrow \quad \text{no vortex} \tag{3.49}$$

Water column amplitude can vary depending on the amplitude and frequency of the incoming waves. Therefore, al alternative parameter has been derived as the ratio of lip radius (normalised by chamber

breath) and water column heave-mode natural frequency. Note that for harmonic motion $\eta_{\max} = \omega\,\dot{\eta}_{\max}$, therefore $\dot{\eta}^2_{\max} = \eta_{\max}\dot{\eta}_{\max}/\omega$. Fig. 3.6 shows the vortex formation and evolution for the inviscid test case model #6. Wave radiation is shown to be linked to the vortex sheeding process seen as a travelling wave generated.

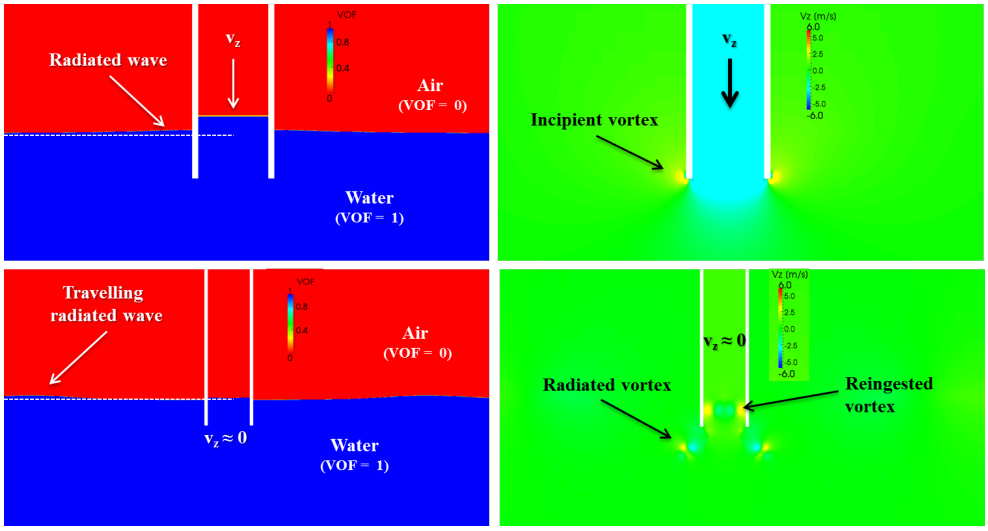

Fig. 3.6 Volume of Fluid (left) and vertical velocity v_z (right) contours showing the vortex formation during free decay of the water column at two instants: maximum speed (top) and zero elevation (bottom)

(3) Radiation restoration coefficient ($\widetilde{C}_{r,h}$): Fig. 3.10 depicts the radiation restoration which is the proportionality constant between the hydrodynamic force and the water column elevation (hydrodynamic stiffness). This parameter has been observed to correlated with average radiated energy as shown in Eq. 3.50. This phenomenon can be seen as part of the exit kinetic energy loss at the chamber bottom opening being transformed into pressure.

$$\widetilde{C}_{r,h} = \frac{C_{r,h}}{S_w} = 0.0416 \left[\frac{1}{2}\left(\widetilde{B}^{+}_{r,h} + \widetilde{B}^{-}_{r,h}\right)\right]^2 + 0.4787 \left[\frac{1}{2}\left(\widetilde{B}^{+}_{r,h} + \widetilde{B}^{-}_{r,h}\right)\right] \quad \left[\frac{\text{kg}}{\text{m}^2\text{s}^2}\right] \tag{3.50}$$

(4) Friction coefficient (K_{fr}): The friction effects have been found to be negligible compared to the nonlinear radiation damping when comparing inviscid, and viscous uRANS simulations, both laminar and turbulent. This result is based on the assumption of hydraulically smooth walls which might need to be reassessed depending on the caisson wall roughness characteristics.

$$K_{fr} \approx 0 \tag{3.51}$$

3.4 Analysis and Solution of the Nonlinear Stochastic Model

3.4.1 Free Response

(1) Dynamical System

The proposed model in the previous sections is analysed in the framework of Dynamical Systems Theory. This approach provides the required toolset to identify the equilibrium points, stability, and the behaviour of nonlinear state space equations.

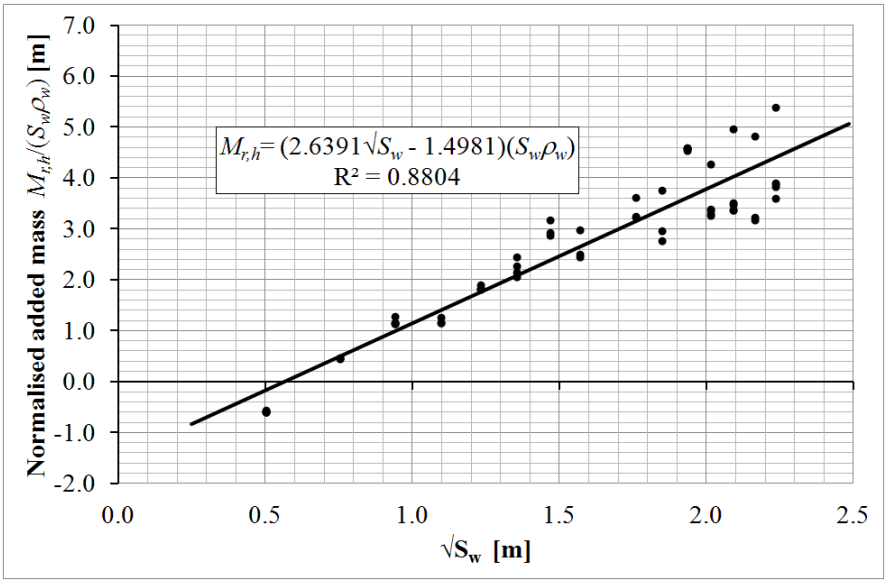

Fig. 3.7 Added mass-OWC cross sectional area correlation (heave mode)

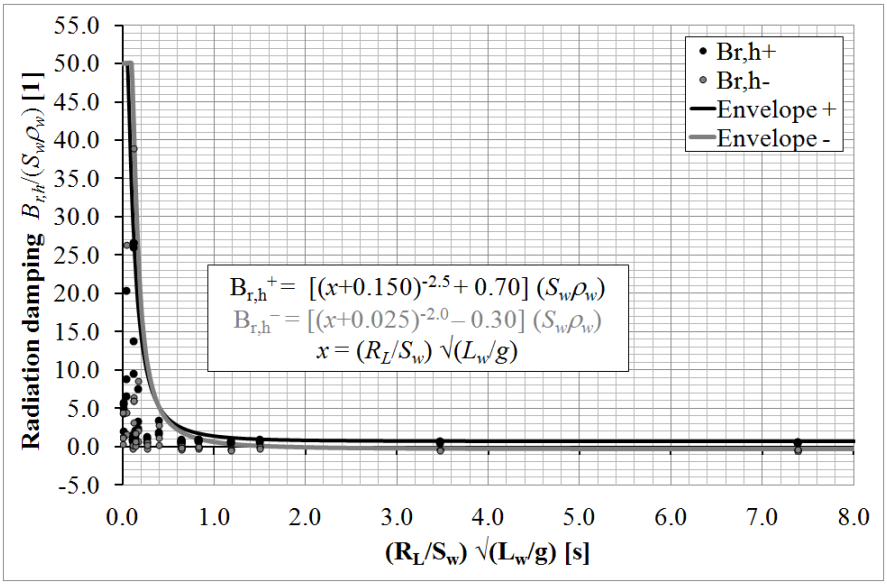

Fig. 3.8 Nonlinear radiation damping-OWC geometry correlation (heave mode)

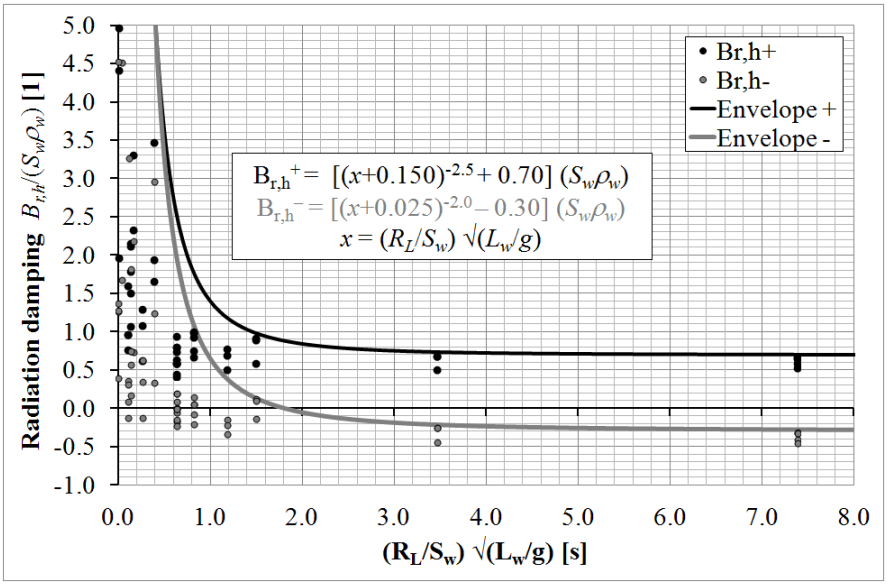

Fig. 3.9 Zoomed nonlinear radiation damping-OWC geometry correlation (heave mode)

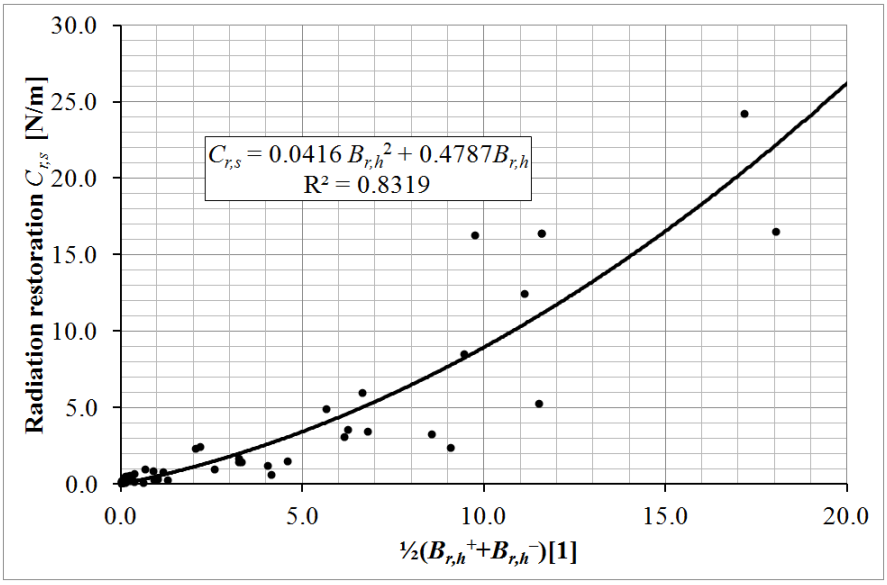

Fig. 3.10 Radiation restoration-nonlinear damping correlation (heave mode)

An Ordinary Differential Equation (ODE) can be transformed into a first order system of ODEs by changing the variables as shown in Eq. 3.52.

$$\begin{cases} z_1(t) = \eta(t) \\ z_2(t) = \dot{\eta}(t) \end{cases} \tag{3.52}$$

Eq. 3.42 can be recasted as first order system of ODEs (Eq. 3.53)

$$\begin{cases} \frac{\partial z_1(t)}{\partial t} &= f_1\Big(z_1(t), z_2(t)\Big) \\ \frac{\partial z_2(t)}{\partial t} &= f_2\Big(z_1(t), z_2(t)\Big) \end{cases} \tag{3.53}$$

where

$$f_1(z_1(t), z_2(t)) = \qquad\qquad z_2(t) \tag{3.54}$$

and

$$f_2(z_1(t), z_2(t)) = \tag{3.55}$$

$$\begin{cases} \frac{1}{z_1(t)+z_0+\widetilde{M}_{r,h}} \left[-\widetilde{B}^{+}_{r,h} z_2^2(t) - (g + \widetilde{C}_{h,r}\rho_w) z_1(t) \right] & \text{if } z_2(t) \geq 0 \\ \frac{1}{z_1(t)+z_0+\widetilde{M}_{r,h}} \left[+\widetilde{B}^{-}_{r,h} z_2^2(t) - (g + \widetilde{C}_{h,r}\rho_w) z_1(t) \right] & \text{if } z_2(t) < 0 \end{cases} \tag{3.56}$$

Eq. 3.53 presents an autonomous system as it does not explicitly contain time. Nonlinearity is introduced by radiation damping which is proportional to the free-surface velocity squared.

(2) Stability

The Jacobian matrix (J_f) allows to study local stability of nonlinear systems of ODEs in the vicinity of a fixed point (cf. Thomsen, 2003). The *Hartman–Grobman Theorem* states that the nonlinear system $z_i' = f_i(z_i)$ is locally homeomorphic to the linear system $z_i' = J_f(z_i)$ in the vicinity of a hyperbolic fixed point, i.e. a fixed point for which the real part of the eigenvalues of the Jacobian are non-zero. The finding the homeomorphism for Hartman-Grobman theorem can be difficult. However, the practical implication is that both nonlinear and linearised systems have the same behaviour in the vicinity of an equilibrium point.

For other cases in which the real part of the eigenvalues of the Jacobian is zero, the *Poincaré-Bendixon theorem* is applied. An important consequence of the application of this theorem to Eq. 3.53 is that no strange attractors can exist in two dimension, and therefore, chaotic behaviour is not possible.

The *fixed* or *equilibrium points* $\{z_{10}, z_{20}\}$ of Eq. 3.53 can be found by solving the state equations $\{f_1(t) = 0,\, f_2(t) = 0\}$.

The equilibrium point calculated in .eq:eqstate cannot exist as $\widetilde{C}_{h,r}$ is a strictly positive function as shown in Fig. 3.10. Water density ρ_w and gravity acceleration g are always positive real numbers. Therefore, the only possible **equilibrium point** of the system is $z_0 = \{z_{10}, z_{20}\} = \{0, 0\}$.

The jacobian of Eq. 3.53 is presented in Eq. 3.57. The independent variable (t) is omitted in the following equations for clarity: $z_1 = z_1(t)$, $z_2 = z_2(t)$.

$$J_f(z_1,z_2) = \begin{pmatrix} 0 & 1 \\ \dfrac{\widetilde{B}_{r,h} z_2^2 + g\, z_1 + \widetilde{C}_{h,r}\, \rho_w\, z_1}{(z_1 + z_0 + \widetilde{M}_{r,h})^2} - \dfrac{g + \widetilde{C}_{h,r}}{z_1 + z_0 + \widetilde{M}_{r,h}} & \pm \dfrac{2\widetilde{B}_{r,h} z_2}{z_1 + z_0 + \widetilde{M}_{r,h}} \end{pmatrix} \tag{3.57}$$

The jacobian is evaluated at the equilibrium state $\{z_{10}, z_{20}\}$ to calculate the eigenvalues which determine the type of equilibrium point.

$$J_{f0} = J_f(z_1,z_2)\Big|_{z_0} = \begin{pmatrix} 0 & 1 \\ -\dfrac{g + \widetilde{C}_{h,r}\, \rho_w}{z_0 + \widetilde{M}_{r,h}} & 0 \end{pmatrix} \quad \forall z_2 \tag{3.58}$$

Eq. {eq:eigval present the two eigenvalues ($\lambda_{1,2}$) of the linearised system are calculated in the neighbourhood of the equilibrium point:

$$\lambda_{1,2} = \pm \sqrt{-\frac{g + \rho_w \widetilde{C}_{h,r}}{z_0 + \widetilde{M}_{r,h}}} \quad \forall z_2 \tag{3.59}$$

The following conclusions can be deduced from the calculate eigenvalues above (Eq. 3.59).

(1) The stability of the nonlinear system cannot be determined from the linearised system properties in the neighbourhood of the fixed point. The real part of the eigenvalues of the linearise system is zero $\Re(\lambda_{1,2}) = 0$ (critically stable). Nonlinear stability of the system depends on higher order terms, and the Hartman-Gobman Theorem cannot be applied.

(2) The natural frequency can be calculated and it only depends on the water column geometry (L_w, S_w) and gravity acceleration as shown in

Eq. 3.60. However, this value will greatly differ from the resonant frequency if significant nonlinear radiation damping is present.

$$\begin{aligned}\omega_n &= \sqrt{\frac{g}{z_0 + \widetilde{M}_{r,h}}} \\ &= \sqrt{\frac{g}{z_0 + 2.6391\sqrt{S_w} - 1.4981}} \quad [\text{rad/s}]\end{aligned} \tag{3.60}$$

(3) Phase map

The solutions of Eq. 3.52 are presented in the so-called phase plane. The phase plane displays the two state variables, free-surface elevation ($z_1 = \eta$) and free-surface velocity ($z_2 = \dot{\eta}$), for a given initial state.

Fig. 3.11 depicts the orbits or trajectories for Eq. 3.52 for two different random sets of design variables (L_w, B_w, and R_L) for lightly damped (blue) and heavily damped (red) water column oscillations.

The phase map can be used to study the stability of a dynamical system. Both sets of orbits in Fig. 3.11 are stable as the states are attracted to the fixed point in $\{z_{10}, z_{20}\}$.

3.4.2 Forced response

The forced response of the water column oscillations is carried out by imposing a constant-amplitude sinusoidal excitation and performing a very slow frequency sweep (1^{-4}rad/s^2). For a typical caisson design, three different amplitudes are simulated for a given caisson design: datum, 1.5x datum, and 5.0x datum.

The time responses for these experiments are shown on Fig. 3.12 (datum), Fig. 3.13 (1.5x datum), and on Fig. 3.14 (5.0x datum).

Fig. 3.15 depicts the normalised response against frequency for the three

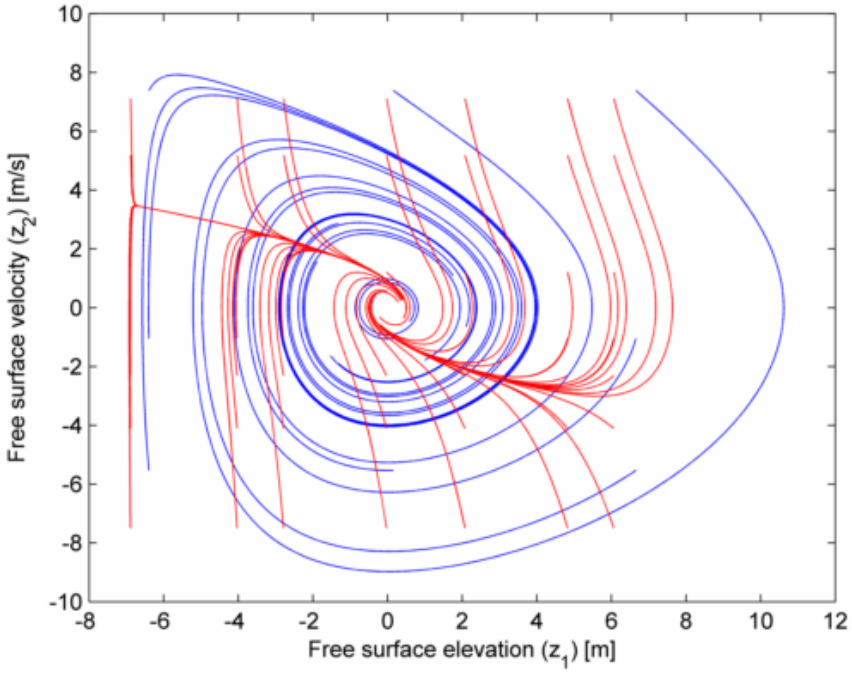

Fig. 3.11 Phase map of heaving water column oscillations: light damping (blue) and heavy damping (red)

cases described above. Changes in both amplitude and frequency are observed depending on the incoming wave amplitudes:

(1) The datum amplitude resonance is narrow which indicates very low damping. An amplification factor circa 30 (with respect to the zero frequency amplitude) is calculated.

(2) If the amplitude of the incoming wave increases by 50% (1.5x datum), the radiation damping lowers the peak response by a factor of 4.22. This significant reduction in amplitude at resonance shows the powerful effect of nonlinear radiation damping. The resonant frequency also increases by 20%..

(3) In the last case, the incoming wave amplitude greatly increases (5.0x datum) which results in a reduction of resonance peak by a factor of 10. The resonant frequency is increased respect to the datum case but it drops by 2% relative to the intermediate amplitude. Therefore, the reduction in the resonant frequency is caused by the radiation damping which overtakes the effect of the hydrodynamic restoration.

3.5 Mode Contamination: Slosh oscillations

Any contained liquid with a free surface can be excited in its own natural sloshing modes. The sloshing is induced by the motion of the walls. The OWC bottom opening can be seen as a virtual wall which is subject to the wave acceleration.

The water column slosh frequencies could match the heave-mode resonant frequency. The slosh modes would not produce any useful compression or expansion work as they are in standing waves. However, the energy carried by the sea waves is split between the heave motion and the slosh modes.

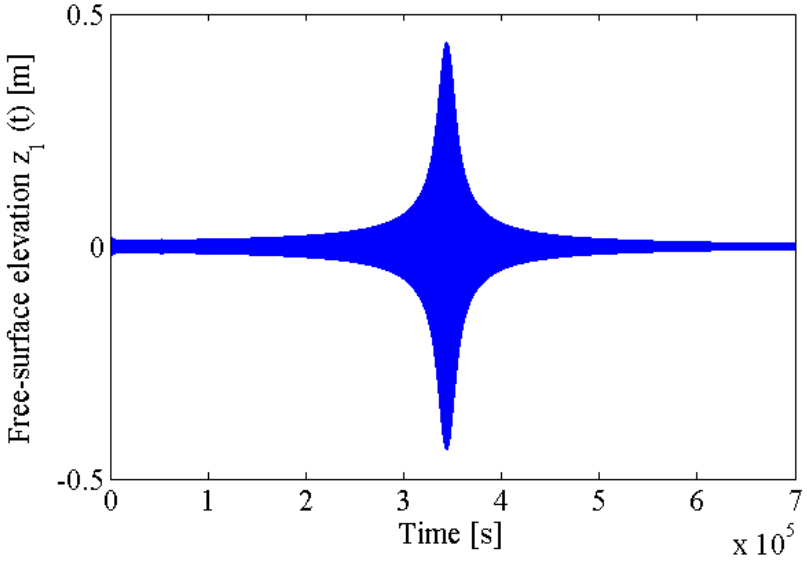

Fig. 3.12 Forced response datum amplitude time series

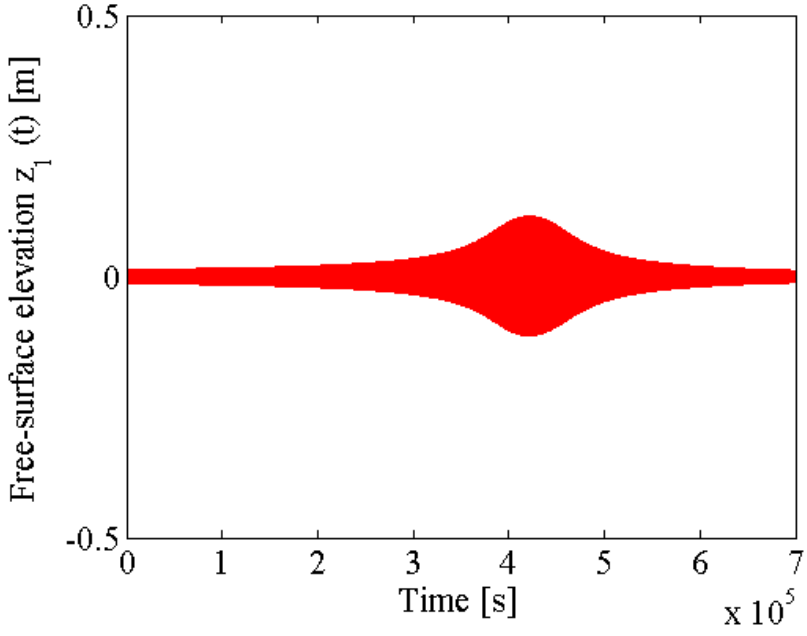

Fig. 3.13 Forced response 1.5x datum amplitude time series

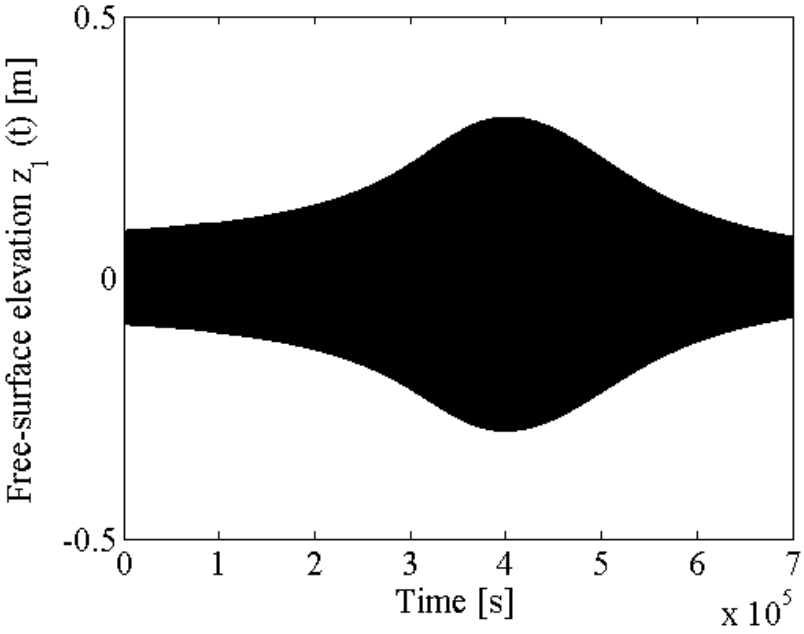

Fig. 3.14 Forced response 5x datum amplitude time series

Good caisson designs must ensure sufficient frequency separation between the slosh modes and the heave mode. O

The slosh-mode frequencies can be analytically derived from Laplace's Equation (Eq. 3.61)) if the fluid is assumed to be non-viscous, linear, and irrotational. Adequate boundary conditions must be imposed (Eq. 3.62).

$$\frac{\partial^2 \varphi(x,y,z,t)}{\partial x^2} + \frac{\partial^2 \varphi(x,y,z,t)}{\partial y^2} + \frac{\partial^2 \varphi(x,y,z,t)}{\partial z^2} = 0 \tag{3.61}$$

$$-\frac{\partial \varphi(x,y,z,t)}{\partial n} = 0 \qquad \forall x,y,z \in CS \tag{3.62}$$

The three-dimensional velocity potential has been solved by (Graham and

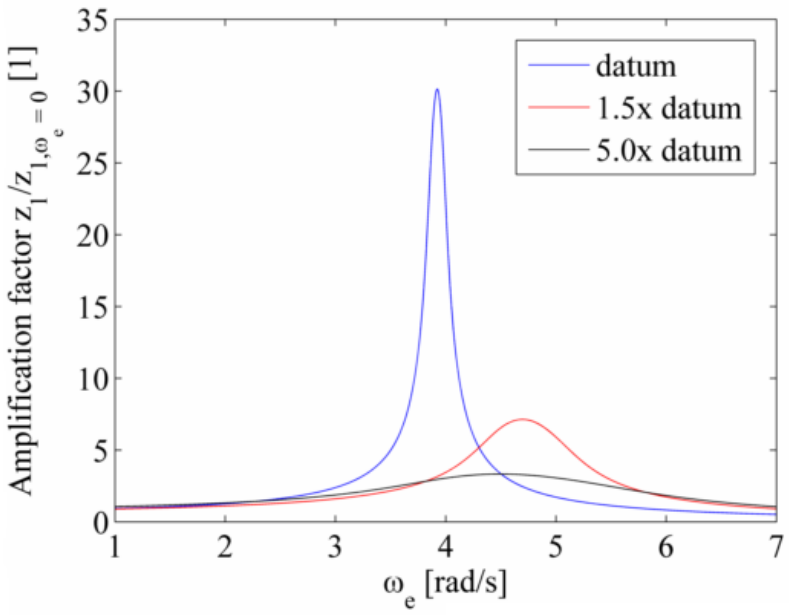

Fig. 3.15 Forced response in the frequency domain: datum (blue), 1.5x datum (red), and 5x datum (black)

Rodriquez, 1951) which is reproduced in Eq. 3.63.

$$\varphi(x,y,z,t) = \sum_{m=0}^{\infty}\sum_{n=1}^{\infty} A_{mn}(t)\cos\left(\frac{2m\pi}{W_w}\right)\cos\left(\frac{2n\pi}{B_w}\right)\cosh\left[k_{mn}\left(z+h\right)\right] \tag{3.63}$$

where $k_{mn} = \pi\sqrt{\frac{4m^2}{W_w^2}+\frac{4n^2}{B_w^2}}$.

Substituting the velocity potential (Eq. 3.63) into Laplace's Equation (Eq. 3.61), the natural frequencies can be calculated (see Eq. 3.64) . The surface tension is neglected, which is a sensible approach as typical OWC length scales are much greater than the capillary length for the air-water interface ($\tilde{2}$ mm according to Batchelor (2000)).

$$f_{mn} = \frac{1}{2\pi}\sqrt{g\,k_{mn}\tanh\left(k_{mn}L_w\right)} \quad [\text{Hz}] \tag{3.64}$$

Caisson designs should allow at least 100% frequency separation between the heave-mode frequency and any of the sloshing mode frequencies. The have-mode resonant frequency varies depending on the sea state, and therefore, this variation needs to be taken into account for the particular location of the OWC power plant. This criterion effectively limits the maximum free-surface area.

3.6 Summary

This chapter has presented the development and validation of a nonlinear reduced-order model for forced response of water column. It has been derived utilising the integral form of the Conservation Laws and a collocation method. Model coefficients have been calibrated by a higher-fidelity CFD method (ANSYS Fluent®). Sixteen different caisson geometries are exten-

sively analysed in 66 test cases in order to derive correlations between the model coefficients and the design parameters.

The original contributions in this chapter are:

(1) A nonlinear stochastic reduced-order model for water column oscillation forced response prediction under irregular wave conditions has been developed. This method has been derived from the integral form of Conservation Laws and a collocation method.

(2) A parametric model for water column added mass, dissimilar radiation coefficients for both exhaust and intake strokes, and hydrodynamic restoration coefficient.

Chapter 4

Turbine Design and Optimisation for Oscillating Water Column Power Plants using a Multi-Fidelity Design System

4.1 Introduction

The objective of the work presented in this chapter is to design and optimise a power turbine for a generic OWC device. The aim is to maximise the aerodynamic efficiency, achieve acceptable steady mechanical stress, and minimise the turbine pressure ratio.

The optimised turbine for a generic OWC application is the baseline turbine design for the system-level optimisation performed in Chapter 6.

4.2 Design Method

The design space for the OWC turbines is still fairly unexplored, and none of the existing turbines fully complies with the requirements (cf. Webb et al., 2005). In this work, the design is carried out by a multi-fidelity design framework (schematically shown in Fig. 4.1) which integrates a set of tools described in the following sections. New design iterations can be quickly evaluated, and then, progressed to higher fidelity assessments when certain pass-off criteria are met. The low-fidelity methods *explore* the design space, and the high-fidelity methods *exploit* and validate the results from lower fidelity solutions as described by March and Willcox (2010).

The proposed multi-fidelity design framework comprises the following steps:

(1) Gas path and blade design using a Non-Isentropic Radial Equilibrium (NISRE) solver coded in Matlab® (Hirsch and Denton, 1981);

(2) Pre-processing of two- and three- dimensional simulations;

(3) 3D blade generation which are based upon the NISRE solution;

(4) Multi-point through-flow simulation using Vista™ TF (Casey and Robinson, 2010), which solves the circumferentially averaged inviscid Navier–Stokes equations, supplemented by established empirical models for losses and deviation;

(5) Three-dimensional mesh generation using PADRAM (Shahpar and Lapworth, 2003) which includes detail geometry such as tip clearance and hub fillet radius; and

(6) 3D uRANS CFD simulation (Sayma et al., 2000).

These processes and simulations are scripted and automated in Matlab®.

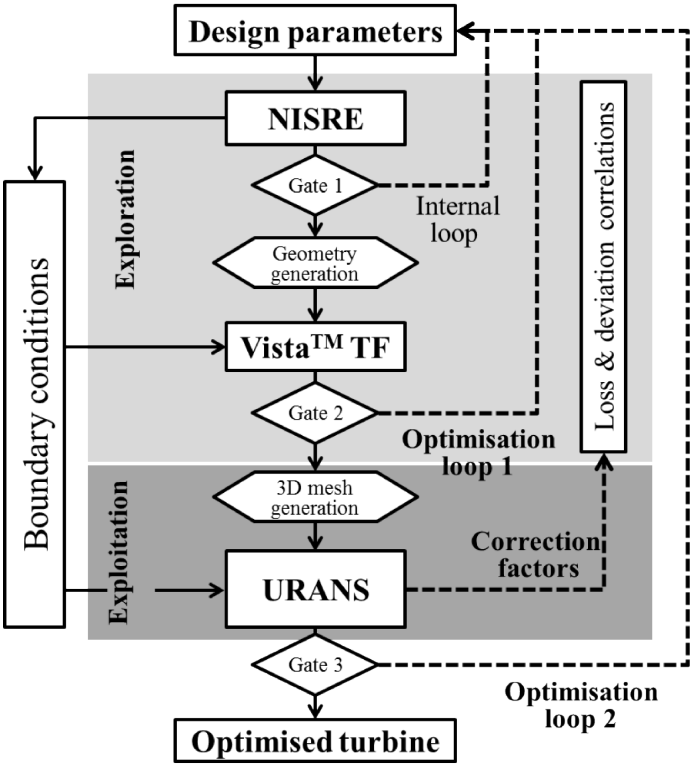

Fig. 4.1 Multi-fidelity design system and optimisation process

4.2.1 Non-Isentropic Simple Radial Equilibrium (NISRE) Solver

The core of the design system is founded on the NISRE equation (Eq. 4.1) which is resolved in the meridional flow passage ($x-r$ plane). The plane is subdivided in calculation stages between the blade rows. The NISRE solution provides the flow velocity profiles (the radial component of velocity is neglected) and thermodynamic properties (see Fig. 4.2). Compressible flow relations are applied as high-speed subsonic flow turbines are also included in the design space.

$$\frac{\partial H_0}{\partial r} - T\frac{\partial s}{\partial r} = v_t\frac{\partial v_t}{\partial r} + \frac{v_t^2}{r} + v_x\frac{\partial v_x}{\partial r} \quad (v_r \approx 0) \tag{4.1}$$

The integration of Eq. 4.1 is carried out using iterative numerical methods. The flow is assumed isentropic in the first iteration to initialise the solver. Subsequently, the entropy gradient is derived from the profile and secondary loss based on the previous iteration flow solution, and this process is repeated until convergence is achieved.

The profile and secondary losses are calculated using Craig and Cox (1970) loss correlation. The tip leakage loss is derived from Ainley and Mathieson (1951) correlation which allows both shrouded and unshrouded turbine blade rows to be considered. The tip clearance loss is not included in the NISRE equation integration as the tip flow does not result in any work, and therefore the loss is added as an overall efficiency penalty to the blade row.

The design is produced at a given condition, the so-called *design point*. Conventional turbine design-point operation implies very little or slightly negative flow incidence onto the blade. However, bi-directional alternating flow conditions in the OWC turbine do not allow this desired characteristic. New design criteria are required to deal with this fact and achieve enhanced off-design performance.

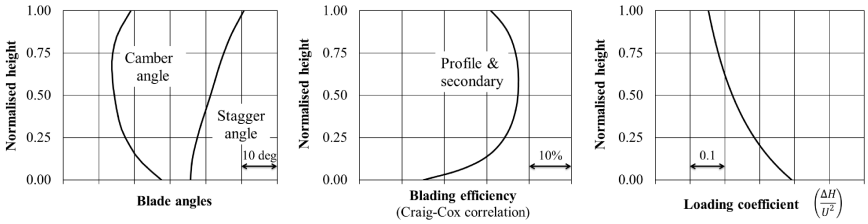

Fig. 4.2 Example of variables calculated using the NISRE equation

The NISRE solver also performs a simple maximum centrifugal stress calculation at the blade root as shown in Eq. 4.2 (cf. Horlock, 1966) for which the limit is set according to usual turbomachinery design rules: 25% of the material yield strength. Other contributing factors to the total stress such as steady gas loads or unsteady pressure loads (alternating stress) are not taken into account.

$$\sigma_c = 2\pi A_{\text{annulus}} N^2 \rho_m \tag{4.2}$$

The NISRE solver also generates the required data to create both the input geometry for Vista™ TFand the three-dimensional mesh generator (PADRAM): the blade inlet and outlet angle, stagger angle, maximum thickness, leading edge and trailing edge radii, etc. at twenty-one streamsurfaces. Radial profiles of velocity components and the thermodynamic properties are calculated and they can be used as boundary conditions in Vista™ TFand uRANS simulations (see Fig. 4.1).

4.2.2 Geometry generation

The NISRE solution is used to create the three-dimensional blade geometry (as shown in Fig. 4.3) which is generated by linearly stacking two-

dimensional aerofoil profiles; each defined by a parabolic camber line, thickness distribution, and parabolic leading and trailing edges.

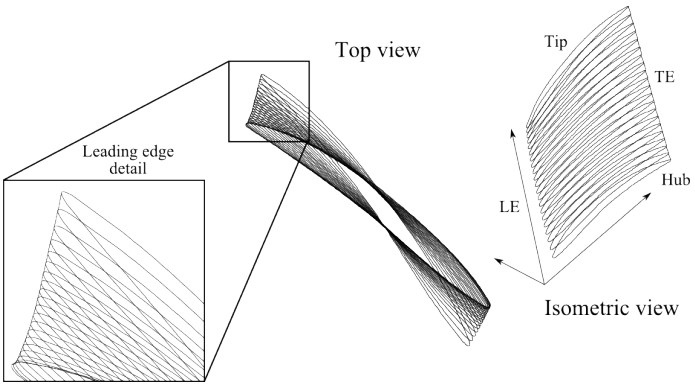

Fig. 4.3 Blade geometry generation by aerofoil profile stacking. Parabolic leading edge detail (left)

4.2.3 Multi-Point Radial Equilibrium Through-Flow Solution

The aim of the through-flow simulations is to generate the turbine map which is calculated using the through-flow solver Vista™ TF. More information about this solver and validation can be found in Casey and Robinson (2010). The input files are automatically generated by the NISRE solver. Fig. 4.4 depicts an example mesh and flow contours (note the inlet end-wall boundary layer profiles). The loss correlations are updated as shown in Fig 4.1.

4.2.4 Three-Dimensional Mesh Generation

Structured mesh with *H-O-H* topology for each blade row is generated by PADRAM (see Fig. 4.5) which is used for the uRANS simulations. The expansion of the O-grid follows a hyperbolic sine law which enables refinement of the y^+ values close to the wall without increasing the number of elements

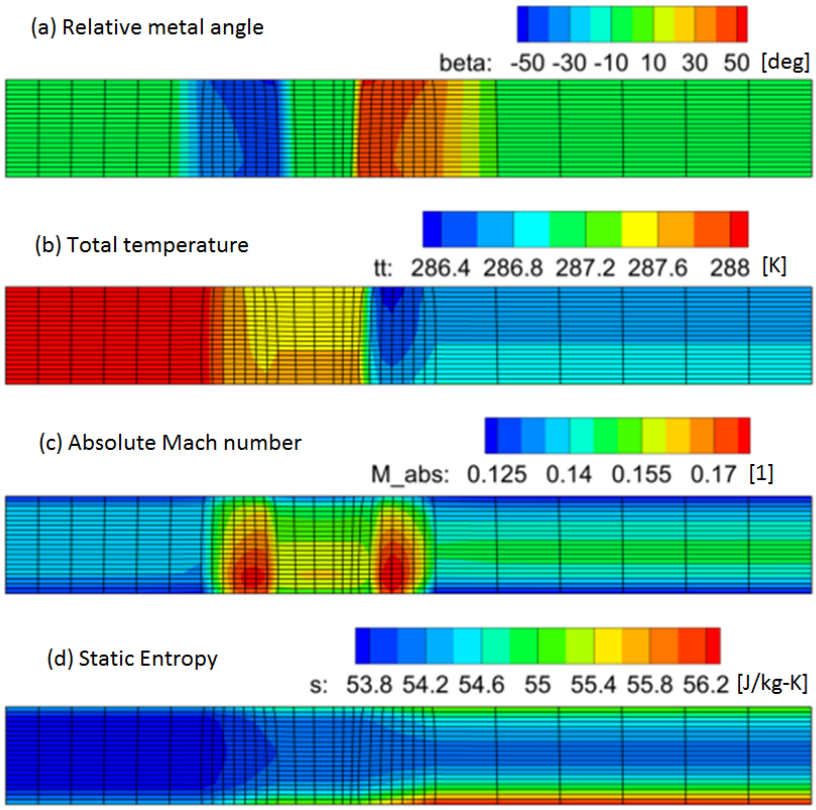

Fig. 4.4 Mesh and flow contours calculated using Vista™ TF

in the grid. This y^+ refinement enables to accurately modelling high flow incidence conditions.

The three-dimensional mesh includes detail features like hub fillets and tip gap for which butterfly topology is utilised. A tip gap of 0.5% based on the blade height has been assumed. All these mesh details are shown in Fig. 4.5.

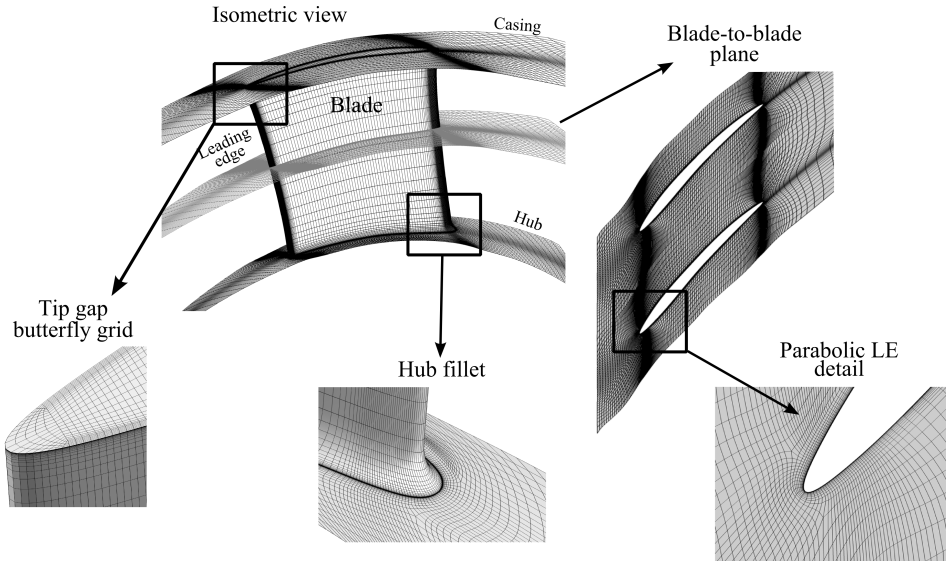

Fig. 4.5 Three-dimensional CFD mesh generated for uRANS simulations

4.2.5 Three-Dimensional uRANS Simulations

Unsteady Reynolds Averaged Navier-Stokes (uRANS) simulations are performed using a dual-time stepping compressible flow solver and the Spalart-Allmaras turbulence model. The blade rows interface utilising sliding planes. The inlet boundary conditions are total temperature, total pressure, and flow angle radial profiles generated by the NISRE solver. In order to account for a more realistic environment, the inlet profile contains end-wall boundary layers. NISRE-generated radial static pressure profile is imposed at the outflow boundary. Only one blade passage is included in the analyses, and periodic

boundary conditions are applied to the sides of the CFD domain. The number of blades per row is a design parameter through the chord-to-pitch ratio.

The uRANS simulations are not carried out imposing time-varying boundary conditions as OWC unsteady turbine performance can be accurately derived from the steady characteristics as reported by Inoue et al. (1988). The steady boundary conditions are valid since the oscillation period is much greater than the time that flow particle remains in the turbine.

Time-accurate simulations and sliding planes are required to accurately analyse the high flow incidence conditions occurring during most of the operation of the OWC turbine and blade row interaction. The uRANS solutions are time-averaged and subsequently used to train the loss and deviation correlations in NISRE and Vista™ TFas schematically shown in Fig. 4.1.

The calibration process of the NISRE solution and Vista™ TFcomprises the correction of the mid height tangential velocity component as depicted in Fig. 4.6. The shape of the distribution remains unchanged. The overall row efficiency derived from the uRANS simulations are factored in the Craig-Cox loss correlation. The same approach is applied to the loss calculation in Vista™ TFwhich allows including correction terms for the built-in loss correlations.

Fig. 4.6 also shows the axial velocity component calculated by the three methods. The biggest discrepancy was found at the hub for which the NISRE method predicts less blockage than the other two methods, but the agreement is fit for purpose. The axial velocity component is therefore not calibrated.

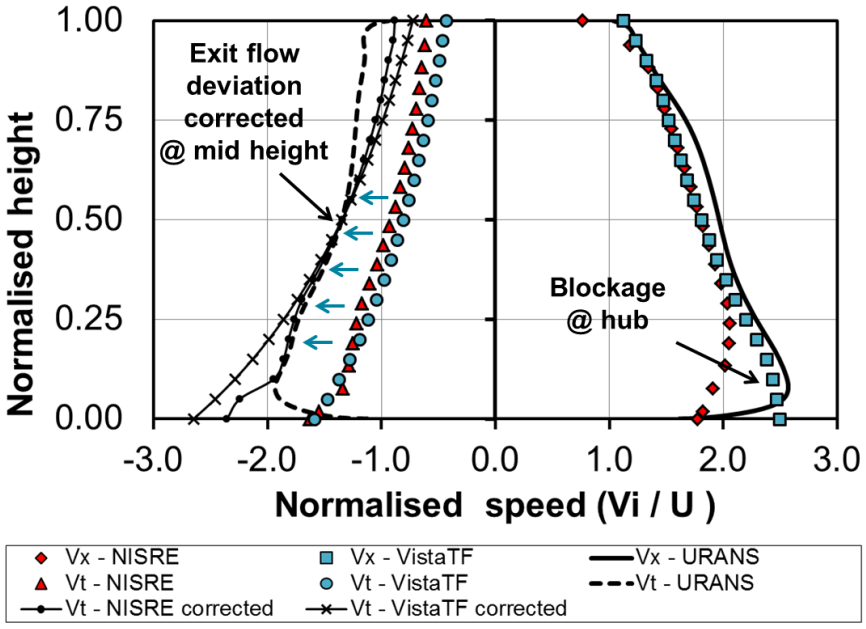

Fig. 4.6 Comparison of radial velocity profiles calculated using NIRSE, Vista™ TF, and uRANS calculations

4.3 Multidisciplinary Turbine Design Optimisation

4.3.1 Turbine Architecture

OWC turbines work in a constantly bi-directional alternating flow environment. Therefore, some peak efficiency has been sacrificed in order to retain off-design performance over broader flow conditions, and thereby, efficient installed operation within the OWC. The following design criteria are based on the previous turbine experience presented in Chapter 2:

(1) Efficient operation in reverse flow conditions;

(2) efficient operation for a very wide flow range;

(3) very-low pressure drop (i.e. low-turning axial turbine);

(4) no stator rows (variable or fixed);

(5) axial-inlet axial-outlet flow conditions;

(6) low mechanical steady stress;

(7) controlled-vortex blade design (twisted aerofoil);

(8) adequate speed of rotation to drive an electrical generator; and

(9) flow acceleration through each blade row in its own frame of reference.

A novel axial Vane-Less Contra-Rotating Turbine (VLCRT) design (patent application number GB1415992.5) is presented in this thesis resulting from the aforementioned design criteria (see Fig. 4.7). This turbine design has been shown to be a valid alternative as it has a number of desirable features: higher efficiency over a wider working range compared to the Wells or the impulse turbines, and low outlet swirl, while the mechanical simplicity is retained. This design is a low-pressure drop ducted turbine which comprises

two contra-rotating rotors, which maintain their sense of rotation independently of the flow direction. The two rotors have fixed blades of aerofoil cross-sections, which are cambered and staggered. The turbine blades are twisted to control the vortex flow. There is no need for any stator, swirling or de-swirling vanes either fixed or variable.

The principle of the VLCRT turbine is schematically shown by the velocity triangles in Fig. 4.7. The exit swirl from rotor A is fed in rotor B which rotates in opposite direction to the former. This feature removes the need for nozzle guide vanes. A good VLCRT should keep rotor B outlet swirl as low as possible in order to minimise the exit loss (kinetic energy and duct losses). Note that the flow always accelerates in the relative frame through the first ($w_{1A} < w_{2A}$) and second rotor ($w_{2B} < w_{3B}$).

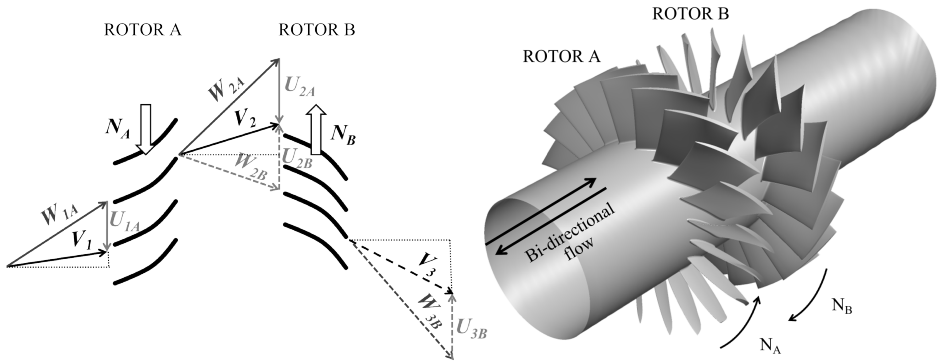

Fig. 4.7 Vane-Less Contra-Rotating Turbine (VLCRT) for OWC power off-take: velocity triangles (left) and 3D isometric view (right)

4.3.2 Parameterisation

The turbine is defined by two families of design parameters –17 in total–. First, *global* turbine parameters:

(1) Loading coefficient ψ;

(2) flow coefficient ϕ;

(3) inlet axial Mach number at mid height M_1;

(4) chord-to-pitch ratio at the tip $(c/g)_{\text{tip}}$;

(5) rated power P_{T};

(6) hub-to-tip ratio $D_{\text{hub}}/D_{\text{tip}}$;

(7) height-to-chord ratio at the tip $(h/c)_{\text{tip}}$; and

(8) rotor speed ratio N_A/N_B.

The second family of parameters determines the turbine blade *detail geometry*: rotor (9-14) vortex-law coefficients, A_1 , B_1 , C_1 , A_2 , B_2 , C_2; (15) thickness-to-chord ratio, t/c, (16) leading thickness, $R_{\text{L/E}}$, and trailing edges thickness $R_{\text{T/E}}$. The blade angles are defined according to a combination of free and forced vortices as shown in Eq. 4.3.

$$v_t = A\frac{r_m}{r} + B + C\frac{r}{r_m} \tag{4.3}$$

The turbine presented here is designed using identical rotor bladings, symmetrically positioned, and the speed ratio $N_A/N_B = -1$. Therefore, the turbine operation should be the equivalent for both inhalation and exhalation.

4.3.3 Objective Function

The objective function encompasses several turbine attributes some of which are determined by customer requirements such as rated power, but some others which are discretionary related to the aerodynamicist and mechanical engineer in order to achieve the best performance. The optimisation constraints play a major role in any successful optimisation run. The design optimisation

shown in this work includes the constraints in a pseudo-objective function (Eq. 4.4) as penalty functions, the so-called weak formulation (cf. Verstraete, 2010). This approach is especially beneficial in the case presented in this work as the constraints are applied to output variables rather than design parameters.

$$\min \quad \widetilde{f}(\vec{x}) = f(\vec{x}) + \sum_j w_j g_j(\vec{x}) \tag{4.4}$$

where the objective function (Eq. 4.5) is a weighted function of:

(1) On-design total aerodynamic loss, $1 - \eta_{\mathrm{VLCRT}}$;

(2) Sensitivity of the efficiency to pressure ratio, $\partial\eta/\partial\mathrm{PR}$ around the design condition (as measure of robustness of the efficiency peak);

(3) Centrifugal steady stress-to-yield strength ratio, $\sigma_\mathrm{c}/\sigma_\mathrm{y}$ which is only active when σ_c is significant (see Eq. 4.6); and

(4) Turbine total pressure ratio, $\mathrm{PR} = P_{01}/P_{03}$.

$$\begin{aligned} g(\vec{x}) = w_1 \left(1 - \eta_{\mathrm{VLCRT}}(\vec{x})\right) + w_2 \left(\frac{\partial\eta(\vec{x})}{\partial\mathrm{PR}}\right)_{\eta=\eta_{\mathrm{peak}}} \\ + w_3 \left(\frac{\sigma_\mathrm{c}(\vec{x})}{\sigma_\mathrm{y}}\right)^n + w_4 \left(\frac{P_{01}}{P_{03}}\right) \end{aligned} \tag{4.5}$$

where

$$\begin{aligned} w_1, w_2 &\equiv Ct > 0.0,\ n > 1.0 \\ w_3 &= \begin{cases} cte > 0.0, & \text{if } \frac{\sigma_\mathrm{c}(\vec{x})}{\sigma_\mathrm{y}} > 0.25 \\ 0.0, & \text{otherwise} \end{cases} \end{aligned} \tag{4.6}$$

The weights w_i are chosen accordingly to the relative importance of the constraints, and the penalty functions $g_j(\vec{x})$ grow exponentially when the constraint is infringed. The constraints are the following:

(1) Area-averaged turbine absolute exit flow angle, $|\alpha_3| < 30$ deg;

(2) Maximum and minimum flow turning 10 deg $< \Delta\beta_{\text{blade}} <$ 40 deg;

(3) Minimum total enthalpy drop $\Delta H_0 > 0$;

(4) Maximum relative inlet Mach number $M_w < 0.6$; and

(5) Maximum absolute Mach number $M < 0.5$.

4.3.4 Optimisation Algorithm

Successful optimisation process requires screening the entire design space which is spanned by a very large number of candidates defined by the combination of the design parameters. Time constraints do not allow analysing each individual of the design space in detail. There are typically three strategies to accelerate the optimisation process: improve computational power (multi-core or GPU computing), faster low-fidelity methods, or interpolation methods using a metamodel, also named surrogate model (cf. Verstraete, 2010). The work presented in this study utilises various low-fidelity methods and experimental aerodynamic loss correlations to *explore* the design space as shown in Fig. 4.1.

The multi-fidelity design system is fully automated through scripting, and a full design iteration loop, including uRANS CFD simulations, takes about two or three days on a typical PC workstation (12-core Intel® Xeon® CPU).

The optimisation is performed using stochastic evolutionary optimisation (genetic algorithm) as described by Shahpar (2002). The initial population is generated using Design of Experiments (DoE) by means of Optimised Latin

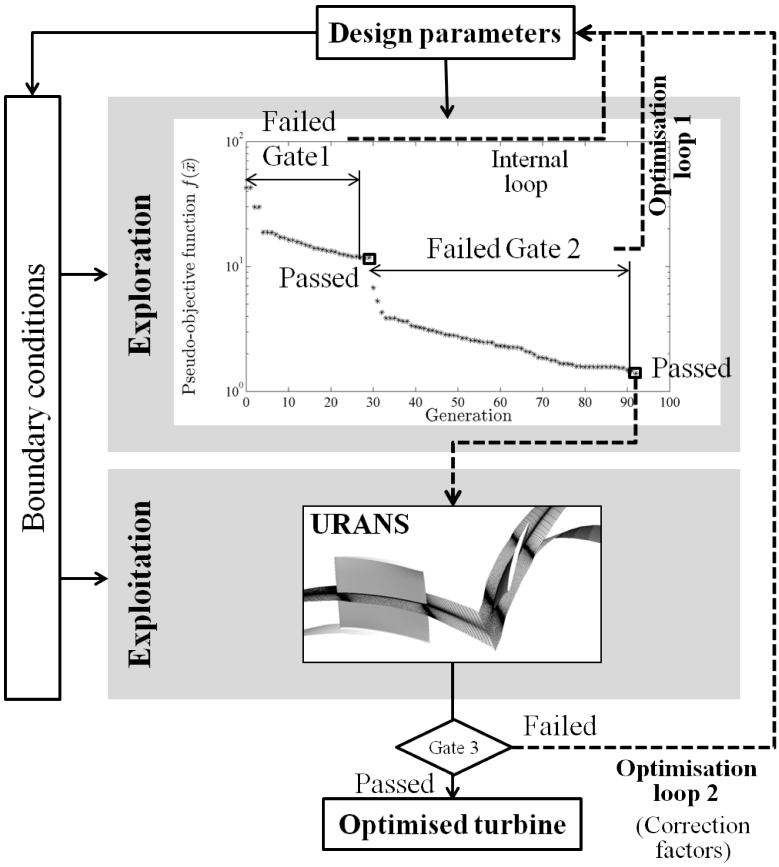

Fig. 4.8 Convergence history of pseudo-objective function $\widetilde{f}(\vec{x})$ and gated optimisation process

Hypercube Sampling (OLHS). The principal advantage of the stochastic optimisation methods is they can operate on irregular functions and seek solutions from disjointed feasible domains, and the simulation codes can be treated as black boxes.

The optimiser settings used for the genetic algorithm are one population of 20 individuals with a maximum number of generations equating to 100. The crossover probability is 0.8, and the inversion probability is 0.2. The method of selecting the individuals to become parents can be either roulette or tournament. Both of these methods have been tried with satisfactory results. Elitism is also used in order to allow for local search in the regions where the best two individuals are found as they are passed unchanged to the next generation.

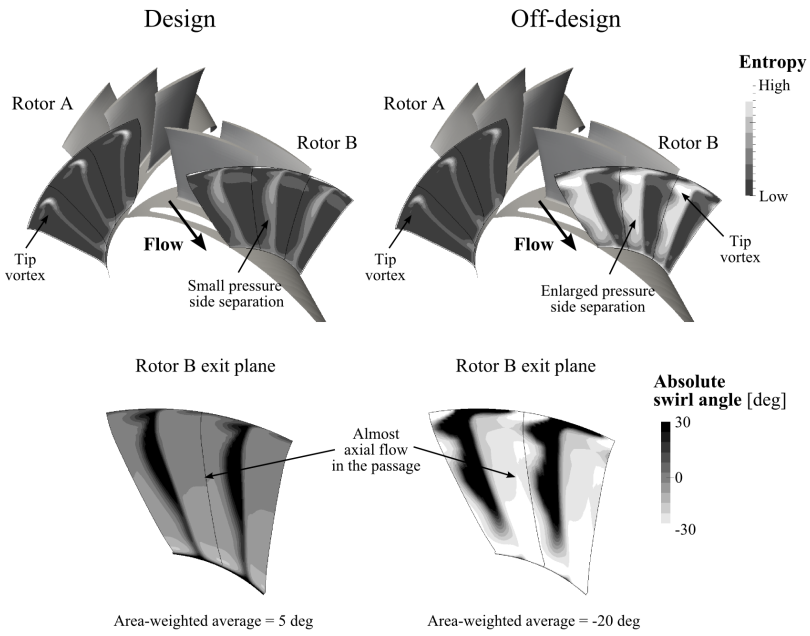

Fig. 4.9 Comparison of on-design (left) and off-design (right) flow contours $\phi_{\text{off-design}} = 1.4\,\phi_{\text{design}}$, $\text{PR}_{\text{off-design}} = 1.002\,\text{PR}_{\text{design}}$, $\eta_{\text{off-design}} = 0.94\,\eta_{\text{design}}$

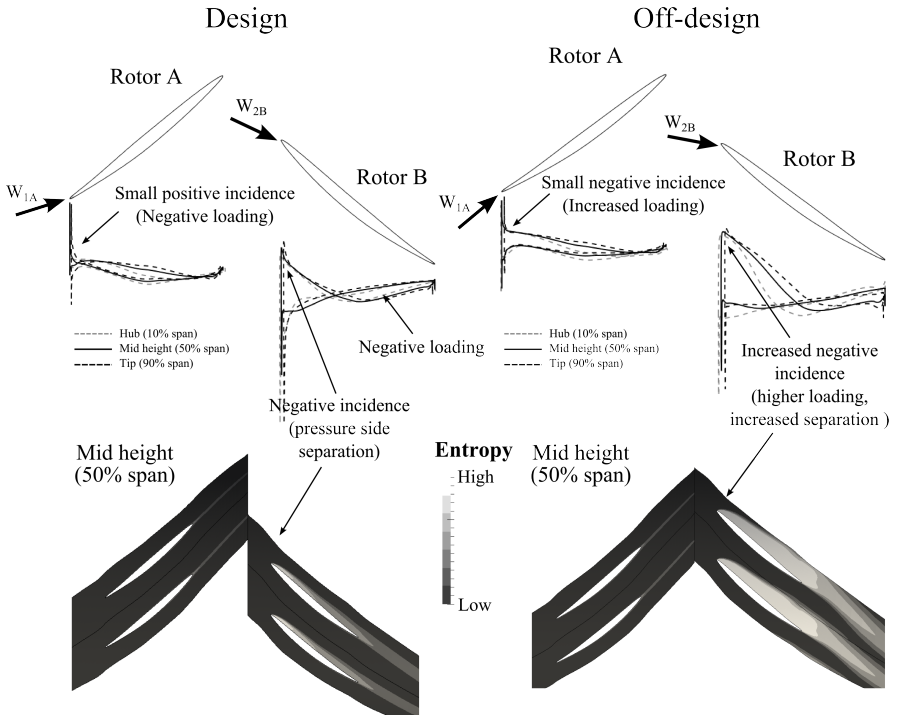

Fig. 4.10 Comparison of on-design (left) and off-design (right) time-averaged pressure distributions (top) and entropy contours in the blade-to-blade surface (bottom) at mid height

$\phi_{\text{off-design}} = 1.4\,\phi_{\text{design}}$, $\text{PR}_{\text{off-design}} = 1.002\,\text{PR}_{\text{design}}$, $\eta_{\text{off-design}} = 0.94\,\eta_{\text{design}}$

4.4 Optimisation Results

A typical exploration phase of the genetic algorithm generates between 50 and 100 generations of 20 individuals each (NISRE + Vista™ TF). Fig. 4.8 depicts an example run of the exploration stage convergence history in the context of the optimisation loops. The initial generation is sparsely distributed over a very large design space. However, the pseudo-objective function (Eq. 4.4) was defined in such a way that the algorithm had enough information to successfully continue with the process. A large number of designs were rejected during the NISRE evaluation as one or various design constraints were not fulfilled which failed *Gate 1* (shown in Fig. 4.1 and Fig. 4.8). This first gate eliminates unfeasible designs and greatly reduces the likelihood of failed simulations in the subsequent stage (Vista™ TF).

The best individual at the end of the exploration is promoted to the exploitation stage for which uRANS simulations are performed at various conditions. At the end of the latter stage, blade row loss and deviation are compared to the profiles generated by the lower-order methods. If the error is below certain limit, the optimisation process stops. Otherwise, the loss and deviation correlations in the NISRE solver and Vista™ TFare updated as described before, and the optimisation process continues.

The initial population generated by the OLHS was highly unsatisfactory since most of the individuals have showed very high flow Mach number, very high speed of rotation, excessive flow incidence onto the blade rows, high aerodynamic loss, compressing rotor, etc. which are *Gate 1* criteria. None of those individuals were promoted to higher fidelity methods being discounted in a few seconds. The optimiser quickly improved the design assisted by the imposed constraints using exponential penalty functions. The best individual of the exploration run was analysed using uRANS, and only two or three of those loops (optimisation loop 2 in Fig. 4.1) are required to achieve an optimised design.

Fig. 4.9 (top) depicts the entropy contours at the rotor A and B exit planes.

Rotor A exhibits very good performance for both design and off-design operation. Rotor B performs slightly worse as expected since pressure side boundary layer separation occurs. Rotor B performance neither steeply falls nor to a great extent since the boundary layer detaches in a controlled manner. This separation does not greatly penalise the performance, even off design, as pressure side separation has been enforced during the optimisation process. Note that the performance (η) drops only circa 6% between design (left) and off design (right), even though the flow coefficient (ϕ) increases around 40%. Therefore, the VLCRT turbine shows an slightly improved peak efficiency and greatly superior performance at high flow coefficients for which the Wells turbine stalls (turbine characteristics shown Fig. 4.4). On the other hand, the boundary layer separation provides a contracting aerodynamic passage as a converging geometric passage cannot be generated simultaneously for both inhalation and exhalation with a fixed geometry.

Fig. 4.9 (bottom) shows the absolute swirl angle at the rotor B exit plane half chord downstream of the blade. This flow variable has been constrained during the optimisation process in order to achieve low outlet swirl. The area-weighted average exit swirl angle is around 5 deg on design and drops to -20 deg off design, which is an acceptable range. N.B. the total pressure ratio increases only 0.2% from design to the off-design condition shown which adds constant stiffness and damping to the water column. The axial vane-less architecture and the low turning blade design result in a low pressure ratio turbine.

Lift plots are depicted on- and off-design in Fig. 4.10 (top). Rotor A is less loaded than rotor B. Rotor A incidence has a crossover point going from a small positive incidence (≈ 5 deg) to a negative incidence (≈ -15 deg) which slightly increases the loading. Note that Rotor B always sees positive incidence (≈ -40 deg on design). The lift distribution is not optimal, but areas of negative lift are minimised. The lift distributions are very similar along the blade height (hub, mid height, and tip are shown), although the vortex law

slightly increases the loading at the mid height sections.

Even off design, there is no aerofoil stall unlike the Wells turbine. The lift distribution shape does not change significantly over a very wide flow range (ϕ_{design} to $1.4\,\phi_{\text{design}}$). The requirement for symmetric bladings does not allow improving this characteristic and it is not desirable to increase the flow incidence onto rotor A as this would have a knock-on effect on rotor B as well.

Fig. 4.10 (bottom) presents the entropy contours on the mid height blade-to-blade surface for the same conditions as the lift plots. Rotor A boundary layer remains attached over the whole running range in order to avoid spurious effects on rotor B. But then, rotor B suffers from pressure side separation which cannot be completely eliminated without greatly penalising the reverse-flow operation or the symmetric blading requirement. However, high turbine efficiency, low outflow angle, and the uttermost, positive lift are maintained in the operational envelope.

Fig. 4.11 presents the calculated turbine chics for the optimised design using Vista™ TFplus the corrections from the uRANS simulations. Peak efficiency is predicted circa 0.85 which moderately drops at higher mass flow rates. High efficiency is achieved over the considered pressure ratios up to PR=1.20. Increasing corrected turbine speed $N\sqrt{T_{01}}$ increases the efficiency at higher mass flows, however the mass flow through the turbine is reduced.

4.5 Summary

A multi-fidelity design system has been developed and it has been successfully applied to design and optimise a novel axial turbine architecture for OWC power off-take. The optimisation is accomplished by stochastic evolutionary algorithms using a multi-fidelity framework which enables an efficient use of the optimiser. The *exploration-exploitation* strategy allowed satisfactorily meeting the design criteria reducing the computational burden.

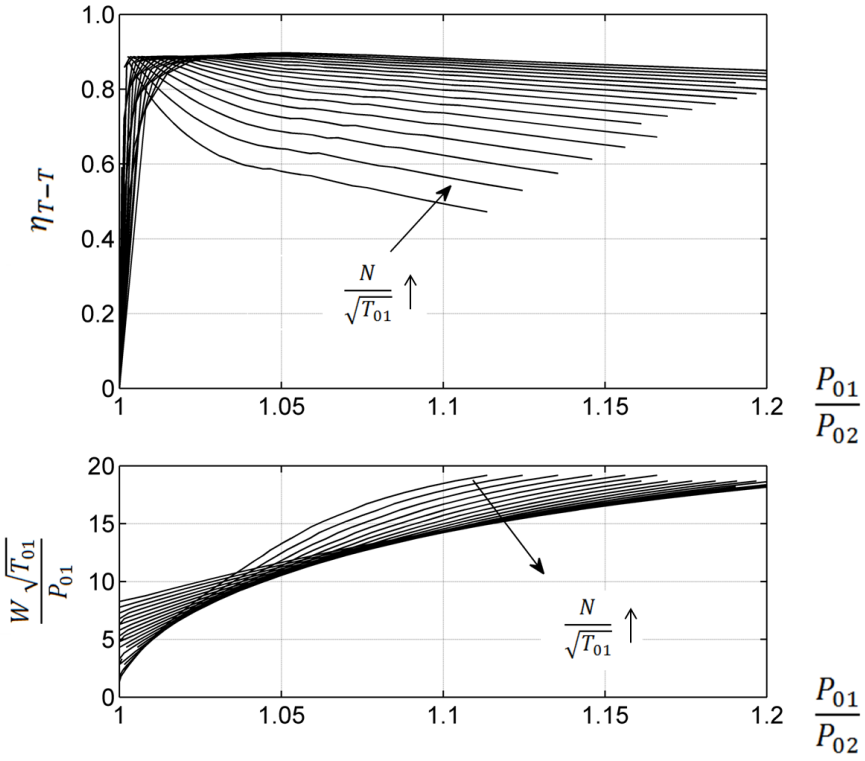

Fig. 4.11 VLCRT turbine characteristics

The main features of the optimised VLCRT are: (1) efficient operation in bi-directional alternating flow conditions over a wide flow range, (2) reduced outlet flow swirl without the need for outlet vanes which cause additional loss and reduce the available pressure drop for the rotor to produce useful work, (3) very-low pressure ratio, and (4) maximum centrifugal steady stress below 25% of the yield strength of the selected material.

The original contributions presented in this chapter are:

(1) The multi-fidelity design system comprising the Non-Isentropic Radial Equilibrium Equation (NISRE) and Craix-Cox loss model, Vista™ TFand uRANS simulations;

(2) an efficient implement of the exploration-implementation optimisation strategy based on low-order simulations (NISRE and Vista™ TF), and high-order simulations (uRANS); and

(3) an optimised reversible Vane-Less Contra-Rotating Turbine (VLCRT) design for OWC power off-take with outstanding aerodynamic efficiency and mechanical integrity.

Chapter 5

System Design and Evaluation

5.1 Introduction

Oscillating Water Column (OWC) power plants are complex systems which convert sea wave energy into high-quality electricity. This essential capability of the system is referred as *operational objective*. The integrating elements of the system must perform the required functions to fulfil the system purpose fitting in its context (i.e. environment and external systems which it interacts with). Integrating lower-level elements are usually referred to as sub-systems or components. All human-made systems have a life cycle which also needs to be understood, and the system must fit accordingly in all the phases, from conceptual design to decommissioning (cf. Blanchard et al., 1990).

In this chapter, the OWC power plant design and analysis are presented from the *Systems Engineering* perspective implementing a prior understanding of the system functionality, both desired and detrimental (see Haskins, 2011). Design criteria based on the *Voice of the Customer*, design synthesis (parameters and constraints) and evaluation method have been developed.

5.2 Conceptual Design

5.2.1 Viability of OWC Power Plants

Medium-term feasibility studies have been published by Webb et al. (2005), considering two different scenarios, for which the following conclusions are drawn:

(1) Shoreline OWC power plant: This configuration is seen as an alternative to diesel power generation in remote small communities.

- Rated power: circa 0.5MW
- Power production cost (demonstrator): 17.5p/KWh at 10% discount rate
- Power production cost (mature devices): 8.0p/KWh at 10% discount rate

(2) Near-shore OWC power plant: This configuration is suited for power supply above 2.0MW

- Rated power: between 2MW and 20MW
- Power production cost (demonstrator): 9.6p/KWh at 10% discount rate
- Power production cost (mature devices): 5.0p/KWh – 2.0p/KWh at 10% discount rate

The study presented focused on the large-scale commercial exploitation of OWC power plants. Therefore, the second scenario is selected for system design and evaluation: Near-shore OWC power plants with a rated power between 2.0 MW and 20.0 MW.

5.2.2 System Context Diagram

The System Context Diagram provides a top-level view of the system of interest and the systems which it interacts with.

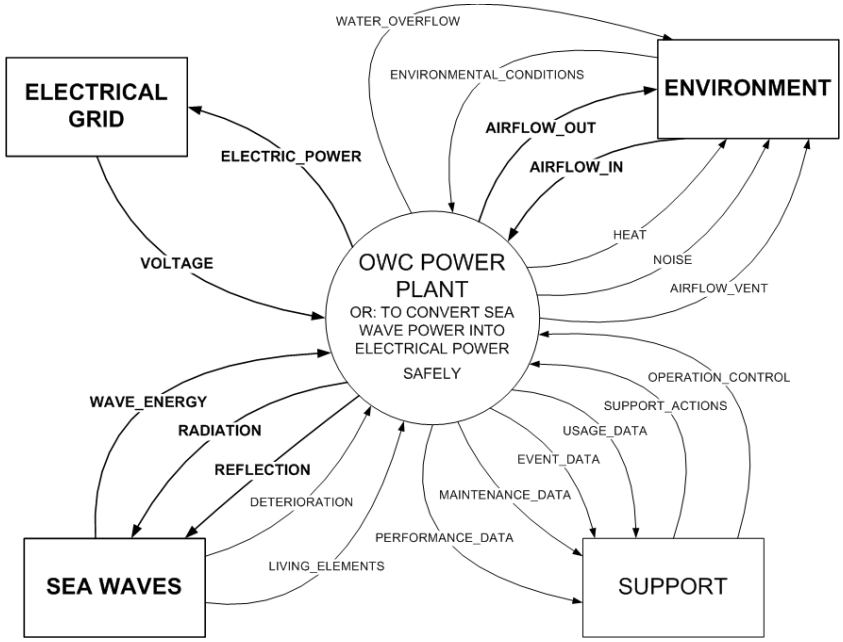

Fig. 5.1 System Context Diagram: OWC power plant

Fig. 5.1 depicts the interactions of the OWC power plant system with the following external systems:

(1) Electrical Grid: Grid operators (usually electricity companies), which set the electrical power specifications, are relevant stakeholders. The requirements for electricity grid connection have been summarised below (Troester, 2009):

(1) Normal operation: voltage range, frequency range, and active and reactive power control

(2) Behavior under grid disturbances: high and low voltage ride through, reactive current injection, sub-synchronous resonance

(3) Applicable electrical safety regulations and legislation.

(2) Sea Waves: The power plant harvests sea wave power whose characteristics will influence the power plant design to maximise efficiency

and ensure mechanical integrity. Thus, accurate wave resource characterisation is required.

(3) Environment: Waste energy such as noise or heat is discharged to the environment as the OWC is an air-breathing device. The environmental conditions at the power plant location greatly influence the design. Environmental policies and regulations must be observed.

(4) Support System: The purpose of this system is to maintain, repair, and ensure the adequate operation of the power plant. Accessibility, remote monitoring, and training needs are defined by this system.

5.2.3 Functional Modelling

Functional Modelling is a critical activity in conceptual design. It focuses on *what* needs to be done rather than *how* it needs to be done in order to accomplish the operational objective. The functional model also provides an overview of the system architecture for which the functionality must be solution-independent.

Functional Flow Diagram is a widely used tool for functional modelling. Fig. 5.2 shows the Functional Flow Diagram for OWC power plant during operation. Although functional analysis encompasses the whole of the life-cycle (design, development, operation, support, and decommissioning), the scope of this Thesis is limited the power plant operation.

Fig. 5.2 depicts the functions performed by the OWC power plant to convert wave power into electricity:

(1) Generate oscillation (F1): Wave energy is converted into free-surface displacements. These oscillations radiate energy back to the open sea altering the flow field. Pressure acting on the free surface influences this function.

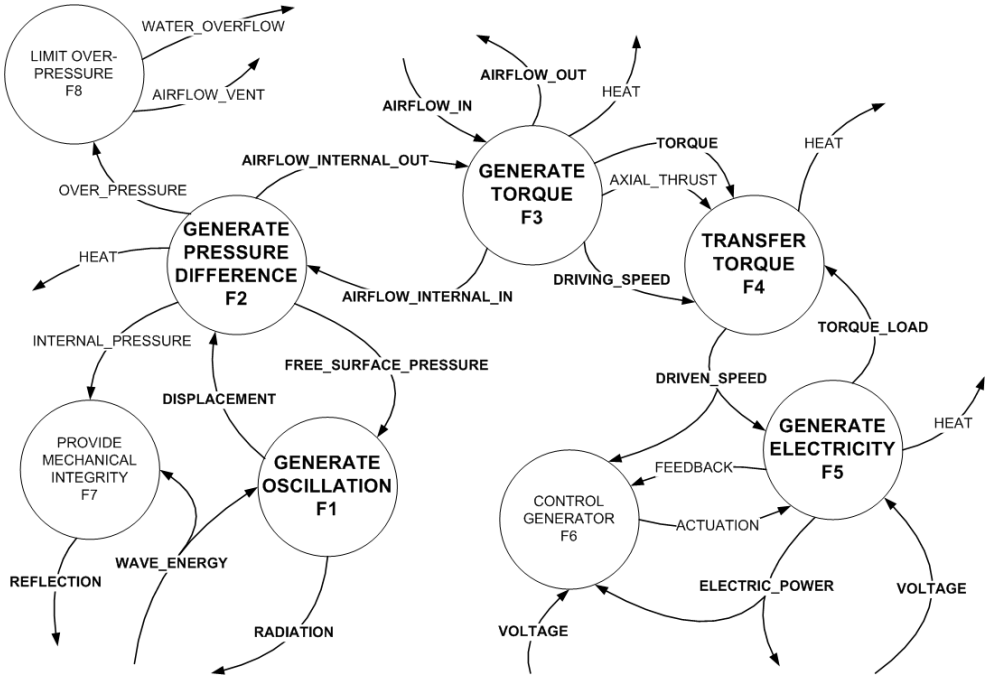

Fig. 5.2 Functional Flow Diagram: OWC power plant system - Diagram 0

(2) Generate pressure difference (F2): The pressure difference between the OWC power plant and the atmosphere generates an alternating airflow due to air chamber volume variation. Air is ingested through the turbine from the atmosphere.

(3) Generate torque (F3): Mechanical torque is generated from turning in the turbine. This element of the system requires intake and exhaust, and connection to the shaft.

(4) Transfer torque (F4): Driving torque must be transferred and axial thrust loads must be balanced. Torque resistant load shall be overcome by the driving torque.

(5) Generate electricity (F5): The driving torque creates a rotating electromagnetic field which is converted into electricity.

(6) Control generator (F6): A system is required to control the electricity generation process so that the grid connection requirements are met.

(7) Provide mechanical integrity (F7): Wave loads can be significant, especially in storm conditions, which have to be withstood. Additionally, pressure difference must be resisted.

(8) Limit pressure (F8): A safety function is required to limits the water elevation avoiding overflows and to limit the maximum pressure in the system.

5.2.4 System Architecting

The system architecting process has been used to organise the system functionality according to interfaces between functions to shape the physical architecture based on the functional architecture.

Information about the interconnection between system function can be assessed using the so-called N^2-chart. The system functions are shown in

the diagonal, and the number of interfaces between each function in the off-diagonal terms (being row-wise elements the outputs). The N^2-chart analysis aids to reveal complex interactions between functions (which usually are clustered in a sub-system), control loops, simple flows, and critical functions. Detailed information about the N^2-chart can be found in Shishko and Aster (1995).

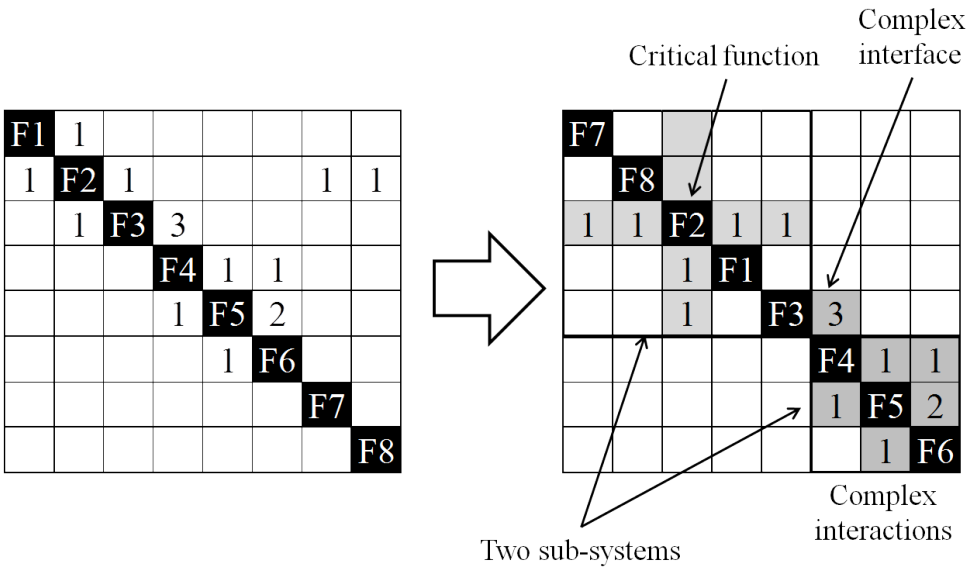

Fig. 5.3 OWC power plant N^2-charts: original (left) and modified (right)

Fig. 5.3 presents the N^2-chart derived from the Functional Flow Diagram on Fig. 5.2. The functions are rearranged such that a critical function (F2) and the complex interactions among functions F4,F5, and F6 are shown. The torque generation function (F3) and the torque transfer function (F4) are interconnected by a complex interface which is usually indication of a problem hot-spot in terms of design, operation, and maintenance.

Fig. 5.4 depicts The system functions grouped into two sub-systems:

(1) Mechanical Power Generator, SS1; and

(2) Electrical Power Generator, SS2.

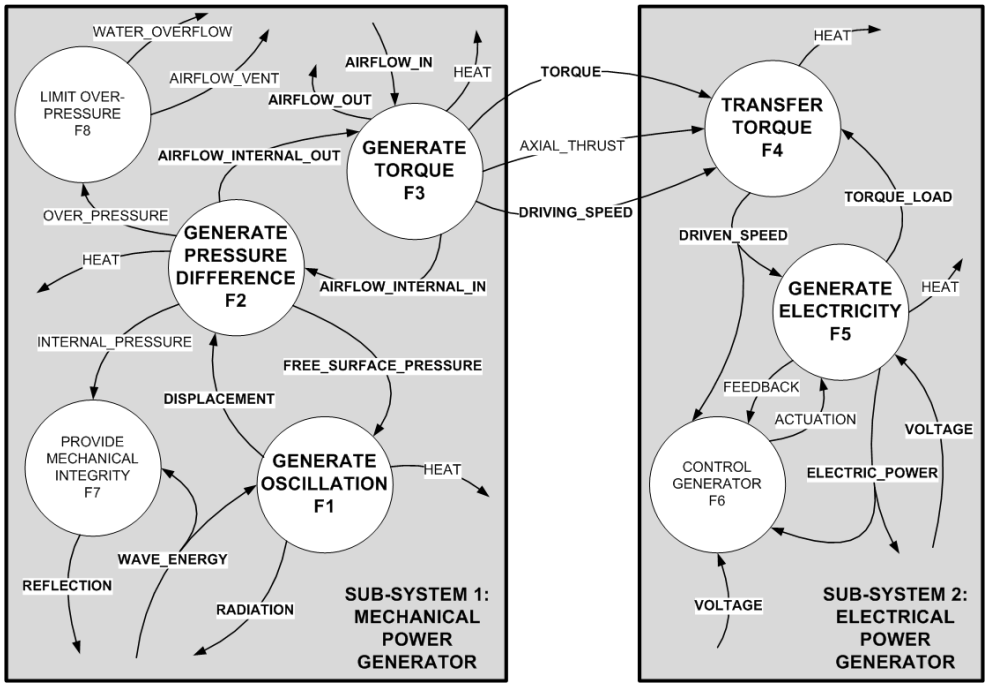

Fig. 5.4 Functional Flow Diagram: Diagram 0 and sub-systems

5.2.5 Quality Function Deployment

The objective of the Quality Function Deployment (QFD) is to ensure that the quality is built into the system right at the beginning of its life cycle (concept design). Therefore, the design attributes (the *hows*) fulfill customers and stakeholders needs (the *whats*).

The House Of Quality (HOQ) is the basic tool to convert the *Voice of the Customer* (VoC) into system functionality and to help prioritising the design effort. The HOQ transforms the customer and stakeholder needs, usually imprecise, into Non-Functional Performance Requirements (NFPR). The NFPRs are quantitative values associated to each of the system functions which can be traced back to the VoC using the HOQ. Should the NFPRs not be achieved, the risk of failing to deliver the stakeholder requirements can be assessed.

Fig. 5.6 presents the HOQ for a generic OWC power plant system which meets the viability criteria described at the beginning of this chapter. Electrical Grid Operator view, peer review, and the relevant environmental legislation applicable to OWC power plant development and operation has been reported by Webb et al. (2005). This report also contains a benchmark case and the sensitivity studies which have been used to populate the HOQ and derived the NFPRs associated with each function. These NFPRs are the targets which need to be validated during the design process. Otherwise, the system will fail to perform its operational objective.

The conclusions from the QFD are the following:

(1) The non-functional performance requirements for each function are presented below:

  (1) Generate oscillation (F1): The capture efficiency shall be greater than 59% at the boundary of the system

  (2) Generate pressure difference (F2): The capture efficiency shall be greater than 42% at the free-surface

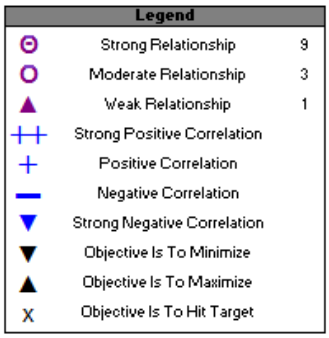

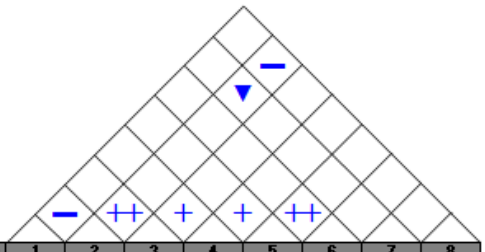

Row #	Max Relationship Value in Row	Relative Weight	Weight / Importance	Demanded Quality (a.k.a. "Customer Requirements" or "Whats") \ Quality Characteristics (a.k.a. "Functional Requirements" or "Hows")	Column #	1	2	3	4	5	6	7	8
				Direction of Improvement: Minimize (▼), Maximize (▲), or Target (x)		▲	▲	▲	▲	▲	▲	x	x
						GENERATE OSCILLATION	GENERATE PRESSURE DIFFERENCE	GENERATE TORQUE	TRANSFER TORQUE	GENERATE ELECRICAL POWER	CONTROL GENERATOR	PROVIDE MECHAMICAL INTEGRITY	LIMIT PRESSURE
1	9	6.8	4.0	SITE-SPECIFIC DESIGN		⊖	○	○	▲			⊖	⊖
2	9	13.6	8.0	CONVERSION EFFICIENCY IN REALISTIC CONDITONS		⊖	⊖	▲	▲	▲	▲		
3	9	15.3	9.0	LOW LIFECYCLE COST		○	○	▲	▲	▲	▲	⊖	
4	9	16.9	10.0	SURVAVILITY								⊖	○
5	9	8.5	5.0	INDUSTRIALISATION (MASS PRODUCTION)		○	○	○	○	▲	▲	⊖	▲
6	9	10.2	6.0	CONTROL OF EXPORT POWER						○	⊖		
7	9	8.5	5.0	NO UNDERWATER WORK REQUIRED		⊖							
8	3	5.1	3.0	LOW MAINTENANCE				○	○	○	○	▲	○
9	3	3.4	2.0	HOSTILE-ENVIRONMENT RESISTANT MATERIALS				▲	▲	▲	○	○	
10	9	11.9	7.0	SAFETY					○	○	⊖	⊖	○
				Target or Limit Value		Capture efficiency at lip > 53%	Capture efficiency > 42%	Instantaneous peak efficiency > 70%	Transmission efficiency > 90%	Electrical generator efficiency > 90%	Electrical grid standards and regulations	Storm limit load at location & cost reduction >50%	Endurance limit < 50%
				Difficulty (0=Easy to Accomplish, 10=Extremely		8	9	7	4	1	3	5	5
				Max Relationship Value in Column		9	9	3	3	3	9	9	9
				Weight / Importance		330.5	213.6	93.2	115.3	122.0	261.0	549.2	171.2
				Relative Weight		17.8	11.5	5.0	6.2	6.6	14.1	29.6	9.2

Fig. 5.5 House Of Quality: OWC power plant system

(3) Generate torque (F3): The instantaneous peak efficiency shall be greater than 70%

(4) Transfer torque (F4): The efficiency of the torque transfer shall be at least 90%

(5) Generate electricity (F5): The electricity generation efficiency shall be greater than 90%

(6) Control generator (F6): The electrical power shall meet the grid standards and regulations at the power plant location.

(7) Provide mechanical integrity (F7): Mechanical integrity of the plant shall be provided for the limit load representative case while reducing the cost by at least 50% compared current cost.

(8) Limit pressure (F8): The internal pressure shall be limited to ensure safe operation of the power plant during large power inputs and flooding.

(2) The relative importance of F7 outweighes the rest of the functions. Mechanical integrity of OWC power plants have already been proven by LIMPET and Pico demonstrators. The main challenge is the cost reduction which has been estimated around 20% to 50% to make the design viable in terms of life-cycle cost.

5.2.6 Scope of Design

The scope of the design and evaluation is wave-to-electrical power conversion as OWC power plants performance still do not meet the NFPRs. The mechanical integrity of the power plant is a well established technology for which the cost is the main challenge.

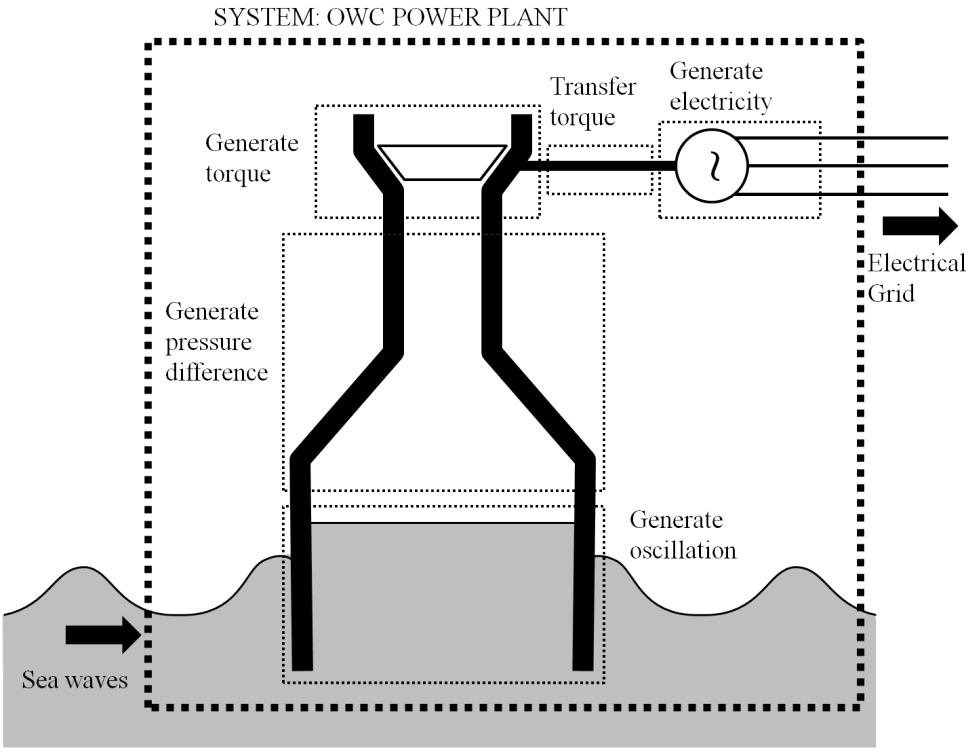

Fig. 5.6 System concept design

5.3 Design Evaluation

The design evaluation is performed via mathematical modelling. A model is an idealised representation of the reality but it provides the right system dynamics. Complex cause-effect relationships between inputs, outputs, and design parameters can be understood using the system model. The results from the model can be compared against the NFPR, and subsequently, validated to determine whether customer and stakeholders needs have been accomplished.

Besides the model accuracy, the key factor for successful implementation of design-oriented models is the timescales to produce an answer. If the model is too complex and the solving time is excessive, it has little value.

The vast majority of systems are complex entities, and therefore some means of dealing with this challenge are required. Two strategies are usually pursued:

(1) Sub-models: The system model is broken down into smaller models (sub-models), but the complexity is usually maintained at the expense of reducing the complexity of the interactions among them. Therefore, changes in sub-models do not dynamically affect the rest of sub-models.

(2) Reduced-order system model: There is only a model for the whole system. The interaction between physical and functional entities is addressed dynamically. These type of models usually require reducing the level of complexity. In order to maintain the accuracy, the simplified system model (reduced-order model) is trained or calibrated by higher-fidelity models or experimental data.

The second approach (reduced-order system modelling) has been used in this study which enables understanding complex interactions like those in the OWC power plant.

5.3.1 OWC Power Plant Reduced-Order System Model

This section presents the model for each function of the system, interface variables, and the limitations of each model as shown in Fig. 5.7.

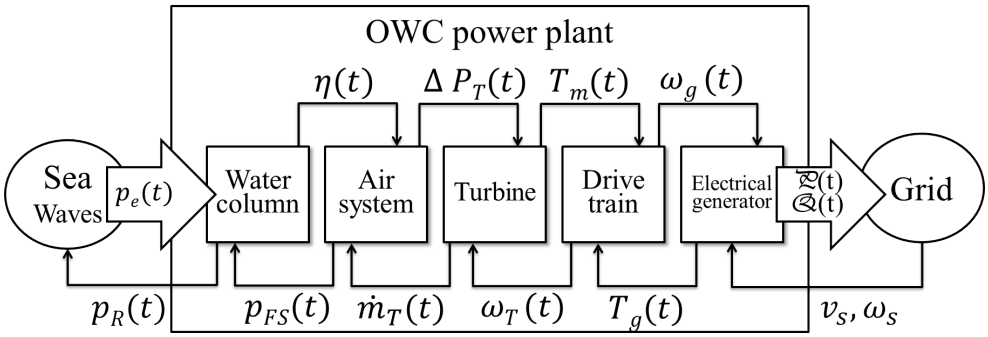

Fig. 5.7 Reduced-order system performance model

5.3.2 Water Column (F1)

The Water Column model has been developed, validated, and calibrated in Chapter 3 and it has been reproduced in this section for completeness. It comprises the Dynamic Equation (Eq. 5.1), and the correlations for added-mass coefficient (Eq. 5.2), non-linear radiation damping (Eq. 5.3), and radiation restoration coefficient (Eq. 5.4).

$$\left\{z_0+\eta(t)+\widetilde{M}_{r,h}\right\}\ddot{\eta}(t)+\widetilde{B}_{r,h}\dot{\eta}^2(t)+\left\{g+\rho_w\widetilde{C}_{r,h}\right\}\eta(t) = \frac{p_e(t)}{\rho_w S_w}+\frac{P_{\text{atm}}-P_{\text{FS}}(t)}{\rho_w} \tag{5.1}$$

$$\widetilde{M}_{r,h} = 2.6391\sqrt{S_w}-1.4981 \quad [\text{m}] \tag{5.2}$$

$$\begin{cases} \widetilde{B}^{+}_{r,h} = \left(\dfrac{R_L}{S_w} \sqrt{\dfrac{L_w}{g}} + 0.150 \right)^{-2.5} + 0.7 \quad \dot{\eta}(t) \geq 0 \quad [1] \\ \widetilde{B}^{-}_{r,h} = \left(\dfrac{R_L}{S_w} \sqrt{\dfrac{L_w}{g}} + 0.025 \right)^{-2.0} - 0.3 \quad \dot{\eta}(t) < 0 \quad [1] \end{cases} \tag{5.3}$$

$$\widetilde{C}_{r,h} = 0.0416 \bar{B}^2_{r,h} + 0.4787 \bar{B}_{r,h} \quad \left[\frac{\text{kg}}{\text{m}^2\text{s}^2} \right] \tag{5.4}$$

where $\overline{B}_{r,h} = \dfrac{1}{2} \left[\widetilde{B}^{+}_{r,h} + \widetilde{B}^{-}_{r,h} \right]$

Design Parameters

The OWC chamber design parameters have been identified in Chapter 3 and they are listed below:

(1) Submergence depth (L_w)

(2) Lip radius (L_w)

(3) Chamber breath (B_w)

(4) Chamber width (W_w)

Interfaces

The OWC chamber interfaces with the Sea Waves and the Air System.

(1) Inputs:

- Sea Waves to Water Column: Wave pressure $p_e(t)$
- Air System to Water Column: Free-surface pressure $p_{\text{FS}}(t)$

(2) Outputs:

- Water Column to Sea Waves: Radiation pressure $p_{\mathrm{r,B}}(t)$
- Water Column to Air System: Free-surface elevation $\eta(t)$

Limitations

The limitations of this Water Column model are:

(1) Single degree-of-freedom with approximated mode shape.

(2) Any three-dimensional effects are not captured.

(3) Friction loss has been neglected based on the assumption of hydrodynamically smooth wetted surfaces which might need to be reassessed.

(4) Diffracted wave field produced by the interaction of the incident wave with the submerged structures has not been considered.

(5) The interaction with the sea bed could change the correlations between the empirical parameters in Eq. 5.1 and the design parameters.

(6) This model does not account for the motion of the power plant which is floating in the water moored to the sea-bed. This could be achieved if the heave frequency of the floating structure is substantially different from the water column heave frequency.

5.3.3 Air System (F2)

Model

The air inside the chamber is compressed and decompressed by the effect of the water column elevation inside the caisson. The pressure difference between the air chamber and the atmosphere forces an alternating air stream throughout the Power Turbine characteristics.

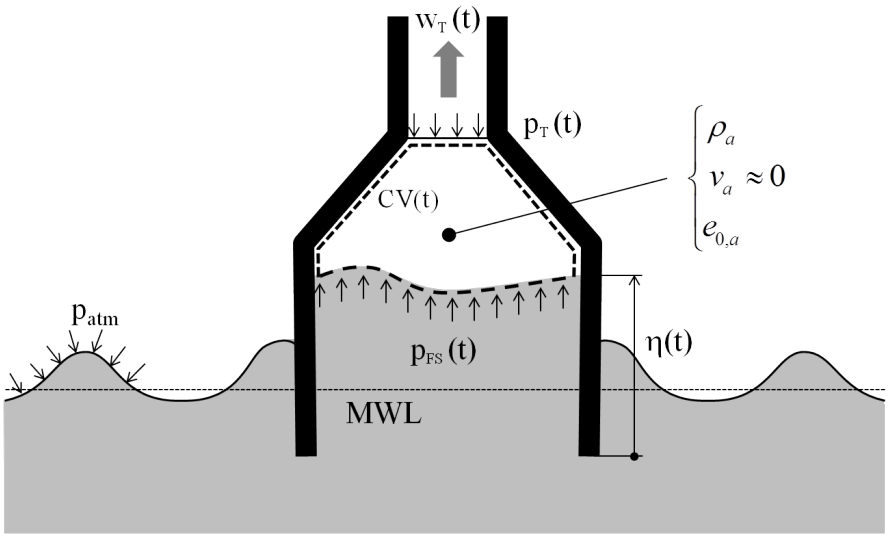

Fig. 5.8 Schematic of the control volume for Air System analysis

The Conservation Laws have been applied to a deformable control volume as depicted in Fig. 5.8. All flow variables are assumed uniform in the control volume except in the vicinity of the turbine location as depicted in Fig. 5.8. The integral Conservation Equations for compressible flow applied which can be found in Anderson (2004).

The initial pressure inside the chamber is estimated using the polytropic equation (see Eq. 5.5) at each instant. The polytropic index allows non-isentropic compressions or expansions which are more representative of real processes.

$$
\begin{aligned}
p_a(t_i) &= p_a(t_{i-1}) \left(\frac{V_a(t_{i-1})}{V_a(t_i)} \right)^n \\
\rho(t_i) &= \rho_a(t_{i-1}) \frac{V_a(t_{i-1})}{V_a(t_i)} \\
T_a(t_i) &= \frac{p_a(t_i)}{R_g \rho_a(t_i)}
\end{aligned}
\tag{5.5}
$$

The variables in the Mass Conservation (Eq. 5.6) and the Energy Conservation (Eq. 5.9) are initialised using the values calculated using Eq. 5.5. The compressibility effect plays an important role in the behaviour of the Air System as described in Chapter 2.

$$
\frac{\mathrm{D}}{\mathrm{D}t} \int_{CV(t)} \rho_a \, \mathrm{d}V = \frac{\partial}{\partial t} \int_{CV(t)} \rho_a \, \mathrm{d}V + \oint_{CS(t)} \rho_a (\vec{w} \cdot \vec{n})(t) \, \mathrm{d}S = 0 \tag{5.6}
$$

which is integrated in the control volume $V_{CV}(t)$ shown in Fig. 5.8.

$$
\begin{aligned}
V_{CV}(t) \frac{\partial \rho_a(t)}{\partial t} + \rho_a \frac{\partial V_{CV}(t)}{\partial t} + \dot{m}_{\mathrm{T}}(t) &= 0 \\
-\left(\frac{\partial \rho_a}{\partial t} \right) = \frac{\rho_a(t)}{V_{CV}(t)} \frac{\partial V_{CV}(t)}{\partial t} &+ \frac{\dot{m}_{\mathrm{T}}(t)}{V_{CV}(t)}
\end{aligned}
\tag{5.7}
$$

Energy Conservation Law (Eq. 5.9) is integrated in a similar fashion. Note that the gravity force is negligible for gases.

$$
\frac{\partial}{\partial t} \int_{CV(t)} (\rho_a e_{0,a}) \, \mathrm{d}V + \oint_{CS(t)} (\rho e_{0,a})(\vec{w}\vec{n}) \, \mathrm{d}S = \tag{5.8}
$$

$$
\dot{Q}_{CV} + \dot{W}_{\text{shaft}} + \dot{W}_{\text{viscous}} - \oint_{CS(t)} p(\vec{v}_d \cdot \vec{n}) \, \mathrm{d}S \tag{5.9}
$$

Integrating in the control volume $CV(t)$ and rearranging Eq. 5.9

$$\begin{aligned} V_{CV}\frac{\partial(\rho_a e_{0,a})}{\partial t}+(\rho_a e_{0,a})\frac{\partial V}{\partial t}+\dot{m}_{\mathrm{T}}\,e_{0,a}=p_{\mathrm{FS}}(t)A_{\mathrm{FS}}\frac{\partial\eta(t)}{\partial t} \quad \Longrightarrow \\ -\left(\frac{\partial(\rho_a e_{0,a})}{\partial t}\right)=\frac{(\rho_a e_{0,a})}{V_{CV}}\frac{\partial V_{CV}}{\partial t}-p_{\mathrm{FS}}(t)A_{\mathrm{FS}}\,\dot{\eta}(t)+\frac{\dot{m}_{\mathrm{T}}}{V_{CV}}e_{0,\mathrm{T}} \end{aligned} \tag{5.10}$$

Once the air density ρ_a and the internal total energy $(\rho_a e_{0,a})$ have been calculated from Eq. 5.7 and Eq. 5.10, the total pressure inside the air volume can be derived from the primitive variables assuming Perfect Gas behaviour (see Eq. 5.11). This calculation requires an iterative process as the mass flow throughout the turbine w_{T} varies with the pressure ratio.

$$p_{0,a}=R_g\frac{e_{0,a}}{c_v} \tag{5.11}$$

The pressure acting on the free surface is calculated from the total pressure inside the air volume and correcting the effect of the free-surface velocity $(\dot{\eta}(t))$ as shown in Eq. 5.12.

$$p_{\mathrm{FS}}(t)=p_{0,a}\left(1+\frac{\gamma-1}{2}M_{\mathrm{FS}}^2\right)^{-\frac{\gamma}{\gamma-1}} \tag{5.12}$$

Design parameters

The only Air System design parameter is:

(1) Air reservoir height (L_a)

The control volume (V_{CV}) in Eqs. 5.7 and 5.10, and the caisson air volume (V_a) are related by Eq. 5.13.

$$V_{CV}(t)=V_a+\Delta V_{CV}(t)=A_{\mathrm{FS}}\Big(L_a+\eta(t)\Big) \tag{5.13}$$

Interfaces

The OWC chamber interfaces with the Sea Waves and the Air System.

(1) Inputs:

- Water Column to Air System Free-surface elevation $\eta(t)$
- Power Turbine to Air System: Mass-flow through the Power Turbine $\dot{m}_{\mathrm{T}}(t)$

(2) Outputs:

- Air System to Power Turbine: Turbine inlet (exhalation) or exit (inhalation) total pressure $P_{0,T}(t)$ and total temperature $T_{0,T}(t)$
- Air System to Water Column: Free-surface pressure $p_{\mathrm{FS}}(t)$

Limitations

The limitations of the Air system model are:

(1) The model assumes negligible air velocity inside the air volume.

(2) The free-surface is not perturbed by the air jet during the inhalation phase.

(3) No aerodynamic loss is considered in this sub-system.

(4) Neither the air cavity resonances nor their effects are investigated.

5.3.4 Power Turbine (F3)

Model

The turbine is analysed utilising a simplified version of the Multi-Fidelity Design System described in Chapter 4 for which the URANS simulations have been removed. The turbine geometry is generated using the NISRE equation based on the design parameters which is analysed using a Throughflow Solver

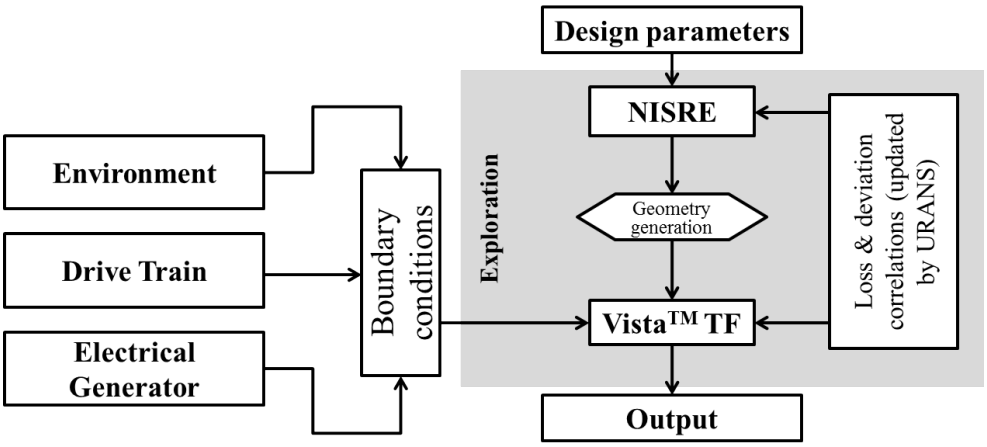

Fig. 5.9 Reduced-order turbine model

(Vista™ TF). The operation of the Power Turbine is considered quasi-steady which allows utilising the Radial Equilibrium Equation. Fig. 5.9 shows an schematic of the turbine geometry generation process and subsequent analysis. The calibration of the loss and deviation correlations has been performed in the uncoupled optimisation process performed in Chapter 4.

Design Parameters

The Power Turbine Design parameters were defined in Chapter 4:

(1) Loading coefficient ψ

(2) Flow coefficient ϕ

(3) Inlet axial Mach number at mid height M_1

(4) Chord-to-pitch ratio at the tip $(c/g)_{\text{tip}}$

(5) Rated power P_{T}

(6) Hub-to-tip ratio $D_{\text{hub}}/D_{\text{tip}}$

(7) Height-to-chord ratio h/c

(8) Rotor speed ratio N_A/N_B

(9) Vortex-law coefficients (3 per blade row) $A_1, B_1, C_1, A_2, B_2, C_2$

Interfaces

The OWC chamber interfaces with the Sea Waves and the Air System.

- Inputs:
  - Air System to Power Turbine: Turbine inlet (exhalation) or exit (inhalation) total pressure $P_{0,T}(t)$ and total temperature $T_{0,T}(t)$
  - Drive Train to Power Turbine: Turbine speed of rotation $\omega_{\mathrm{T}}(t)$
- Outputs:
  - Power Turbine to Air System: Mass-flow through the Power Turbine $\dot{m}_{\mathrm{T}}(t)$
  - Power Turbine to Drive Train: Drive Torque $T_m(t)$

Limitations

- The loss and deviation correlations have been calibrated utilising URANS simulations but the calibration might not be valid if the aerofoil geometry significantly changes.
- Flow hysteresis effects are not captured. However, shaft acceleration and deceleration will be captured by the model.

5.3.5 Drive Train (F4)

Model

The Drive Train comprises all the connecting mechanical elements between the Power Turbine and the Electrical Generator: gearbox, bearings, shafts, and the inertia elements which are connected by these (Power Turbine and Electrical Generator rotors).

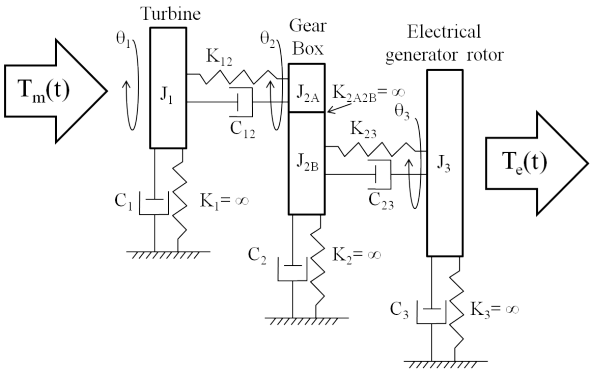

Fig. 5.10 Drive Train model schematic

The Torque Equilibrium governs the speed of rotation of the system. The electrical load of the generator sets the torque load which the Power Turbine has to drive. The connecting mechanical elements between the power turbine and the Electrical Generator have an influence on the system performance, especially during transients (start-up, stop, etc.).

Due to the nature of the alternating flow in the OWC power plant, the torque delivered by the power turbine is pulsating. Therefore, the Drive Train fulfils the non-trivial task of providing a uniform speed of rotation in the electrical generator shaft without suffering from significant torsional vibrations.

The shafts are modelled as flexible elements. The rotating parts of turbine, gearbox, and electrical generator are considered concentrated inertias. Mechanical loss accounts for the viscous friction in the bearings and shaft damping. Bearing and gear teeth stiffnesses are not studied in this model. Fig. 5.10 depicts the Drive Train model parameters and representation.

The Drive Train in Fig. 5.10 can be reduced to the turbine shaft as depicted in Fig. 5.11. Eq. 5.14 presents the dynamic equation which has been deduced from the idealised drive train reduced to the turbine shaft.

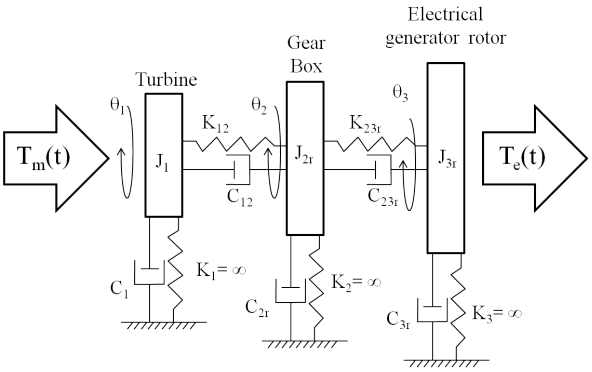

Fig. 5.11 Drive Train model schematic (reduced to the turbine shaft)

$$\begin{aligned}
\widetilde{J}_1\ddot{\theta}_1(t)+C_{12}\Big(\dot{\theta}_1(t)-\dot{\theta}_2(t)\Big)+C_1\dot{\theta}_1(t)+K_{12}\Big(\theta_1(t)-\theta_2(t)\Big)&=T_m(t)\\
\widetilde{J}_2\ddot{\theta}_2(t)+C_{12}\Big(\dot{\theta}_2(t)-\dot{\theta}_1(t)\Big)+\widetilde{C}_{23}\Big(\dot{\theta}_2(t)-\dot{\theta}_3(t)\Big)&\\
+\widetilde{C}_2\dot{\theta}_2(t)+K_{12}\Big(\theta_2(t)-\theta_1(t)\Big)+\widetilde{K}_{23}\Big(\theta_2(t)-\theta_3(t)\Big)&=0\\
\widetilde{J}_3\ddot{\theta}_3(t)+\widetilde{C}_{23}\Big(\dot{\theta}_3(t)-\dot{\theta}_2(t)\Big)+\widetilde{C}_3\dot{\theta}_3(t)+\widetilde{K}_{23}\Big(\theta_3(t)-\theta_2(t)\Big)&=\widetilde{T}_g(t)
\end{aligned} \tag{5.14}$$

where the equivalent inertias are defined by Eq. 5.15,

$$\begin{aligned}
\widetilde{J}_2&=J_{2A}+GR^2J_{2B}\\
\widetilde{J}_3&=GR^2J_3
\end{aligned} \tag{5.15}$$

the equivalent stiffness of the electrical generator shaft is calculated by Eq. 5.16,

$$\widetilde{K}_{23}\quad=GR^2K_{23} \tag{5.16}$$

the equivalent damping of the bearings on the electrical generator shaft and

the shaft damping are defined by Eq. 5.17,

$$\begin{aligned} \widetilde{C}_2 &= C_{2A} + GR^2 C_{2B} \\ \widetilde{C}_3 &= GR^2 C_3 \\ \widetilde{C}_{23} &= GR^2 C_{23} \end{aligned} \tag{5.17}$$

and the equivalent torque load is determined by Eq. 5.18.

$$\widetilde{T}_g = GR^2 T_g \tag{5.18}$$

This model not only allows studying the load transfer, but also analysing the torsional vibrations during start-up, shutdown, and continuous operation of the power plant. The torsional behaviour of the drive train plays a key role in the reliability of rotating machinery and a good design must avoid any coincidence of an excitation order with a natural frequency of the system (cf. Szenasi, 1993).

Design Parameters

The Drive Train design parameters are:

- Gearbox gear ratio (GR)
- Power Turbine shaft stiffness (K_{12})
- Electrical Generator shaft stiffness (K_{23})
- Power Turbine rotor inertia (J_1)
- Gearbox inertia (Power Turbine shaft side) (J_{2A})
- Gearbox inertia (Electrical Generator shaft side) (J_{2B})
- Electrical Generator rotor inertia (J_3)

Interfaces

The Drive Train interfaces with the Power Turbine and the Electrical Generator.

- Inputs:

  - Power Turbine to Drive Train: Drive Torque $T_m(t)$
  - Electrical Generator to Drive Train: Electro-magnetic torque load $T_g(t)$
- Outputs:
  - Drive Train to Power Turbine: Turbine speed of rotation $\omega_{\text{T}}(t)$
  - Drive Train to Electrical Generator: Electrical Generator speed of rotation $\omega_g(t)$

Limitations

The limitations of the Drive Train model are:

- The damping values for the bearings are assumed
- Bearings are and gear teeth are infinitely stiff
- Rotating masses are modelled as rigid disks
- Stress analyses cannot be carried out due to the model simplicity
- Bending stiffness of the shafts is not included
- Other degrees of freedom (axial, bending) have not been accounted for

5.3.6 Electrical Generator (F5) and Control System (F6)

Model

Fixed-pitch turbines require variable speed electrical generators in order to match the Power Turbine characteristics to the Water Column operation, and consequently, maximise the energy yield. The main drawback of the variable speed electrical systems is the cost increase of the Electrical Generator System. On the other hand, the whole system is much simpler as the electronic control enables mechanical simplicity: fixed pitch turbine, valveless, and no mechanical regulation. Variable speed operation is possible through power electronics which fully or partially decouple the electrical machine from the electricity grid.

Doubly-Fed Induction Generator (DFIG) has been the selected topology

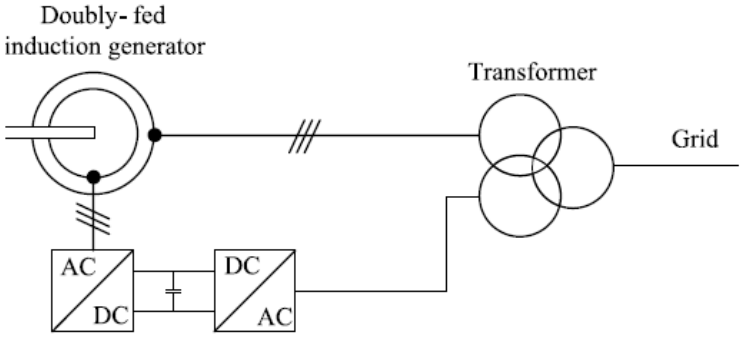

Fig. 5.12 Doubly-Fed Induction Generator (DFIG) scheme

in this study due to the following advantages: low cost, small size, wide range of rated powers (2,500 to 10,000 kVA), and the maturity achieved in wind energy power systems.

The DFIG is constructed using a wound rotor which is usually fed though slip rings. The rotor is connected to the electricity grid through a power converter which rectifies the rotor frequency to the grid frequency (50/60 Hz). The stator windings are directly connected to the electricity grid. Both rotor and stator inject a significant amount of real power to the grid. Figure 5.12 shows an schematic of the DFIG.

A system is required to control the real and reactive power via rotor flux control. Among all the control strategies the so-called *vector control* is the most popular as it enables independent regulation of real and reactive power.

Figure 5.13 depicts the equivalent electric circuit of the DFIG reduced to the stator. The usual model of electric machines follows Park (1929) for which the electromagnetic torque is expressed in the direct (d) and quadrature (q) axes. These electrical magnitudes can be easily converted to instantaneous phase values following *Park's Transformation*.

The DIFG electro-magnetic equations are expressed in the dq0 frame as

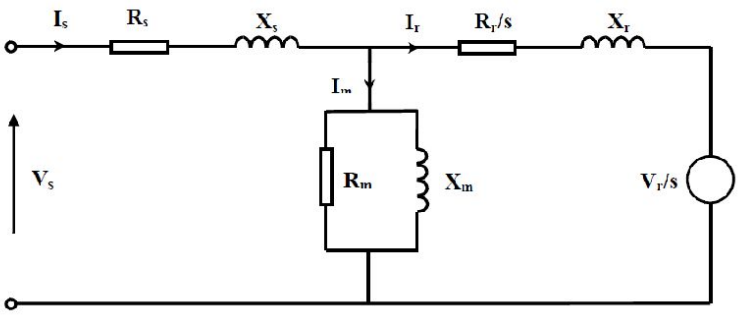

Fig. 5.13 Doubly-Fed Induction Generator (DFIG) equivalent electric circuit

follows (cf. Leonhard, 2001):

$$\begin{aligned}
\frac{\mathrm{d}\,i_{sd}}{\mathrm{d}t} &= \frac{1}{\mathscr{X}_s} v_{sd} - \frac{\mathscr{R}_s}{\mathscr{X}_s} i_{sd} - \frac{\mathscr{X}_\mu}{\mathscr{X}_s} \frac{\mathrm{d}\,i_{rd}}{\mathrm{d}t} + \omega_s \left(i_{sq} + \frac{\mathscr{X}_\mu}{\mathscr{X}_s} i_{rq} \right) \\
\frac{\mathrm{d}\,i_{sq}}{\mathrm{d}t} &= \frac{1}{\mathscr{X}_s} v_{sq} - \frac{\mathscr{R}_s}{\mathscr{X}_s} i_{sq} - \frac{\mathscr{X}_\mu}{\mathscr{X}_s} \frac{\mathrm{d}\,i_{rq}}{\mathrm{d}t} - \omega_s \left(i_{sd} + \frac{\mathscr{X}_\mu}{\mathscr{X}_s} i_{rd} \right) \\
\frac{\mathrm{d}\,i_{rd}}{\mathrm{d}t} &= \frac{1}{\mathscr{X}_r} v_{rd} - \frac{\mathscr{R}_r}{\mathscr{X}_r} i_{rd} - \frac{\mathscr{X}_\mu}{\mathscr{X}_r} \frac{\mathrm{d}\,i_{sd}}{\mathrm{d}t} + (\omega_s - \omega_e) \left(i_{rq} + \frac{\mathscr{X}_\mu}{\mathscr{X}_r} i_{sq} \right) \\
\frac{\mathrm{d}\,i_{rq}}{\mathrm{d}t} &= \frac{1}{\mathscr{X}_r} v_{rq} - \frac{\mathscr{R}_r}{\mathscr{X}_r} i_{rq} - \frac{\mathscr{X}_\mu}{\mathscr{X}_r} \frac{\mathrm{d}\,i_{sd}}{\mathrm{d}t} - (\omega_s - \omega_e) \left(i_{rq} + \frac{\mathscr{X}_\mu}{\mathscr{X}_r} i_{sd} \right)
\end{aligned} \tag{5.19}$$

where $\omega_e = p\,\omega_g$ being p the number of pole pairs of the electrical generator and ω_g the physical speed of rotation.

Equation 5.19 are restricted to symmetric three-phase machines. Eddy currents in the armature iron are neglected and each armature winding as sinusoidally distributed as per Park (1929).

The electromagnetic torque (Eq. 5.20) is fed back to the Drive Train and it can be derived from the rotor and stator currents:

$$T_g = \frac{3}{2} p\, \mathscr{X}_\mu \left(i_{sq}\, i_{rd} - i_{rq}\, i_{sd} \right) \tag{5.20}$$

The outputs from the Electrical Generator are the real power $\mathscr{P}$ (Eq. 5.21) and the reactive power $\mathscr{Q}$ (Eq. 5.22) injected into the electricity grid.

$$\mathscr{P} = \frac{3}{2}\left(v_{sd}\, i_{sd} + v_{sq}\, i_{sq} + v_{rd}\, i_{rd} + v_{rq}\, i_{rq}\right) \tag{5.21}$$

$$\mathscr{Q} = \frac{3}{2}\left(v_{sq}\, i_{sd} - v_{sd}\, i_{sq} + v_{rq}\, i_{rd} - v_{rd}\, i_{rq}\right) \tag{5.22}$$

Design Parameters

The Electrical Generator is defined by the following design parameters.

- Magnetising reactance ($\mathscr{X}_\mu$)
- Reactance of the rotor ($\mathscr{X}_s$)
- Electric resistance of the rotor ($\mathscr{R}_s$)
- Reactance of the stator ($\mathscr{X}_r$)
- Electric resistance of the stator ($\mathscr{R}_r$)
- Number of pole pairs (p)

Interfaces

The Electrical Generator Sub-System interfaces with the Power Turbine and the Electrical Grid.

- Inputs:
  - Drive Train to Electrical Generator: Electrical Generator speed of rotation $\omega_g(t)$
  - Electrical Grid to Electrical Generator: Stator voltage v_{sd}, v_{sq}
  - Electrical Grid to Electrical Generator: Stator voltage frequency ω_s (50/60 Hz)
- Outputs:

  - Electrical Generator to Electrical Grid: Active power injected to the electrical grid $\mathscr{P}$
  - Electrical Generator to Electrical Grid: Active power injected to the electrical grid $\mathscr{Q}$
  - Electrical Generator to Drive Train: Electro-magnetic torque $T_g(t)$

Limitations

The limitations of the Electrical Generator model are:

- The Electrical Grid is modelled as an infinite bus.
- The power electronics are considered ideal current sources.
- The electro-magnetic transients are not accounted for.
- No electrical fault or ride-through cases are analysed.

Chapter 6

Multidisciplinary System Design Optimisation

6.1 Introduction

This chapter will concentrate on the Multidisciplinary System Design Optimisation (MSDO). The optimisation of systems is a complex task as it involves many disciplines requiring multi-objective optimisation and many design parameters. All the relevant disciplines must be involved to avoid that the design is biased toward a single specialism. In doing so, side effects are generated and the other disciplines suffer substantial penalties, often leading to a substantial determined of the overall system attributes.

Stringent design timescales required efficient, advanced optimisation methods which can be used conjointly with the system model described in Chapter 5 to produce a design tool.

SOFT (Smart Optimisation For Turbomachinery) is an in-house code which has been developed by Rolls-Royce in collaboration with its University Technology Centres. This tool allows to integrate different analyses and provides five advanced optimisation libraries as following:

(1) Local and global optimisation library,

- Local methods: Dynamic Hill Climber (DHC), Modified Method of Feasible Direction (MFD), Sequential Quadratic Programming (NPQL), Successive Approximation Method (SAM), etc.
- Global methods: Simulated Annealing (SA), various Genetic Algorithms (GA), Tabu Search (TS), Monte Carlo (MC), Multi-Objective Genetic Algorithm, and Midrange Approximation Method, etc.

(2) A DoE library, e.g. Latin Hypercube, Taguchi and Lptau;

(3) A RSM library, e.g. Polynomial, RBF (Radial basis function) and Kriging, and Co-kriging (where adjoint gradients are used to produce a more accurate global RSM);

(4) ANOVA, where the interaction between design parameters as well as ranking and screening of the design parameters can be carried out;

(5) Design Space visualisation: Two-dimensional Slice contours, Parallel Coordinates, SOM (Self-Organising Maps), for multi-objective design spaces.

For more details on the SOFT libraries readers are referred to references Shahpar (2005) and Shahpar (2001). Various optimisation algorithms might be required depending on the available computation resources and the complexity of the optimisation problem.

In this Thesis, two of the methods available are in SOFT are selected based on the previous experience of the author: ARMOGA for the global search, and SQP for local search.

6.1.1 ARMOGA

The ARMOGA (Adaptive-Range Multi-Objective Genetic Algorithm) method available in SOFT is a GA search (non-deterministic zero-order method)

adapted to conduct a real multi-objective optimisation (Arakawa and Hagiwara, 1998), i.e. weighted sum approach of all the objectives is NOT used in this algorithm. This is important as the relative importance of each objective is not usually known a priory. ARMOGA will concentrate the search on the most promising area out of the whole design space based on population statistics.

The basic principle of GAs is the Darwinian natural selection, in which the fittest members of a species survive and produce offspring. Designs can be seen as individuals of a population for which their DNA is a vector ($\vec{x}$) containing the design parameters (genes). The GAs perform four basic operations: (1) Crossover and (2) Mutation.

(1) Crossover

This operator interchanges genes of the selected parents (${\vec{x}_1}^{i}, {\vec{x}_2}^{i}$) to produce two children (${\vec{x}_1}^{i+1}, {\vec{x}_2}^{i+1}$). Two parents are allowed to produce two children to maintain the population size. Eq. 6.1 shows the crossover operation.

$$\vec{x}_1{}^{i+1} = 0.5\left[\left(1+\beta_q\right)\vec{x}_1{}^{i}\right] + \left[\left(1-\beta_q\right)\vec{x}_2{}^{i}\right]$$

$$\vec{x}_2{}^{i+1} = 0.5\left[\left(1-\beta_q\right)\vec{x}_1{}^{i}\right] + \left[\left(1+\beta_q\right)\vec{x}_2{}^{i}\right]$$

$$\text{If} \quad u_1 \sim \mathscr{U}[0,1] < SBXrate \tag{6.1}$$

$$\beta_q = \begin{cases} \left(2u_1\right)^{\frac{1}{\eta_c+1}} & \text{if} \quad u_1 \leq 0.5 \\ \left(\dfrac{1}{2(1-u_1)}\right)^{\frac{1}{\eta_c+1}} & \text{if} \quad u_1 > 0.5 \end{cases}$$

else

$$\beta_q = 1.0$$

(2) Mutation

This operation alters the design vector by randomly disturbing its parameters (*genes*). Mutation expands the search space beyond the initial population and despite the elitism principles. High mutation rates perform a more random search which usually leads to slow convergence. However, low mutation rates might not able able to explore the whole design space. ARMOGA employs polynomial mutation as described by equation Eq. 6.2.

$$\vec{x}^{i+1}_{\text{mutation}} = \vec{x}^{i+1}_{\text{crossover}} + \left(\vec{x}_{\max} - \vec{x}_{\min}\right)\delta$$

If $u_2 \sim \mathscr{U}[0,1] < PMTrate$

$$\delta = \begin{cases} \left(2u_1\right)^{\frac{1}{\eta_m+1}} & \text{if} \quad u_1 \leq 0.5 \\ 1.0 - \left(2(1-u_1)\right)^{\frac{1}{\eta_m+1}} & \text{if} \quad u_1 > 0.5 \end{cases} \tag{6.2}$$

else

$$\delta = u_2\left(\vec{x}_{\max} - \vec{x}_{\min}\right) + \vec{x}_{\min}$$

6.1.2 SQP

Sequential Quadratic Programming is a gradient-based method (deterministic first-order method) which approximates the objective function as a quadratic function. The solution guarantees a globally optimal solution for the quadratic problem, however this might not be true for the original function. The SQP is a faster algorithm than ARMOGA, however its computational cost greatly increases with the number of design parameters. Gradient calculation is a onerous computational task, especially if this function cannot be analytically derived (which is the expected for the majority of real engineering problems).

6.2 Description of the problem

This section describes the optimisation strategy used in this thesis for MSDO. The problem definition is given by Eq. 6.3 which involves minimising M objective functions, $f_m(\vec{x})$. The solution vector contains n design parameters: $x = (x_1 \ldots x_n)^T$.

$$\begin{aligned}
&\text{Minimise:} && f_m(\vec{x}) && m = 1 \ldots M; \\
&\text{Subject to:} && g_j(\vec{x}) \geq 0 && j = 1 \ldots J; \\
& && h_k(\vec{x}) = 0 && k = 1 \ldots K; \\
& && \vec{x}_i{}^L \leq \vec{x}_i \leq \vec{x}_i{}^U && i = 1 \ldots n
\end{aligned} \tag{6.3}$$

The problem is subject to several constraints: (1) inequality constraints $g_j(\vec{x})$, (2) equality constraints $h_k(\vec{x})$, and (3) lower and upper bounds for each design parameter x_i. However, this formulation of the optimisation problem in which equality constraints are enforced, usually leads to unfeasible problems. An alternative approach has been proposed by Shahpar (2010) wherein this type of constraints are replaced by two-sided inequality constraints as shown in Eq. 6.4.

$$\begin{aligned}
&\text{Side constraints:} && h_k(\vec{x}) + \varepsilon \geq 0 && k = 1 \ldots K; \\
& && \varepsilon - h_k(\vec{x}) \geq 0 && k = 1 \ldots K
\end{aligned}$$

where ε is the allowed deviation from the target value (usually small).

Four real sea wave states published by Nielsen et al. (2010) have been chosen to perform the MSDO. The selected locations shown in Fig. 6.1 are described below:

(1) Bimep (Spain): Power 21 kW/m, depth 50-90 m

(2) Wave Hub (UK): Power 17 kW/m, depth 50-65 m

(3) Pilot Zone (Portugal): Power 25 kW/m, depth 50-90 m

(4) Galway Bay (Ireland): Power 2.4 kW/m, depth 20-25 m

Fig. 6.1 Selected locations for OWC optimisation

Sea wave spectra at those locations is derived from the joint probability diagrams provided by Nielsen et al. (2010). Figs. 6.2, 6.3, 6.4, and 6.5 depict the measured sea wave spectrum (red) and the fitted Jonswap spectrum (blue) at Bimep (Spain), Wave Hub (UK), Pilot Zone (Portugal), and Galway Bay (Ireland) respectively.

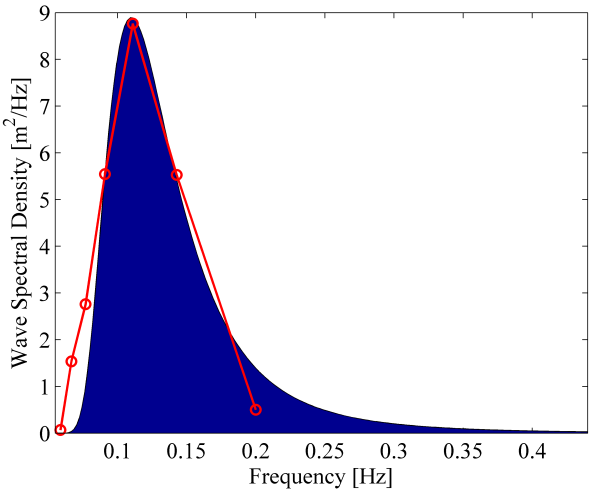

Fig. 6.2 Sea wave spectrum at Bimep (Spain): measured (red) and fitted Jonswap (blue)

Wave amplitude time series can be calculated using the Jonswap fitted spectra at each location as shown in Fig. 6.6 and Fig. 6.7.

6.3 Results

Several optimisation cases have been performed for each location described in the previous section. They have been carried out using SOFT which evaluates the objective function by running the Matlab®code which has been described in Chapter 5. It has been run on a computer with an Intel®Core™ i7 at 1.60 GHz and 4.0 GB of RAM. Each evaluation in the optimisation takes from few minutes to several minutes depending on the number of sub-systems involved

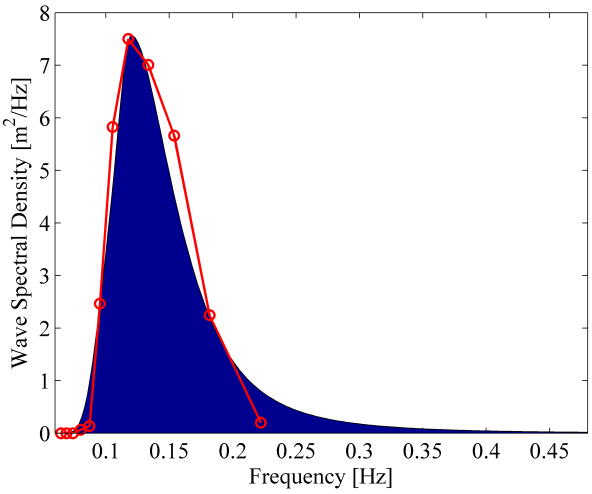

Fig. 6.3 Sea wave spectrum at Wave Hub (UK): measured (red) and fitted Jonswap (blue)

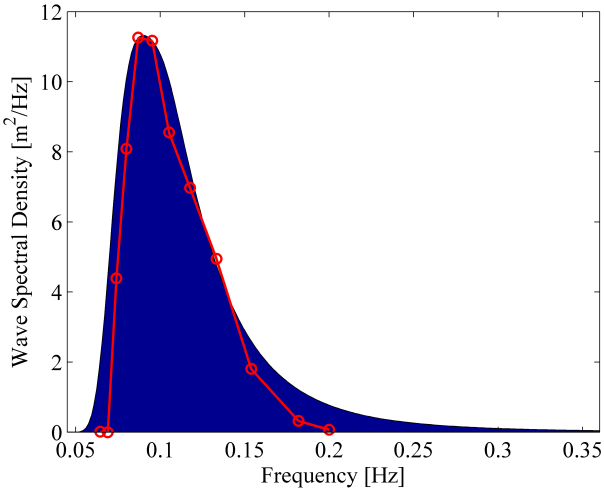

Fig. 6.4 Sea wave spectrum at Pilot Zone (Portugal): measured (red) and fitted Jonswap (blue)

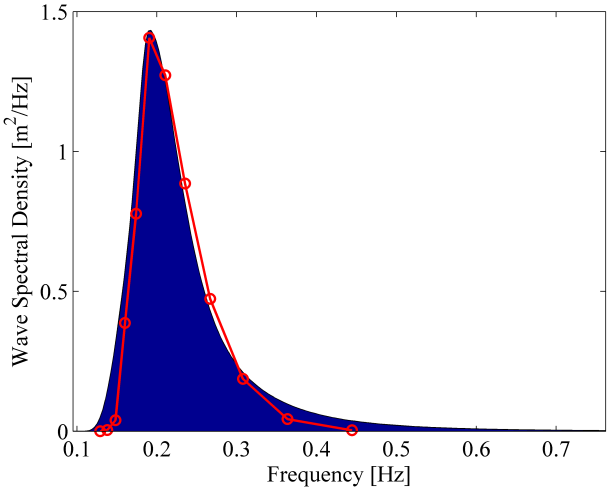

Fig. 6.5 Sea wave spectrum at Galway Bay (Ireland): measured (red) and fitted Jonswap (blue)

in the calculation and whether constant or variable speed is considered.

6.3.1 Case 1: Caisson sizing

The first step toward optimising the full system in this work would be to define a suitable caisson size based on the selected design parameters. The design vector contains four design variables which have been described in Chapter 3: (1) Submergence depth, L_w; (2) lip radius, R_L; (3) chamber breath, B_w; and (4) chamber width, W_w.

$$\vec{x}_{C1} = (L_w \quad R_L \quad B_w \quad W_w)^T \tag{6.5}$$

An amplification factor, Q, is defined as the ratio of free-surface elevation sample standard deviation, $s(\eta)$, to wave height sample standard deviation, $s(A_w)$, defined according to Eq. 6.6.

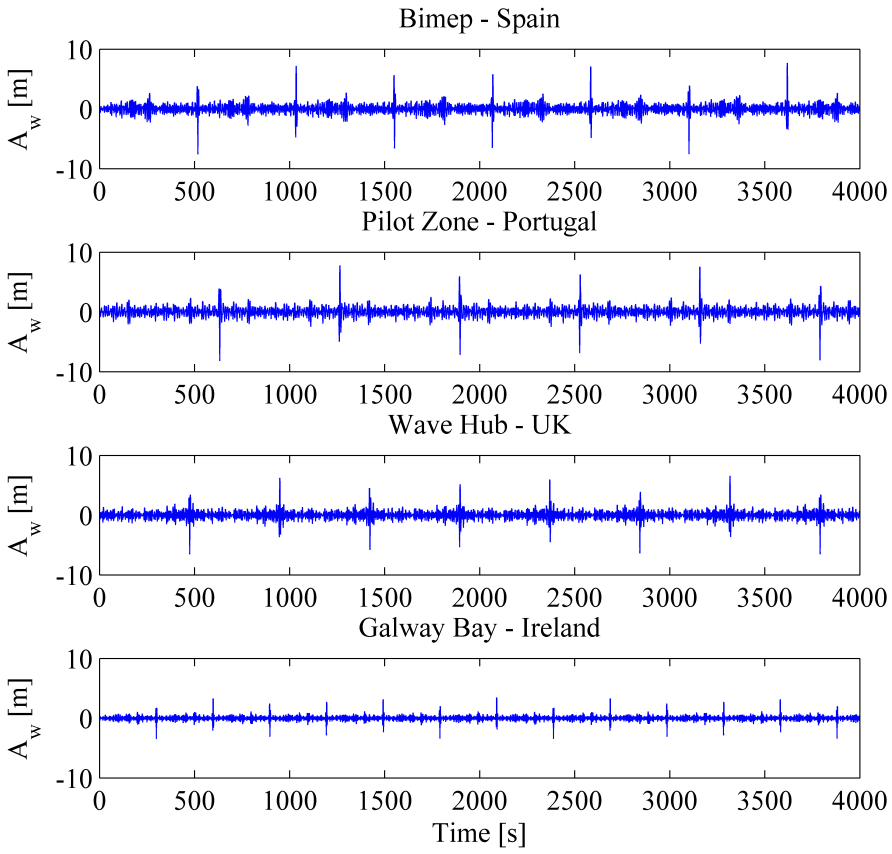

Fig. 6.6 Generated wave amplitude using fitted Jonswap spectra at various locations

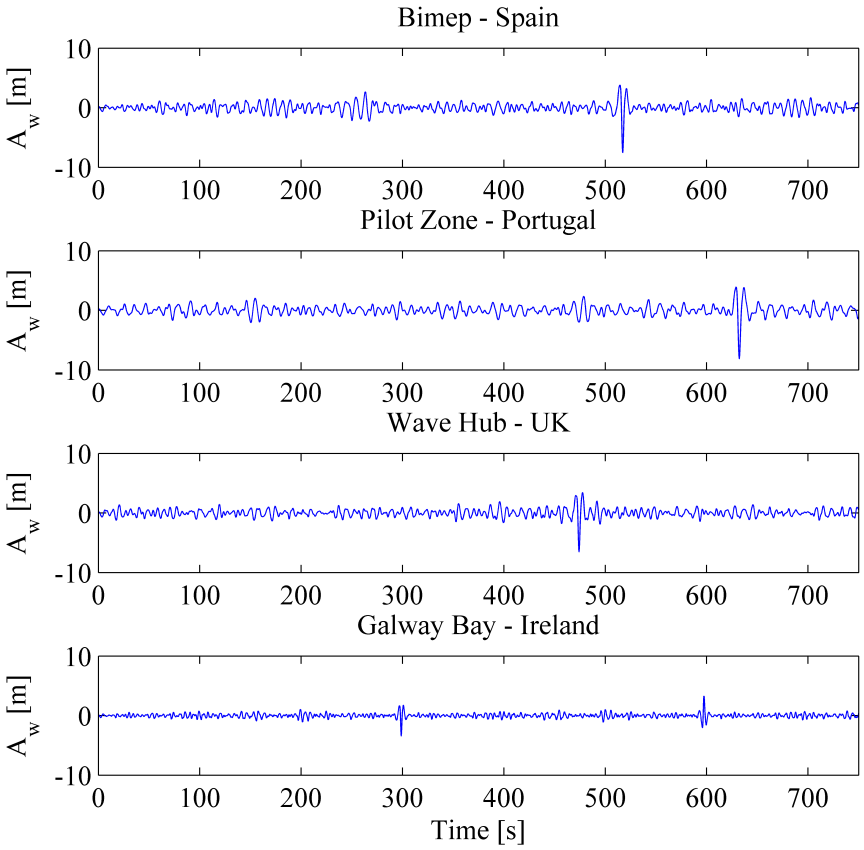

Fig. 6.7 Generated wave amplitude using fitted Jonswap spectra at various locations (reduced time span)

$$Q(\vec{x}) = \frac{s(\eta)(\vec{x})}{s(A_w)} \tag{6.6}$$

A good caisson design should amplify the wave amplitude, i.e. the amplification factor (Q) shall be maximised. However, the problem needs to be converted into a minimisation problem as defined by Eq. 6.3. The objective function has been defined as shown in Eq. 6.7.

$$f_{C1}(\vec{x}) = \frac{1}{\left(1 + Q(\vec{x})\right)^{5.0}} \tag{6.7}$$

For the optimisation process an inequality constraint has been defined to avoid exciting water column slosh modes (see Eq. 6.8). Mode contamination, i.e. forcing oscillations into a combination of modes, will reduce the available energy for the heave mode.

$$g_{C1}(\vec{x}) = f_{mn}(\vec{x}) - f_{\text{cut-off}} \geq 0 \quad \forall m,n \tag{6.8}$$

where

$$\begin{aligned} f_{mn}(\vec{x}) &= \frac{1}{2\pi}\sqrt{g\,k_{mn}\tanh\left(k_{mn}L_w\right)} \quad [\text{Hz}] \\ \text{where} \quad k_{mn}(\vec{x}) &= \pi\sqrt{\frac{4m^2}{W_w^2} + \frac{4n^2}{B_w^2}} \end{aligned} \tag{6.9}$$

and the cut-frequency $f_{\text{cut-off}}$ is defined as the frequency for which the sea wave energy spectral density becomes 5% of its peak value.

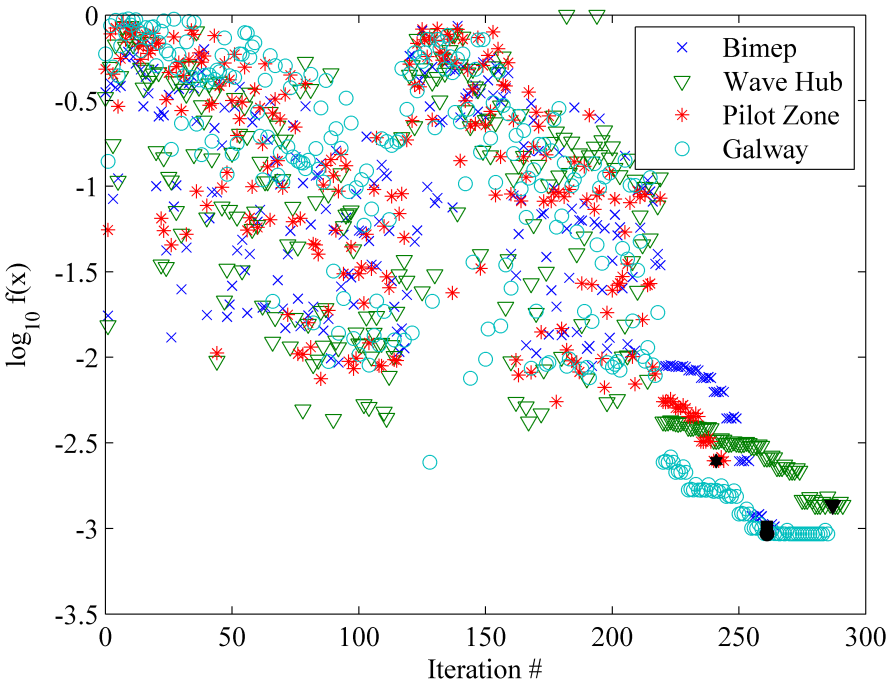

Fig. 6.8 Case1: Converge history of objective function $f(\vec{x})$

Fig. 6.8 depicts the evolution of the objective function $g_{C1}(\vec{x})$ in the optimisation process. The first 20 iterations correspond to 10 generations of 20 individuals using ARMOGA, whilst the remainders are calculated using the SQP algorithm. The optima for the four locations are shown as black filled symbols.

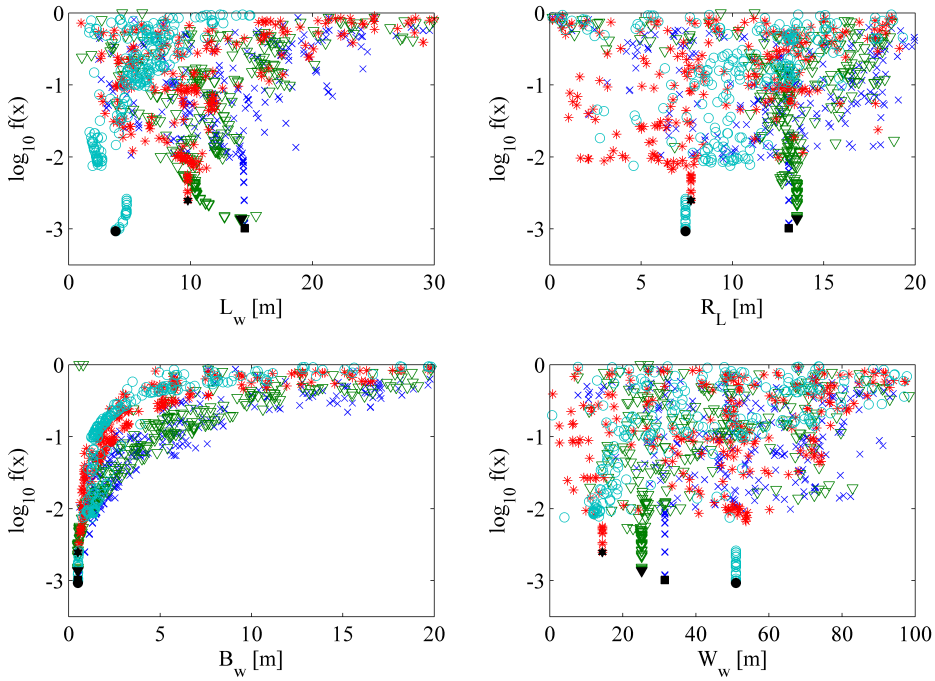

Fig. 6.9 Case1: Objective function $f(\vec{x})$ against design parameters L_w, R_L, B_w, and W_w

Fig. 6.9 depicts the evolution of the objective function against the four design parameters.

Fig. 6.10 shows a comparison of the ratio of heave mode natural mode calculated (see Eq. 3.60) to frequency for which the peak energy density occurs at each location. Note that the amplification factor drops as the maximum drifts away from the natural frequency. This is due to higher resonant frequency caused by increased damping as demonstrated in Chapter 3.

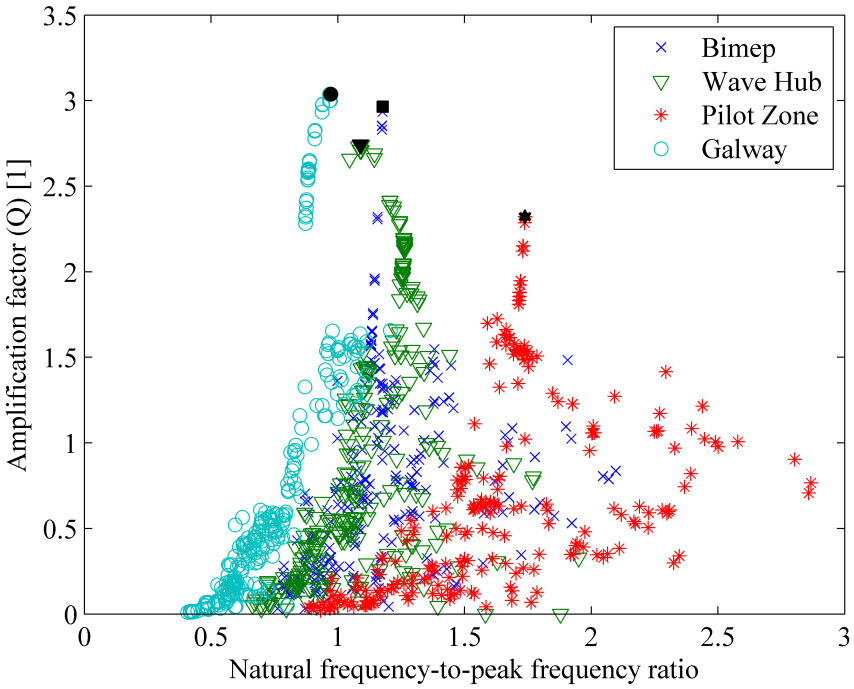

Fig. 6.10 Case1: Amplification ratio Q against natural frequency-to-peak excitation frequency ratio

Table 6.1 presents the optimal design vector at each location and the calculated amplification factor $Q(\vec{x})$.

Table 6.1 Case1: Optimal designs

Location	Bimep	Wave Hub	Pilot Zone	Galway Bay
L_w **[m]**	14.5	14.2	9.8	3.8
R_L **[m]**	13.1	13.5	7.7	7.4
B_w **[m]**	0.5	0.5	0.5	0.5
W_w **[m]**	31.5	25.2	14.4	51.0
f_n **[Hz]**	0.1294	0.130	0.156	0.243
f_m **[Hz]**	0.11	0.12	0.09	0.25
$f(\vec{x})$**[1]**	$1.02{\cdot}10^{-3}$	$1.36{\cdot}10^{-3}$	$2.47{\cdot}10^{-3}$	$9.31{\cdot}10^{-3}$
$Q(\vec{x})$ **[1]**	2.963783	2.741426	2.321391	3.038407

6.3.2 Case 2: Turbine sizing

The objective of this case is to optimise Sub-System 1 (water column, air system, and power turbine) when the power turbine operates at constant speed of rotation. The design vector contains the following parameters: (1) Submergence depth, L_w; (2) lip radius, R_L; (3) chamber breath, B_w; (4) chamber width, W_w; (5) air reservoir height, L_a; (6) turbine tip diameter, D_t; and (7) mechanical turbine speed, N.

$$\vec{x}_{C2} = (L_w \quad R_L \quad B_w \quad W_w \quad L_a \quad D_t \quad N)^T \tag{6.10}$$

In this case, the turbine is scaled based on the optimised design presented in Chapter 4, i.e. the bladings are not altered.

The Sub-System 1 efficiency has been defined as the ratio of average energy entering the system boundary to average energy extracted by the turbine

for a sufficient time series derived from the sea spectra presented in the previous sections.

$$\xi_{SS1}(\vec{x}) = \frac{\langle E_{\mathrm{T}} \rangle}{\langle E_{\mathrm{in}} \rangle} = \frac{\frac{1}{\Delta t}\int E_{\mathrm{T}}(t)\,\mathrm{d}t}{\frac{1}{\Delta t}\int E_{\mathrm{in}}(t)\,\mathrm{d}t} \tag{6.11}$$

In order to understand the contribution of each component to the subsystem efficiency, it can be split into two component efficiencies (see Eq. 6.12: (1) capture efficiency, ξ_{C}, and (2) turbine efficiency, ξ_{T}.

$$\xi_{\mathrm{SS1}}(\vec{x}) = \xi_{\mathrm{C}}(\vec{x})\ \xi_{\mathrm{T}}(\vec{x}) = \frac{\langle E_{\mathrm{T}} \rangle}{\langle E_{\mathrm{air}} \rangle} \quad \frac{\langle E_{\mathrm{air}} \rangle}{\langle E_{\mathrm{in}} \rangle} \tag{6.12}$$

where

$$\xi_{C}(\vec{x}) = \frac{\langle E_{\mathrm{air}} \rangle}{\langle E_{\mathrm{in}} \rangle} = \frac{\frac{1}{\Delta t}\int p_{\mathrm{FS}}(t)\dot{\eta}(t)B_w W_w\,\mathrm{d}t}{\frac{1}{\Delta t}\int \Big(p_e(t) + \rho_w g \eta(t)\Big)\dot{\eta}(t)\,\mathrm{d}t} \tag{6.13}$$

and

$$\xi_{T}(\vec{x}) = \frac{\langle E_{\mathrm{T}} \rangle}{\langle E_{\mathrm{air}} \rangle} = \frac{\frac{1}{\Delta t}\int T_{\mathrm{T}}(t)\omega_{\mathrm{T}}(t)\,\mathrm{d}t}{\frac{1}{\Delta t}\int p_{\mathrm{FS}}(t)\dot{\eta}(t)B_w W_w\,\mathrm{d}t} \tag{6.14}$$

Multi-objective optimisation has been performed on the functions shown in Eq. 6.20, which again are minimised.

$$f_{C2,1}(\vec{x}) = \frac{1}{\left(1+\xi_C(\vec{x})\right)^{5.0}} \tag{6.15}$$

$$f_{C2,2}(\vec{x}) = \frac{1}{\left(1+\xi_T(\vec{x})\right)^{5.0}} \tag{6.16}$$

The same inequality constraint as the previous case has been imposed to avoid water column slosh modes excitation (see Eq. 6.17).

$$g_{C2}(\vec{x}) = f_{mn}(\vec{x}) - f_{\text{cut-off}} \geq 0 \quad \forall m,n \tag{6.17}$$

The same optimisation strategy as in Case 1 has been taken. Fig. **??** depicts the evolution of the objective function $g_{C2}(\vec{x})$ in the optimisation process. ARMOGA has been utilised to compute the first XXX iterations followed by SQP optimisation. Unfeasible solutions are shown in red, feasible individuals in green, and the optimum in blue.

Fig. **??** shows the pareto front of the two objective functions.

Table **??** presents the optimal design vector at each location and the calculated efficiencies efficiency xi_{SS1}.

6.3.3 Case 3: Turbine design

This case involves a much larger number of design parameters. The bladings of the Vane-Less Contra-Rotating Turbine are also designed. However, constant rotational speed is enforced. The design vector contains the following parameters: (1) Submergence depth, L_w; (2) lip radius, R_L; (3) chamber breath, B_w; (4) chamber width, W_w; (5) air reservoir height, L_a, (6) inlet loading coefficient ψ, (7) inlet flow coefficient, ϕ, (7) mid-span inlet Mach num-

ber, M_1, (8) chord-to-pitch ratio at the tip, $(c/g)_{\text{tip}}$; (9) turbine rated power, P_{T}; (10) blade hub-to-tip ratio, $D_{\text{hub}}/D_{\text{tip}}$; (11-16) vortex law coefficients, $A_1, B_1, C_1, A_2, B_2, C_2$.

$$\begin{aligned}\vec{x}_{C3} = (&L_w \quad R_L \quad B_w \quad W_w \quad L_a \quad \psi \quad \phi \quad M_1 \quad (c/g)_{\text{tip}} \quad P_{\text{T}} \\ &D_{\text{hub}}/D_{\text{tip}} \quad A_1 \quad B_1 \quad C_1 \quad A_2 \quad B_2 \quad C_2)^T\end{aligned} \tag{6.18}$$

$$f_{C3,1}(\vec{x}) = \frac{1}{\left(1+\xi_C(\vec{x})\right)^{5.0}} \tag{6.19}$$

$$f_{C3,2}(\vec{x}) = \frac{1}{\left(1+\xi_T(\vec{x})\right)^{5.0}} \tag{6.20}$$

Several constraints have been imposed to: (1) avoid water column slosh modes excitation, (2) starting torque, (3) ETC ETC ETC ETC (see Eq. 6.21).

$$g_{C3,1}(\vec{x}) = f_{mn}(\vec{x}) - f_{\text{cut-off}} \geq 0 \quad \forall m,n \tag{6.21}$$

The same optimisation strategy as in Case 1 and 2 has been taken. Fig. **??** depicts the evolution of the objective function $g_{C2}(\vec{x})$ in the optimisation process. ARMOGA has been utilised to compute the first XXX iterations followed by SQP optimisation. Unfeasible solutions are shown in red, feasible individuals in green, and the optimum in blue.

Fig. **??** shows the pareto front of the two objective functions.

Table **??** presents the optimal design vector at each location and the calculated efficiencies efficiency xi_{SS1}.

Chapter 7

Conclusions and perspectives

7.1 Conclusions

This thesis has presented a holistic approach to Multidisciplinary Design System Optimisation of Oscillating Water Column Power Plants. A nonlinear stochastic approach has been taken, and a novel Vane-Less Contra-Rotating Turbine has been design using a Multi-Fidelity Design System.

Detailed literature and previous art have been presented in Chapter 2. Vast research has been performed on the early OWC design usually referred as hydro-pneumatic wave engines. Water column and system modelling techniques have been described. A rigorous survey on turbine architectures used for OWC power plants in which benefits and pitfalls have been ascertained. Concluding remarks have been made on the optimisation work available in the open literature, both manual and automated optimisation. As a result of this study, several shortfalls were identified which have been addressed in the subsequent chapters of the thesis:

(1) A nonlinear model for water column forced response was required for which caisson design parameters could be related to the performance. Most of the models presented in the literature are linear or do not in-

clude a comprehensive input of design parameters.

(2) Water column energy loss has been demonstrated to be large and could be reduced by geometric feature which need to be included in the design.

(3) A new turbine architecture which suits the OWC power plant elicited requirements. The Wells-type turbines lack of operating range, whilst the impulse-type turbines have an aerodynamic efficiency deficit.

(4) A multi-fidelity turbine design system which could be used for Multidisciplinary Design Optimisation on the selected turbine architecture.

(5) A computationally efficiency nonlinear system model, which allows to investigate and optimise power plant operation under stochastic wave conditions was required. This model needs to comprise all the design parameters relevant for system definition and explore major design constraints.

(6) Define a suitable system optimisation problem: representative wave input, system design parameters, objective function, and constraints.

(7) Perform Multidisciplinary System Design Optimisation (MSDO) of an OWC power plant under representative wave conditions.

A nonlinear reduced-order model for forced response of water column has been developed, validated, and calibrated against higher-fidelity CFD method using ANSYS Fluent®. This method was derived using first principles and a collocation method. Sixteen different caisson geometries were generated using Optimised Latin Hypercube which were extensively analysed in 66 test cases. Correlations between the model coefficients (added mass, nonlinear radiation damping, viscous loss, and hydrodynamic restoration) and the design parameters were developed. This strategy allowed rapid and accurate

analysis of forced water column oscillations. The effect of nonlinear radiation damping was assessed which was demonstrated to be important at high amplitudes.

A novel axial Vane-Less Contra-Rotating Turbine (VLCRT) for OWC power off-take has been designed using an automated multi-fidelity framework and optimised via stochastic evolutionary algorithms. The design framework is integrated by a core tool based upon the Non-Isentropic Simple Radial Equilibrium (NISRE) equation which together with the radial equilibrium through-flow solver Vista™ TFare utilised to explore the design space. Unsteady Reynolds-Averaged Navier-Stokes (uRANS) simulations validate and exploit the resulting design from the previous design stage. The uRANS CFD together the sliding planes allowed for rotor-rotor interaction. The main features of the optimised VLCRT are: (1) efficient operation in bi-directional alternating flow conditions over a wide flow range, (2) reduced outlet flow swirl without the need for outlet vanes which cause additional loss and reduce the available pressure drop for the rotor to produce useful work, (3) very-low pressure ratio, and (4) maximum centrifugal steady stress below 25% of the yield strength of the selected material.

A Systems Engineering approach has been taken for system design and analysis. The Voice of the Customer has been translated into functional and non-functional performance requirements. Systems architecting based on system functionality and functional interface has been used to group components into sub-systems. A computationally efficient system model has been proposed which included all the components: water column, air system, power turbine, drive train, and electrical generator. This system model includes the developments of previous chapters (nonlinear oscillations and novel VLCRT turbine architecture). The solution strategy allows for efficient simulation of power plant performance under stochastic wave conditions.

Multidisciplinary Design System Optimisation problem has been defined based on the former requirements and models. Four location have been in-

vestigated. Four optimisation problems have been presented: (1) Caisson optimisation, (2) Turbine sizing, (3) Turbine optimisation, and (4) Full-System optimisation. The results from the simpler problems have been fed into the more complex problems to enable faster convergence. Optimum design for each location has been demonstrated to vary when considering component optima or system optima. Therefore, a collection of optimum components do not lead to an optimal system, and hence, full-system optimisation is required. Finally, optimal design have been calculated considering the measured sea wave spectrum at four different locations: (1) Bimep (Spain), (2) Wave Hub (UK), (3) Pilot Zone (Portugal), and (4) Galway Bay (Ireland).

7.2 Perspectives

This thesis has proposed a model-based Multi-Disciplinary System Design Optimisation. The analysis techiniques could be further improved if the following topics are addressed:

(1) Water Column:

- Include several mode shapes to predict water column oscillations which would allow off-resonant prediction The water column model presented in this thesis is only valid in the vicinity of the heave-mode resonance. It would enable including three-dimensional effects which are not currently capture.
- Recalculated model coefficient correlation with design parameters when considering substantially rough surfaces.
- Introduce a model for diffracted wave field produced by the interaction of the incident wave with the submerged structures. It can be easily include in the current model due to its modularity and integral approach. Interaction with sea bed might be required for swallow

- If OWC structure motion affects water column oscillations, it could be easily included as extra degrees of freedom in the equation of motion. However, the influence on the radiation terms could be complex and might require higher-order methods or experimental surveys.
- Tide effect shall be included in the analysis as the water column performance is degraded off-resonance. However, a variable length system could be implemented to greatly improve energy yield.

(2) Air System:

- No viscous loss were considered for this compoent. Including jet effects and turbulent dissipation inside the surge chamber could be included by calibrating the proposed component equations.
- Air cavity resonances could be investigated, specially if some benefit could be achieved from tuning those to the water-column head mode frequency.

(3) Power turbine: Detail mechanical design of the Power Turbine needs to be carried out. Thorough investigation of aeroelastic effects need to be investigated due to the flow separations present in the VLCRT presented in this thesis.

(4) Drive Train: System reliability depends upon the accurate characterisation of the mechanical attributes of this component. The following aspects need to be carefully investigated:

- Mechanical damping present in the system
- Bearings are and gear teeth are stiffness and strength
- Turbine rotor flexibility
- Stress analysis via sub-modelling
- Other degrees of freedom (axial, bending) could be included in the analysis enabling simple rotordynamic analyses

(5) Electric Generator:

- The electric grid has been considered as an infinity bus. The OWC power plant model could be coupled with a power system analysis code in order to investigate phenomena such as line fault cases, Low-Voltage Ride-Through, or Sub-Synchronous Resonance
- The power electronics were considered ideal current sources, however detail analysis of the control system must include control system transients which are required for component design and performance analysis

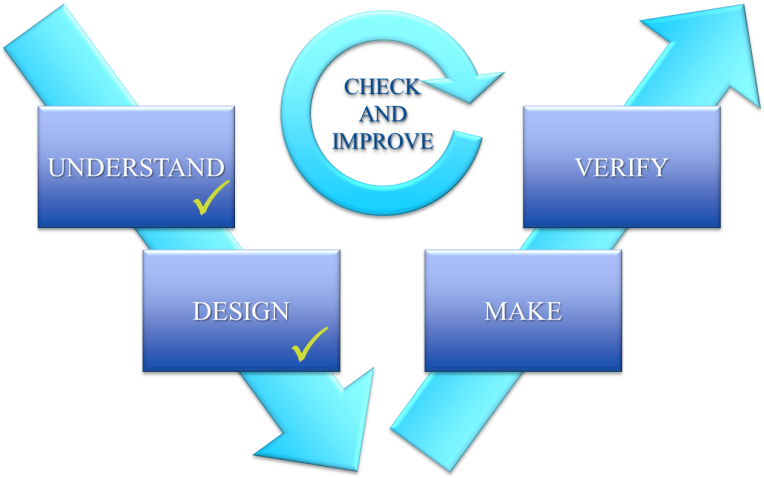

Fig. 7.1 Systems Engineering ‘V’

The system has been understood within the defined scope and suitable designs have been proposed. Fig. 7.1 shows the following steps in the system design. Potential failure modes and effects have to be identified so that mitigation or corrective strategies could be implemented to improve system safety and reliability. Once the system design has been shown to be fault-resistant to the Customer requirements, structured verifaction has to be carried out. This

process will ensure that all the requirements have been met either by analysis, lab testing, prototype tesiting, and finally power plant demonstration.

References

Abramson, H. N. (1966). The dynamic behavior of liquids in moving containers. nasa sp-106. *NASA Special Publication*, 106.

Ainley, D. and Mathieson, G. (1951). An examination of the flow and pressure losses in blade rows of axial-flow turbines. *British ARC Reports and Memoranda*, 2891.

Ambli, N. (1982). Wave energy power station. US Patent 4,341,959.

Amundarain, M., Alberdi, M., Garrido, A. J., and Garrido, I. (2011). Modeling and simulation of wave energy generation plants: Output power control. *Industrial Electronics, IEEE Transactions on*, 58(1):105–117.

Anderson, J. (2004). *Modern Compressible Flow with Historical Perspective*. Mc Graw-Hill Book Company, (New York), thrid edition.

Arakawa, M. and Hagiwara, I. (1998). Development of adaptive real range (arrange) genetic algorithms. *JSME International Journal Series C*, 41(4):969–977.

Babintsev, I. A. (1975). Apparatus for converting sea wave energy into electrical energy. US Patent 3,922,739.

Bang, D., Polinder, H., Shrestha, G., and Ferreira, J. A. (2008). Review of generator systems for direct-drive wind turbines. In *European Wind Energy Conference Exhibition, Belgium*.

Batchelor, G. K. (2000). *An introduction to fluid dynamics*. Cambridge university press.

Beckers, D. (1898). Tide-water air-compressor. US Patent 610,790.

Bissell, E. J. (1907). Wave-motor. US Patent 875,042.

Blanchard, B. S., Fabrycky, W. J., and Fabrycky, W. J. (1990). *Systems engineering and analysis*, volume 4. Prentice Hall Englewood Cliffs, New Jersey.

Boccotti, P. (2007). Comparison between a u-owc and a conventional owc. *Ocean Engineering*, 34(5):799–805.

Boccotti, P. (2012). Design of breakwater for conversion of wave energy into electrical energy. *Ocean engineering*, 51:106–118.

Booker, J., Mellor, P., Wrobel, R., and Drury, D. (2010). A compact, high efficiency contra-rotating generator suitable for wind turbines in the urban environment. *Renewable Energy*, 35(9):2027–2033.

Brendmo, A., Falnes, J., and Lillebekken, P. (1996). Linear modelling of oscillating water columns including viscous loss. *Applied ocean research*, 18(2):65–75.

Cai, R., Wu, W., and Fang, G. (1990). Basic analysis of counter-rotating turbines. In *ASME 1990 International Gas Turbine and Aeroengine Congress and Exposition*, pages V001T01A030–V001T01A030. American Society of Mechanical Engineers.

Casey, M. and Robinson, C. (2010). A new streamline curvature throughflow method for radial turbomachinery. *Journal of Turbomachinery*, 132(3):031021.

Chan, K. and Baird, M. (1974). Wall friction in oscillating liquid columns. *Chemical Engineering Science*, 29(10):2093–2099.

Corbett, J. A. D., Goalwin, D. S., and Weinberg, E. K. (1962). Power generator actuated by wave motion. US Patent 3,064,137.

Craig, H. and Cox, H. (1970). Performance estimation of axial flow turbines. *Proceedings of the Institution of Mechanical Engineers*, 185(1):407–424.

Curran, R. and Gato, L. (1997). The energy conversion performance of several types of wells turbine designs. *Proceedings of the Institution of Mechanical Engineers, Part A: Journal of Power and Energy*, 211(2):133–145.

Denantes, F. and Bilgen, E. (2006). Counter-rotating turbines for solar chimney power plants. *Renewable energy*, 31(12):1873–1891.

El Marjani, A., Ruiz, F. C., Rodriguez, M., and Santos, M. P. (2008). Numerical modelling in wave energy conversion systems. *Energy*, 33(8):1246–1253.

Evans, D. (1982). Wave-power absorption by systems of oscillating surface pressure distributions. *Journal of Fluid Mechanics*, 114:481–499.

Evans, D. and Porter, R. (1995). Hydrodynamic characteristics of an oscillating water column device. *Applied Ocean Research*, 17(3):155–164.

Faltinsen, O. M., Rognebakke, O. F., and Timokha, A. N. (2007). Two-dimensional resonant piston-like sloshing in a moonpool. *Journal of Fluid Mechanics*, 575:359–397.

Fluri, T. and Von Backström, T. (2008). Comparison of modelling approaches and layouts for solar chimney turbines. *Solar Energy*, 82(3):239–246.

Folley, M., Curran, R., and Whittaker, T. (2006). Comparison of limpet contra-rotating wells turbine with theoretical and model test predictions. *Ocean Engineering*, 33(8):1056–1069.

Gadonneix, P. (2010). 2010 survey of energy resources. Technical report, World Energy Council.

Gato, L. and Falcao, A. d. O. (1990). Performance of the wells turbine with a double row of guide vanes. *JSME international journal. Ser. 2, Fluids engineering, heat transfer, power, combustion, thermophysical properties*, 33(2):265–271.

Gonzalez, J. G., Pereiras, B., Castro, F., and Rodriguez, M. A. (2010). Numerical modelling in turbines for owc systems: Application to a radial impulse. In *ASME 2010 29th International Conference on Ocean, Offshore and Arctic Engineering*, pages 439–446. American Society of Mechanical Engineers.

Graham, E. and Rodriquez, A. (1951). The characteristics of fuel motion which affect airplane dynamics. Technical report, DTIC Document.

Griffith, A. A. (1949). Contrarotating axial flow high and low pressure turbine and compressor with bladed duct with turbine cooling. US Patent 2,477,798.

Haskins, C., editor (2011). *Systems Engineering Handbook: A guide for system life cycle processes and activities*. International Council of Systems Engineering.

Hasselmann, K., Barnett, T., Bouws, E., Carlson, H., Cartwright, D., Enke, K., Ewing, J., Gienapp, H., Hasselmann, D., Kruseman, P., et al. (1973). Measurements of wind-wave growth and swell decay during the joint north sea wave project (jonswap).

Hirsch, C. and Denton, J. (1981). Through-flow calculations in axial turbomachines. *AGARD-AR-175*.

Horlock, J. H. (1966). *Axial flow turbines*. Butterworth.

Inoue, M., Kaneko, K., Setoguchi, T., and Saruwatari, T. (1988). Studies on the wells turbine for wave power generator (turbine characteristics and design parameter for irregular wave). *JSME international journal. Ser. 2, Fluids engineering, heat transfer, power, combustion, thermophysical properties*, 31(4):676–682.

Jung, S. N., No, T.-S., and Ryu, K.-W. (2005). Aerodynamic performance prediction of a 30kw counter-rotating wind turbine system. *Renewable Energy*, 30(5):631–644.

Kaneko, K., Setoguchi, T., Raghunathan, S., et al. (1991). Self-rectifying turbines for wave energy conversion. In *The First International Offshore and Polar Engineering Conference*. International Society of Offshore and Polar Engineers.

Kanemoto, T. and Galal, A. M. (2006). Development of intelligent wind turbine generator with tandem wind rotors and double rotational armatures (1st report, superior operation of tandem wind rotors). *JSME International Journal Series B Fluids and Thermal Engineering*, 49(2):450–457.

Kasai, T., Usui, M., Nakamura, Y., Kanemoto, T., and Tanaka, D. (2010). On-cam operation of counter-rotating type hydroelectric unit. *Current Applied Physics*, 10(2):S133–S136.

Kearton, W. J. (1948). *Steam turbine theory and practice: a textbook for engineering students*. I. Pitman.

Knott, G. and Flower, J. (1980). Measurement of energy losses in oscillatory flow through a pipe exit. *Applied Ocean Research*, 2(4):155–164.

Knott, G. and Mackley, M. (1980). On eddy motions near plates and ducts, induced by water waves and periodic flows. *Philosophical Transactions of the Royal Society of London. Series A, Mathematical and Physical Sciences*, pages 599–623.

Larry, E. P. and Stein, D. J. (1923). Water-movement-power vessel. US Patent 1,448,029.

Leonhard, W. (2001). *Control of electrical drives*. Springer.

Louis, J. (1985). Axial flow contra-rotating turbines. In *ASME 1985 International Gas Turbine Conference and Exhibit*, pages V001T03A057–V001T03A057. American Society of Mechanical Engineers.

Maeda, H., Santhakumar, S., Setoguchi, T., Takao, M., Kinoue, Y., and Kaneko, K. (1999). Performance of an impulse turbine with fixed guide vanes for wave power conversion. *Renewable Energy*, 17(4):533–547.

March, A. and Willcox, K. (2010). Multifidelity modeling approaches for multidisciplinary design optimization. *VKI, lecture Series*, 7:93.

Masuda, Y. (1965). Ocean wave electric generator. US Patent 3,200,255.

McCormick, M., Rehak, J., and Williams, B. (1992). An experimental study of a bidirectional radial turbine for pneumatic wave energy conversion. In *OCEANS'92. Mastering the Oceans Through Technology. Proceedings.*, volume 2, pages 866–870. IEEE.

McCormick, M. and Surko, S. (1989). An experimental study of the performance of the counter-rotating wave energy conversion turbine. *Journal of Energy Resources Technology*, 111(3):167–173.

McCormick, M. E. (1974). Analysis of a wave energy conversion buoy. *Journal of Hydronautics*, 8(3):77–82.

McCormick, M. E. (1976). A modified linear analysis of a wave-energy conversion buoy. *Ocean Engineering*, 3(3):133–144.

McCormick, M. E. (1981). Counter-rotating wave energy conversion turbine. US Patent 4,271,668.

Modisette, J. L. (1981). Double acting turbine for converting wave energy of water to electrical power. US Patent 4,286,347.

Moody, G. W., Wilson, J. L., and Salter, S. H. (1980). Devices for extracting energy from wave power. US Patent 4,198,821.

Murakami, T., Kanemoto, T., Takano, G., and Kasahara, R. (2012). Numerical simulation in turbine mode of counter-rotating type axial flow pump (preparation of pump-turbine unit in cooperation with wind power unit).

In *ASME 2012 Fluids Engineering Division Summer Meeting*, pages 367–373. American Society of Mechanical Engineers.

Murakami, T., Kanemoto, T., Takano, G., and Kasahara, R. (2013). Numerical flow simulation in turbine mode of counter-rotating type pumping unit to cooperate with wind turbine. *Journal of Energy and Power Engineering*, 7(9):1770–7.

Muyeen, S., Tamura, J., and Murata, T. (2009). *Stability augmentation of a grid-connected wind farm*. Springer.

Newman, J. N. (1977). *Marine hydrodynamics*. MIT press.

Nielsen, K., Pontes, T., and Annex, I. (2010). Task 1.1 generic and site-related wave energy data. Technical report, Tech. Rep. T02-1.1, OES IA (September 2010).

Palme, A. (1920). Wave motion turbine. *Power*, 52(18):200–201.

Park, R. H. (1929). Two-reaction theory of synchronous machines generalized method of analysis-part i. *American Institute of Electrical Engineers, Transactions of the*, 48(3):716–727.

Paulson, B. J. (1949). Hydropneumatic power plant. US Patent 2,484,183.

Pereiras, B., Castro, F., el Marjani, A., and Rodríguez, M. A. (2011). Tip clearance effect on the flow pattern of a radial impulse turbine for wave energy conversion. *Journal of Turbomachinery*, 133(4):041019.

power conversion, G. (2014). Generators: 2,500 to 80,000 kva.

Raghunathan, S. (1995). The wells air turbine for wave energy conversion. *Progress in Aerospace Sciences*, 31(4):335–386.

Raghunathan, S. and Beattie, W. (1996). Aerodynamic performance of contra-rotating wells turbine for wave energy conversion. *Proceedings of the Institution of Mechanical Engineers, Part A: Journal of Power and Energy*, 210(6):431–447.

Raghunathan, S. and Tan, C. (1983). Performance of biplane wells turbine. *Journal of energy*, 7(6):741–742.

Richards, D. and Weiskopf, F. B. (1986). Studies with, and testing of the mccormick pneumatic wave energy turbine with some comments on pwecs systems. In *Utilization of Ocean Waves—Wave to Energy Conversion*, pages 80–102. ASCE.

Rolls-Royce plc and Atkins ltd (2010). Concept design of a very-low head dual generation tidal scheme for the severn estuary. Technical Report DNS159636.

Santhakumar, S., Jayashankar, V., Atmanand, M., Pathak, A., Ravindran, M., Setoguchi, T., Takao, M., Kaneko, K., et al. (1998). Performance of an impulse turbine based wave energy plant. In *The Eighth International Offshore and Polar Engineering Conference*. International Society of Offshore and Polar Engineers.

Sarmento, A. J. and Falcão, A. d. O. (1985). Wave generation by an oscillating surface-pressure and its application in wave-energy extraction. *Journal of Fluid Mechanics*, 150:467–485.

Sayma, A., Vahdati, M., Sbardella, L., and Imregun, M. (2000). Modeling of three-dimensional viscous compressible turbomachinery flows using unstructured hybrid grids. *AIAA Journal*, 38(6):945–954.

Schlaich, J., Bergermann, R., Schiel, W., and Weinrebe, G. (2005). Design of commercial solar updraft tower systems—utilization of solar induced convective flows for power generation. *Journal of Solar Energy Engineering*, 127(1):117–124.

Setoguchi, T., Kaneko, K., Maeda, H., Kim, T., and Inoue, M. (1988). Impulse turbine with self controlled blades for wave energy conversion. *Int. Jnl. Rotating Machinery*, 3(4):233–238.

Setoguchi, T., Kinoue, Y., Kim, T., Kaneko, K., and Inoue, M. (2003). Hysteretic characteristics of wells turbine for wave power conversion. *Renewable Energy*, 28(13):2113–2127.

Setoguchi, T., Santhakumar, S., Takao, M., Kim, T., and Kaneko, K. (2001). Effect of guide vane shape on the performance of a wells turbine. *Renewable energy*, 23(1):1–15.

Setoguchi, T., Santhakumar, S., Takao, M., Kim, T., and Kaneko, K. (2002). A performance study of a radial turbine for wave energy conversion. *Proceedings of the Institution of Mechanical Engineers, Part A: Journal of Power and Energy*, 216(1):15–22.

Setoguchi, T. and Takao, M. (2006). Current status of self rectifying air turbines for wave energy conversion. *Energy Conversion and Management*, 47(15):2382–2396.

Setoguchi, T., Takao, M., Kinoue, Y., Kaneko, K., Santhakumar, S., Inoue, M., et al. (1999). Study on an impulse turbine for wave energy conversion. In *The Ninth International Offshore and Polar Engineering Conference*. International Society of Offshore and Polar Engineers.

Shahpar, S. (2001). Soft: A new design and optimisation tool for turbomachinery. *Evolutionary Methods for Design, Optimisation and Control*.

Shahpar, S. (2002). Soft: A new design and optimisation tool for turbomachinery. *Evolutionary Methods for Design, Optimisation and Control*.

Shahpar, S. (2005). Sophy: An integrated cfd based automatic design optimisation system. *ISABE-2005-1086*, 93022.

Shahpar, S. (2010). High fidelity multi-stage design optimisation of multi-stage turbine blades using a mid-range approximation method. In *13th AIAA/ISSMO Multidisciplinary Analysis Optimization Conference, Fort Worth, TX, September*, pages 13–15.

Shahpar, S. and Lapworth, L. (2003). Padram: parametric design and rapid meshing system for turbomachinery optimisation. In *ASME turbo Expo, Atlanta, Georgia, GT 2003-38698*, pages 579–590. American Society of Mechanical Engineers.

Shishko, R. and Aster, R. (1995). Nasa systems engineering handbook. *NASA Special Publication*, 6105.

Stoker, J. J. (1957). *Water Waves: The Mathematical Theory With Applications*. Interscience Publishers Inc.

Stratford, B. and Sansome, G. (1962). *Theory and tunnel tests of rotor blades for supersonic turbines*. Citeseer.

Szenasi, F. R. (1993). Analysis of torsional vibrations in rotating machinery. In *Proceedings of the Turbomachinery Symposium*, volume 22, page 127. Gas Turbine Laboratories, Department of Mechanical Engineering, Texas A & M University.

Takao, M., Fujioka, Y., and Setoguchi, T. (2005). Effect of pitch-controlled guide vanes on the performance of a radial turbine for wave energy conversion. *Ocean engineering*, 32(17):2079–2087.

Takao, M., Setoguchi, T., Kaneko, K., Kim, T., Maeda, H., Inoue, M., et al. (2002a). Impulse turbine for wave power conversion with air flow rectification system. *International journal of offshore and polar engineering*, 12(02).

Takao, M., Setoguchi, T., Kaneko, K., Raghunathan, S., and Inoue, M. (2002b). Noise characteristics of turbines for wave power conversion. *Proceedings of the Institution of Mechanical Engineers, Part A: Journal of Power and Energy*, 216(3):223–228.

Thakker, A. and Dhanasekaran, T. (2004). Computed effects of tip clearance on performance of impulse turbine for wave energy conversion. *Renewable energy*, 29(4):529–547.

Thakker, A., Dhanasekaran, T., and Ryan, J. (2005). Experimental studies on effect of guide vane shape on performance of impulse turbine for wave energy conversion. *Renewable energy*, 30(15):2203–2219.

Thakker, A., Dhanasekaran, T., Takao, M., and Setoguchi, T. (2003). Effects of compressibility on the performance of a wave-energy conversion device with an impulse turbine using a numerical simulation technique. *International Journal of Rotating Machinery*, 9(6):443–450.

Thakker, A. and Elhemry, M. A. (2007). 3-d cfd analysis on effect of hub-to-tip ratio on performance of impulse turbine for wave energy conversion. *Thermal Science*, 11(4):157–170.

Thakker, A., Frawley, P., Khaleeq, H., Abugihalia, Y., Setoguchi, T., et al. (2001). Experimental and cfd analysis of 0.6 m impulse turbine with fixed guide vanes. In *The Eleventh International Offshore and Polar Engineering Conference*. International Society of Offshore and Polar Engineers.

Thiebaut, F., DOSullivan, P. K., Ceballos, S., López, J., Boake, C., Bard, J., Brinquete, N., Varandas, J., Gato, L., Alcorn, R., et al. (2011). Testing of a floating owc device with movable guide vane impulse turbine power take-off. In *Proceedings of the 9th European Wave and Tidal Energy Conference, Southampton, UK*.

Thomsen, J. J. (2003). *Vibrations and stability: advanced theory, analysis, and tools*. Springer.

Troester, E. (2009). New german grid codes for connecting pv systems to the medium voltage power grid. In *2nd International workshop on concentrating photovoltaic power plants: optical design, production, grid connection*, pages 9–10.

Tuch, C. C. (1918). Hydraulic air-compressor and motor. US Patent 1,267,936.

Ushiyama, I., Shimota, T., and Miura, Y. (1996). An experimental study of the two-staged wind turbines. *Renewable energy*, 9(1):909–912.

Verstraete, T. (2010). Introduction to optimization and multidisciplinary design. *VKI, lecture Series*, 7:93.

Vieira, M., Sarmento, A., and Reis, L. (2015). Failure analysis of the guide vanes of the pico wave power plant wells turbine. *Engineering Failure Analysis*.

Webb, I., Seaman, C., and Jackson, G. (2005). Marine energy challenge oscillating water column wave energy converter evaluation report. Technical report, The Carbon Trust.

Weber, J., Thomas, G., et al. (2001). An investigation into the importance of the air chamber design of an oscillating water column wave energy device. In *The Eleventh International Offshore and Polar Engineering Conference*. International Society of Offshore and Polar Engineers.

Wells, A. A. (1980). Rotary transducers. US Patent 4,221,538.

Wells, A. A. (1983). Wave energy apparatus. US Patent 4,383,413.

Wintucky, W. T. and Stewart, W. L. (1958). Analysis of two-stage counterrotating turbine efficiencies in terms of work and speed requirements.

Appendix A

Oscillating Water Column Reduced-Order Model Parameter Optimisation

A.1 Water Column Loss Model Calibration

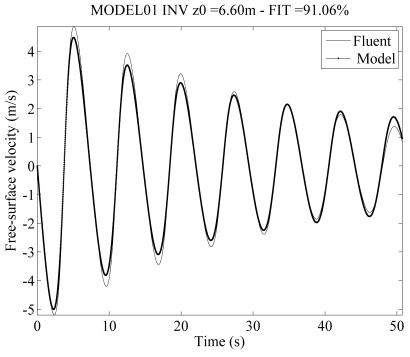

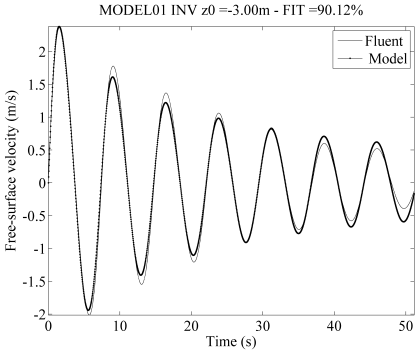

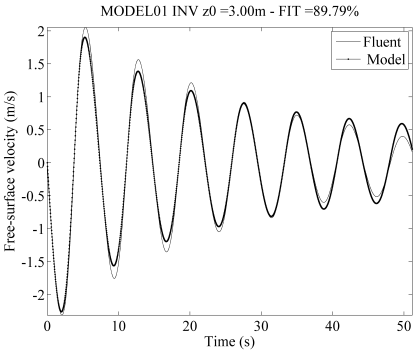
MODEL01 INV z0 =3.00m - FIT =89.79%
Fluent
Model
Free-surface velocity (m/s)
Time (s)

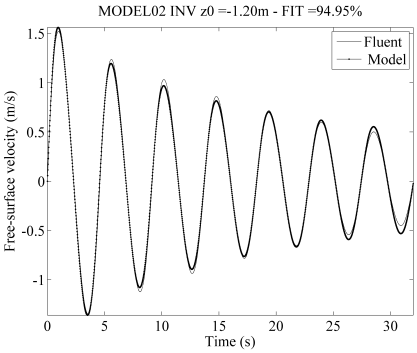
MODEL02 INV z0 =-1.20m - FIT =94.95%
Fluent
Model
Free-surface velocity (m/s)
Time (s)

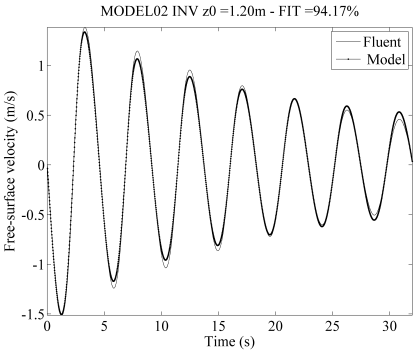
MODEL02 INV z0 =1.20m - FIT =94.17%
Fluent
Model
Free-surface velocity (m/s)
Time (s)

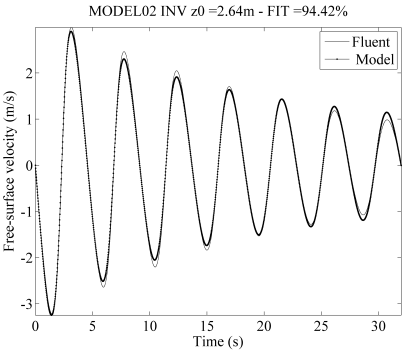
MODEL02 INV z0 =2.64m - FIT =94.42%
Fluent
Model
Free-surface velocity (m/s)
Time (s)

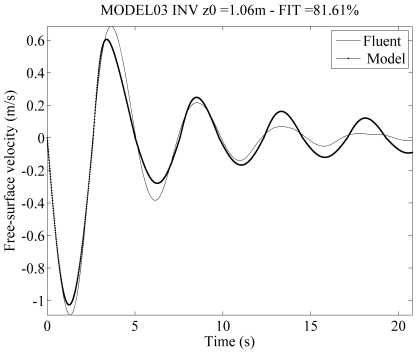
MODEL03 INV z0 =1.06m - FIT =81.61%
Fluent
Model
Free-surface velocity (m/s)
Time (s)

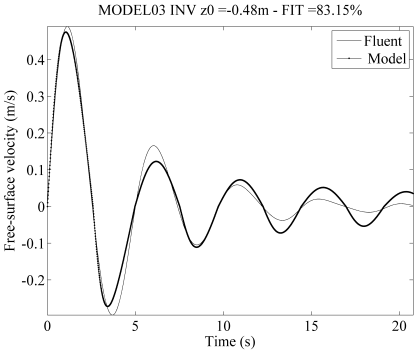
MODEL03 INV z0 =-0.48m - FIT =83.15%
Fluent
Model
Free-surface velocity (m/s)
Time (s)

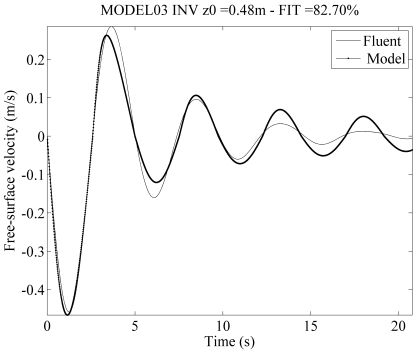
MODEL03 INV z0 =0.48m - FIT =82.70%
Fluent
Model
Free-surface velocity (m/s)
Time (s)

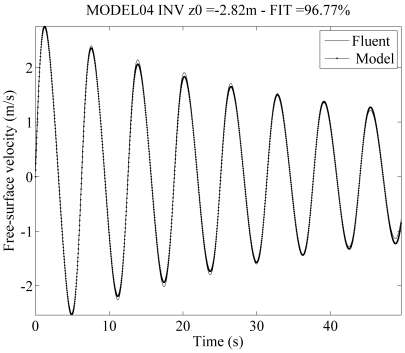
MODEL04 INV z0 =-2.82m - FIT =96.77%
Fluent
Model
Free-surface velocity (m/s)
Time (s)

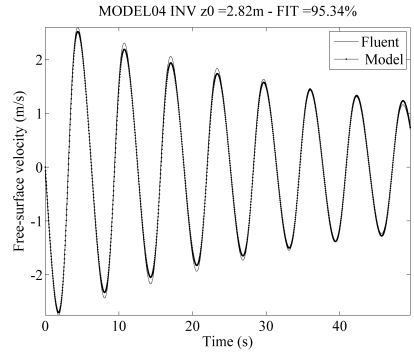
MODEL04 INV z0 =2.82m - FIT =95.34%
Fluent
Model
Free-surface velocity (m/s)
Time (s)

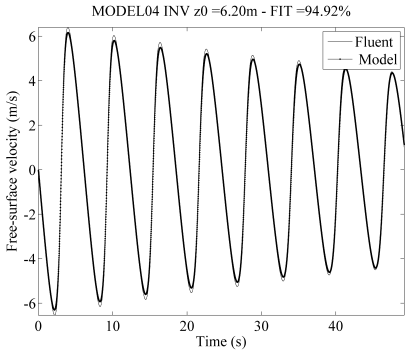
MODEL04 INV z0 =6.20m - FIT =94.92%
Fluent
Model
Free-surface velocity (m/s)
Time (s)

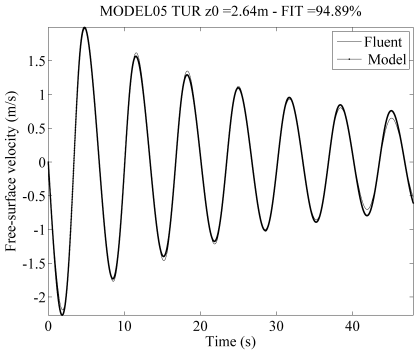
MODEL05 TUR z0 =2.64m - FIT =94.89%
Fluent
Model
Free-surface velocity (m/s)
Time (s)

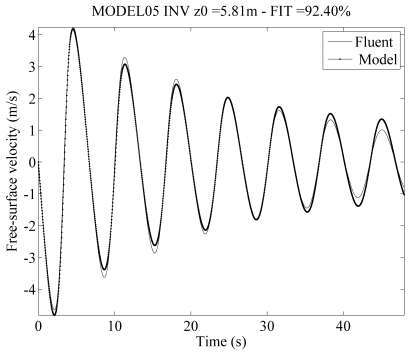
MODEL05 INV z0 =5.81m - FIT =92.40%
Fluent
Model
Free-surface velocity (m/s)
Time (s)

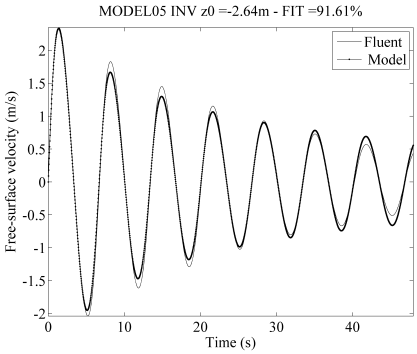
MODEL05 INV z0 =-2.64m - FIT =91.61%
Fluent
Model
Free-surface velocity (m/s)
Time (s)

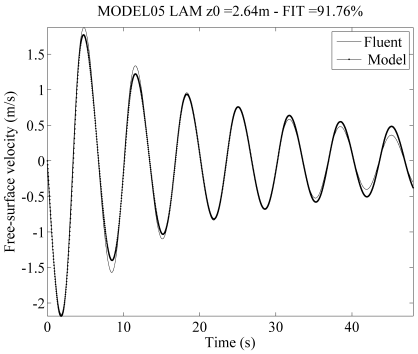
MODEL05 LAM z0 =2.64m - FIT =91.76%
Fluent
Model
Free-surface velocity (m/s)
Time (s)

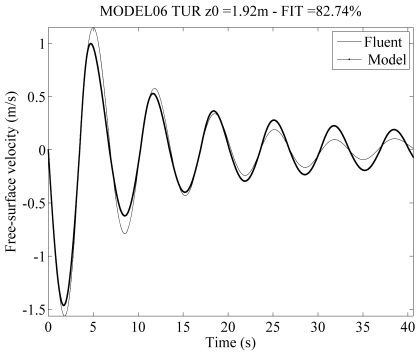
MODEL06 TUR z0 =1.92m - FIT =82.74%
Fluent
Model
Free-surface velocity (m/s)
Time (s)

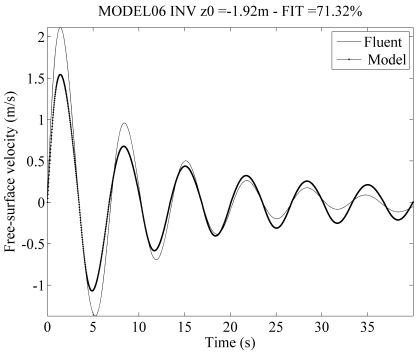
MODEL06 INV z0 =-1.92m - FIT =71.32%
Fluent
Model
Free-surface velocity (m/s)
Time (s)

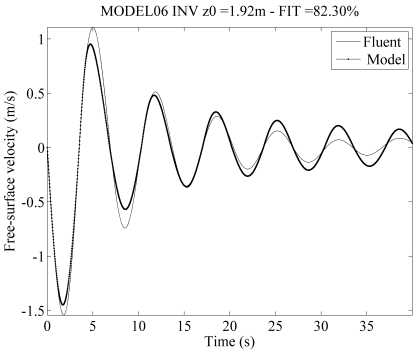
MODEL06 INV z0 =1.92m - FIT =82.30%
Fluent
Model
Free-surface velocity (m/s)
Time (s)

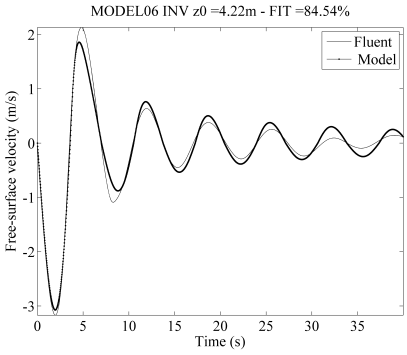
MODEL06 INV z0 =4.22m - FIT =84.54%
Fluent
Model
Free-surface velocity (m/s)
Time (s)

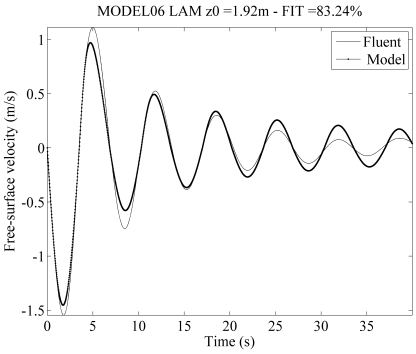
MODEL06 LAM z0 =1.92m - FIT =83.24%
Fluent
Model
Free-surface velocity (m/s)
Time (s)

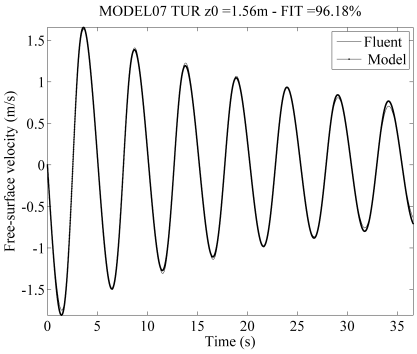
MODEL07 TUR z0 =1.56m - FIT =96.18%
Fluent
Model
Free-surface velocity (m/s)
Time (s)

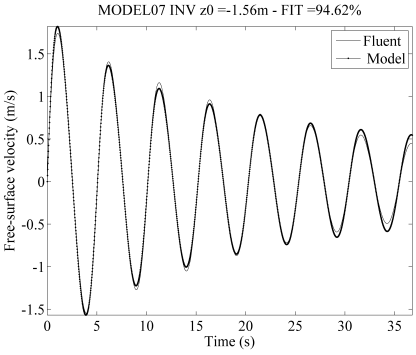
MODEL07 INV z0 =-1.56m - FIT =94.62%
Fluent
Model
Free-surface velocity (m/s)
Time (s)

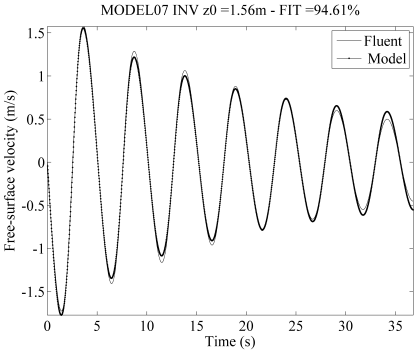
MODEL07 INV z0 =1.56m - FIT =94.61%
Fluent
Model
Free-surface velocity (m/s)
Time (s)

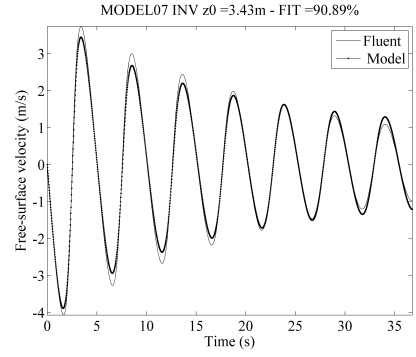
MODEL07 INV z0 =3.43m - FIT =90.89%
Fluent
Model
Free-surface velocity (m/s)
Time (s)

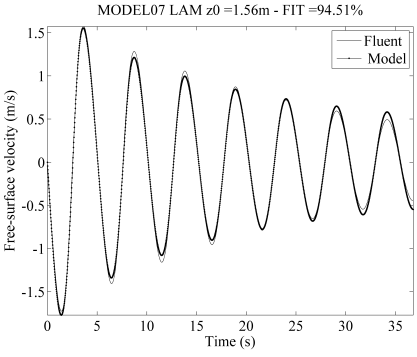
MODEL07 LAM z0 =1.56m - FIT =94.51%
Fluent
Model
Free-surface velocity (m/s)
Time (s)

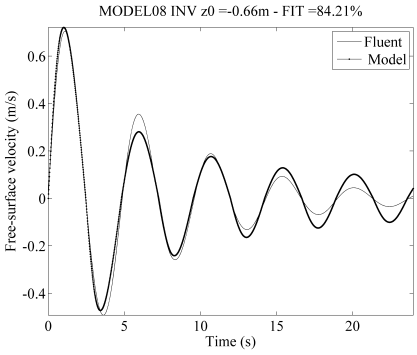
MODEL08 INV z0 =-0.66m - FIT =84.21%
Fluent
Model
Free-surface velocity (m/s)
Time (s)

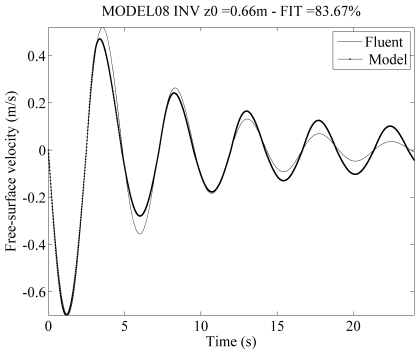
MODEL08 INV z0 =0.66m - FIT =83.67%
Fluent
Model
Free-surface velocity (m/s)
Time (s)

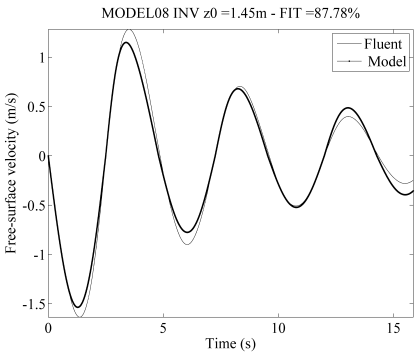
MODEL08 INV z0 =1.45m - FIT =87.78%
Fluent
Model
Free-surface velocity (m/s)
Time (s)

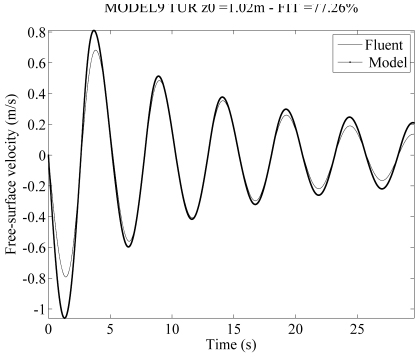
Fluent
Model
Free-surface velocity (m/s)
Time (s)

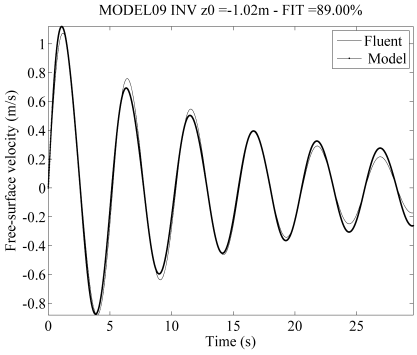
MODEL09 INV z0 =-1.02m - FIT =89.00%
Fluent
Model
Free-surface velocity (m/s)
Time (s)

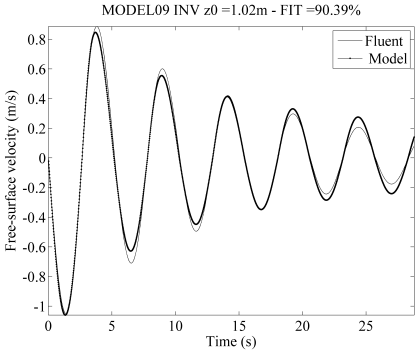
MODEL09 INV z0 =1.02m - FIT =90.39%
Fluent
Model
Free-surface velocity (m/s)
Time (s)

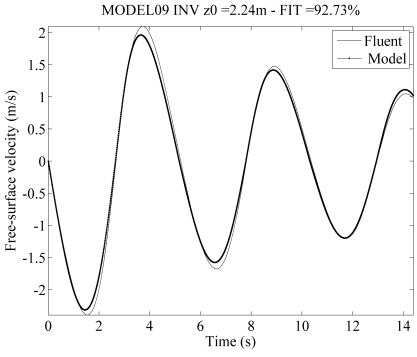
MODEL09 INV z0 =2.24m - FIT =92.73%
Fluent
Model
Free-surface velocity (m/s)
Time (s)

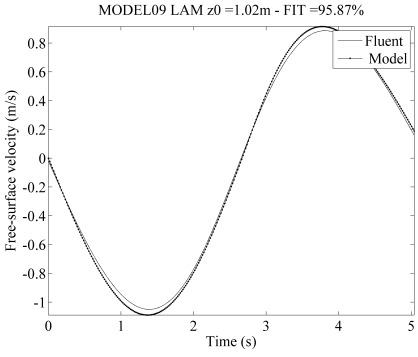
MODEL09 LAM z0 =1.02m - FIT =95.87%
Fluent
Model
Free-surface velocity (m/s)
Time (s)

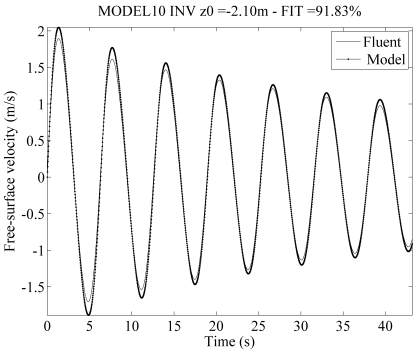
MODEL10 INV z0 =-2.10m - FIT =91.83%
Fluent
Model
Free-surface velocity (m/s)
Time (s)

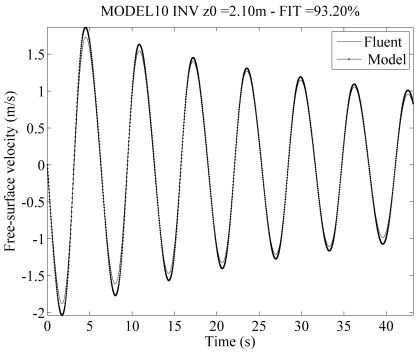
MODEL10 INV z0 =2.10m - FIT =93.20%
Fluent
Model
Free-surface velocity (m/s)
Time (s)

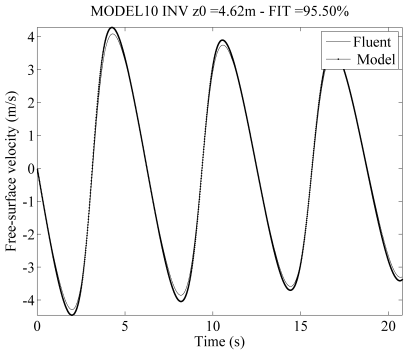
MODEL10 INV z0 =4.62m - FIT =95.50%
Fluent
Model
Free-surface velocity (m/s)
Time (s)

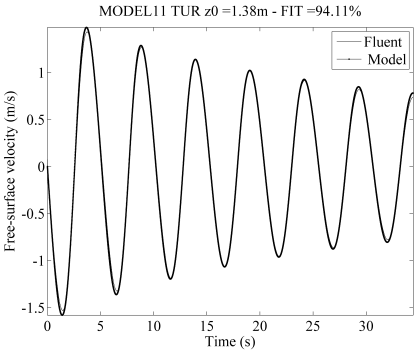
MODEL11 TUR z0 =1.38m - FIT =94.11%
Fluent
Model
Free-surface velocity (m/s)
Time (s)

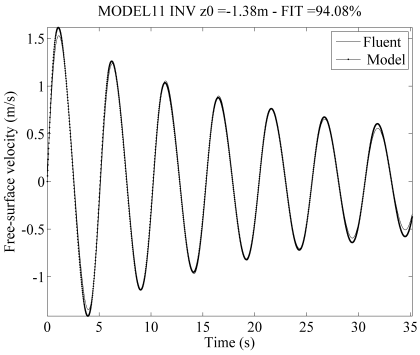
MODEL11 INV z0 =-1.38m - FIT =94.08%
Fluent
Model
Free-surface velocity (m/s)
Time (s)

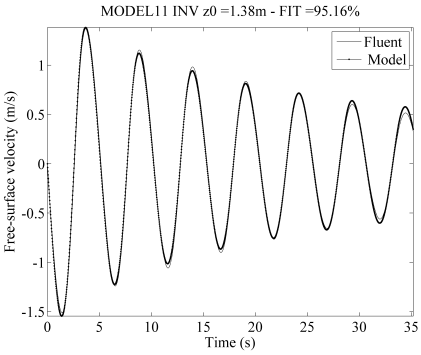
MODEL11 INV z0 =1.38m - FIT =95.16%
Fluent
Model
Free-surface velocity (m/s)
Time (s)

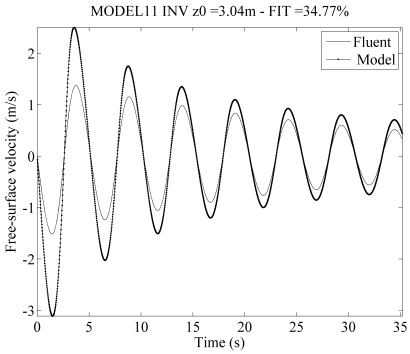
MODEL11 INV z0 =3.04m - FIT =34.77%
Fluent
Model
Free-surface velocity (m/s)
Time (s)

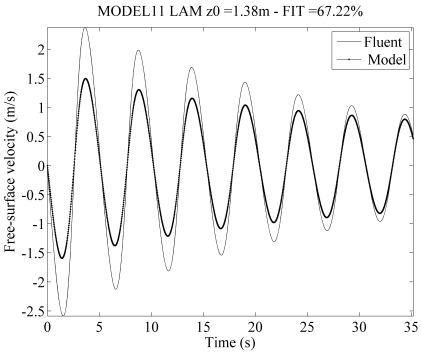
MODEL11 LAM z0 =1.38m - FIT =67.22%
Fluent
Model
Free-surface velocity (m/s)
Time (s)

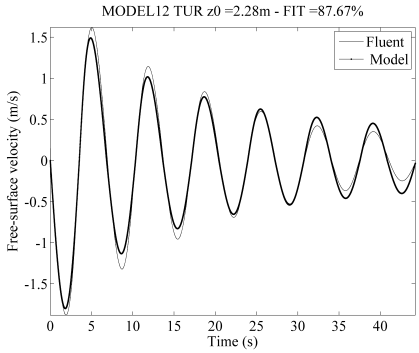
MODEL12 TUR z0 =2.28m - FIT =87.67%
Fluent
Model
Free-surface velocity (m/s)
Time (s)

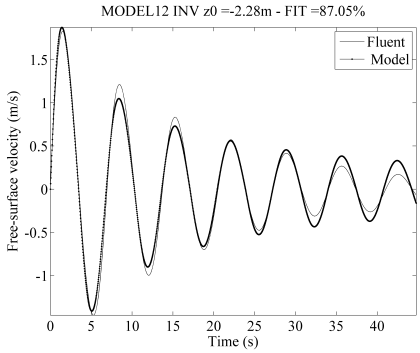
MODEL12 INV z0 =-2.28m - FIT =87.05%
Fluent
Model
Free-surface velocity (m/s)
Time (s)

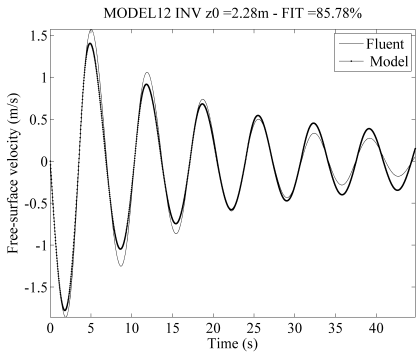
MODEL12 INV z0 =2.28m - FIT =85.78%
Fluent
Model
Free-surface velocity (m/s)
Time (s)

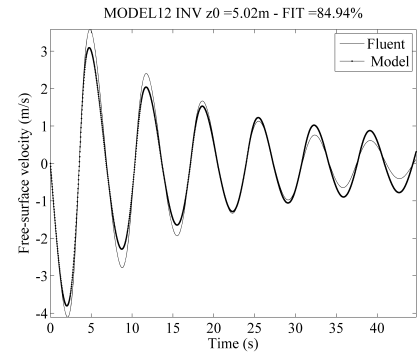
MODEL12 INV z0 =5.02m - FIT =84.94%
Fluent
Model
Free-surface velocity (m/s)
Time (s)

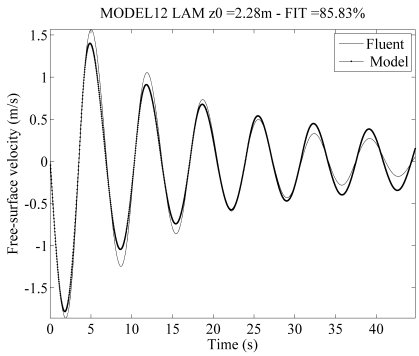
MODEL12 LAM z0 =2.28m - FIT =85.83%
Fluent
Model
Free-surface velocity (m/s)
Time (s)

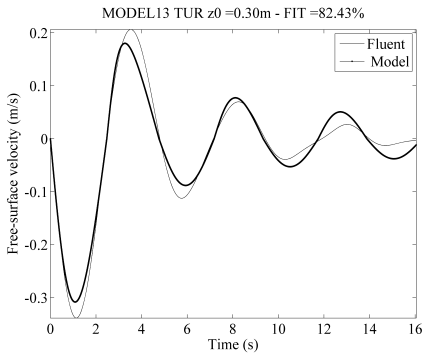
MODEL13 TUR z0 =0.30m - FIT =82.43%
Fluent
Model
Free-surface velocity (m/s)
Time (s)

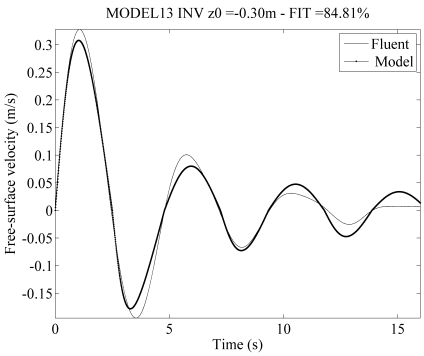
MODEL13 INV z0 =-0.30m - FIT =84.81%
Fluent
Model
Free-surface velocity (m/s)
Time (s)

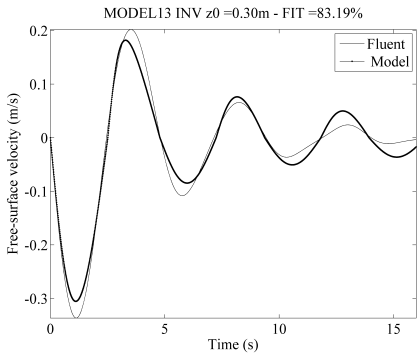
MODEL13 INV z0 =0.30m - FIT =83.19%
Fluent
Model
Free-surface velocity (m/s)
Time (s)

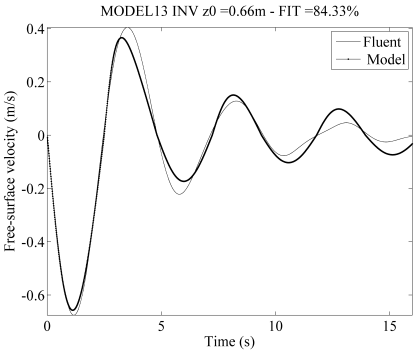
MODEL13 INV z0 =0.66m - FIT =84.33%
Fluent
Model
Free-surface velocity (m/s)
Time (s)

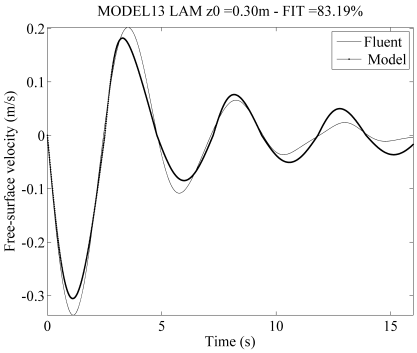
MODEL13 LAM z0 =0.30m - FIT =83.19%
Fluent
Model
Free-surface velocity (m/s)
Time (s)

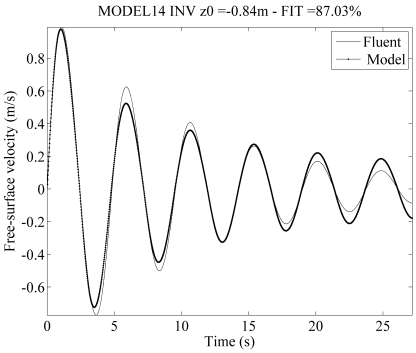
MODEL14 INV z0 =-0.84m - FIT =87.03%
Fluent
Model
Free-surface velocity (m/s)
Time (s)

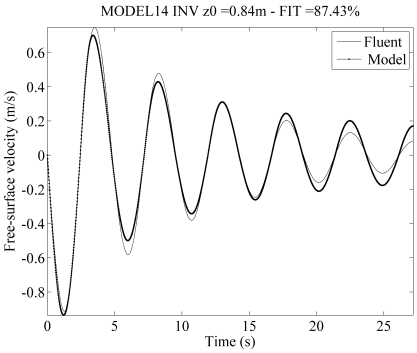
MODEL14 INV z0 =0.84m - FIT =87.43%
Fluent
Model
Free-surface velocity (m/s)
Time (s)

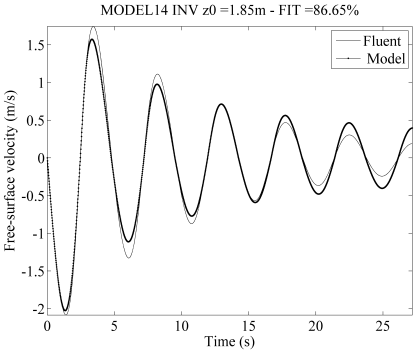
MODEL14 INV z0 =1.85m - FIT =86.65%
Fluent
Model
Free-surface velocity (m/s)
Time (s)

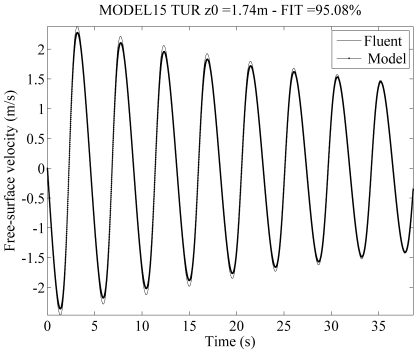
MODEL15 TUR z0 =1.74m - FIT =95.08%
Fluent
Model
Free-surface velocity (m/s)
Time (s)

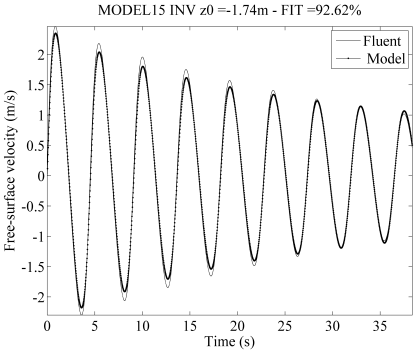
MODEL15 INV z0 =-1.74m - FIT =92.62%
Fluent
Model
Free-surface velocity (m/s)
Time (s)

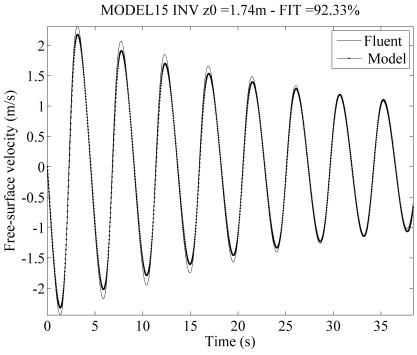
MODEL15 INV z0 =1.74m - FIT =92.33%
Fluent
Model
Free-surface velocity (m/s)
Time (s)

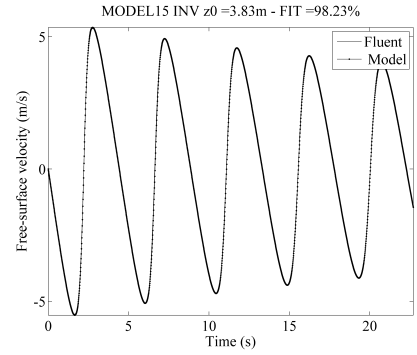
MODEL15 INV z0 =3.83m - FIT =98.23%
Fluent
Model
Free-surface velocity (m/s)
Time (s)

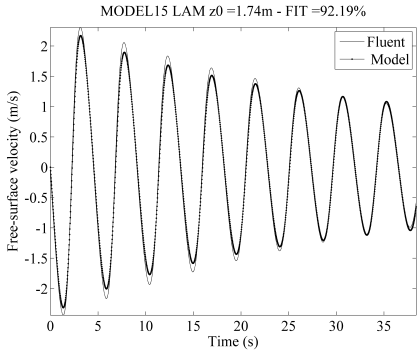
MODEL15 LAM z0 =1.74m - FIT =92.19%
Fluent
Model
Free-surface velocity (m/s)
Time (s)

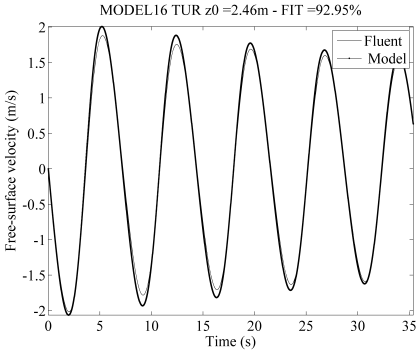
MODEL16 TUR z0 =2.46m - FIT =92.95%
Fluent
Model
Free-surface velocity (m/s)
Time (s)

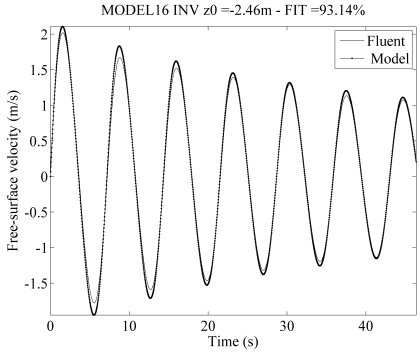
MODEL16 INV z0 =-2.46m - FIT =93.14%
Fluent
Model
Free-surface velocity (m/s)
Time (s)

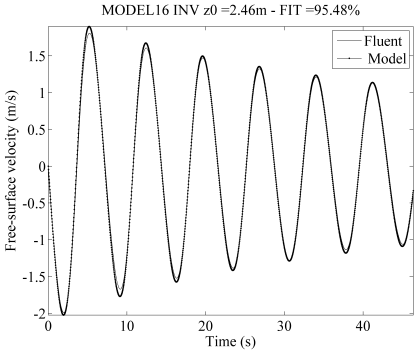
MODEL16 INV z0 =2.46m - FIT =95.48%
Fluent
Model
Free-surface velocity (m/s)
Time (s)

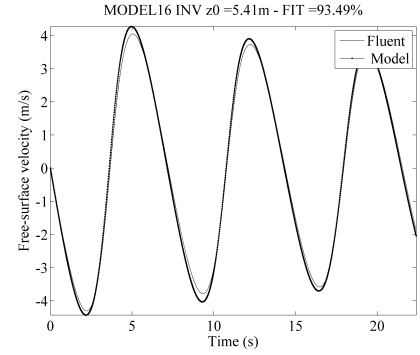
MODEL16 INV z0 =5.41m - FIT =93.49%
Fluent
Model
Free-surface velocity (m/s)
Time (s)

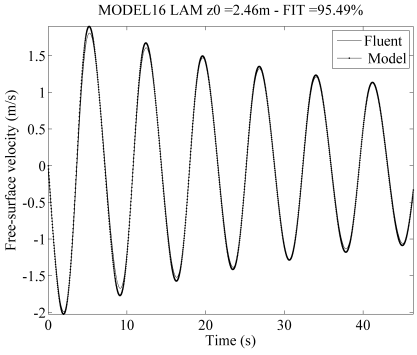
MODEL16 LAM z0 =2.46m - FIT =95.49%
Fluent
Model
Free-surface velocity (m/s)
Time (s)

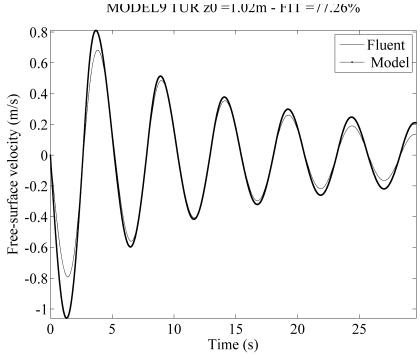
Fluent
Model
Free-surface velocity (m/s)
Time (s)